Size effects in dislocation-mediated plasticity in copper alloys with different microstructural length-scales

Alexandra Cackett

August 2020

Submitted in partial fulfilment of the requirements of the degree of

Doctor of Philosophy

Supervisors: Dr. A.J. Bushby and Dr. C.D. Hardie

School of Engineering and Materials Science

Queen Mary University of London

Statement of Originality

I, Alexandra Cackett, confirm that the research included within this thesis is my own work or that where it has been carried out in collaboration with, or supported by others, that this is duly acknowledged below and my contribution indicated. Previously published material is also acknowledged below.

I attest that I have exercised reasonable care to ensure that the work is original, and does not to the best of my knowledge break any UK law, infringe any third party's copyright or other Intellectual Property Right, or contain any confidential material.

I accept that the College has the right to use plagiarism detection software to check the electronic version of the thesis.

I confirm that this thesis has not been previously submitted for the award of a degree by this or any other university.

The copyright of this thesis rests with the author and no quotation from it or information derived from it may be published without the prior written consent of the author.

Signature:

Date:

Relevant publications:

A.J. Cackett, C.D. Hardie, J.J.H. Lim and E. Tarleton. Spherical indentation of copper: Crystal plasticity vs experiment. *Materialia*, 7:100368, 2019.

A.J. Cackett, J.J.H. Lim, P. Klupś, A.J. Bushby and C.D. Hardie. Using spherical indentation to measure the strength of copper-chromium-zirconium. *Journal of Nuclear Materials*, 511:610-616, 2018.

Select conference presentations:

A.J. Cackett, H. Vo, P. Hosemann, C.D. Hardie and A.J. Bushby. Exploring size effects in copper-chromium-zirconium using indentation techniques and in-situ micro-pillar compression. *Nanomechanical testing in materials research and development VI (ECI Series)*, Poster, 2019.

A.J. Cackett, C.J. Campbell, S.P.A. Gill, J.J.H. Lim, A.J. Bushby and C.D. Hardie. Predicting the microstructural length scale of CuCrZr alloys using spherical indentation. *Thin film and small scale mechanical behaviour (Gordon Research Seminar)*, Poster, 2018.

A.J. Cackett, A. Schiavi, J.J.H. Lim, C.D. Hardie and A.J. Bushby. Observing the size effect in CuCrZr using spherical indentation. *Nanomechanical testing in materials research and development V (ECI Series)*, Poster, 2017.

Acknowledgements

This work has been carried out within the framework of the EUROfusion Consortium and has received funding from the Euratom research and training programme 2014-2018 and 2019-2020 under grant agreement No 633053. The views and opinions expressed herein do not necessarily reflect those of the European Commission.

This project has also received funding from the EMPIR programme (14IND03) co-financed by the Participating States and from the European Union's Horizon 2020 research and innovation programme.

Equipment at the Materials Research Facility at UKAEA was used; the MRF is funded by the UK National Nuclear User Facility and Henry Royce Institute.

A Post-Graduate Research Fund was awarded by Queen Mary University of London and used to part-fund the work presented in Chapter 7. This research was also performed using funding received from the DOE Office of Nuclear Energy's Nuclear Energy University Programs.

I would also like to acknowledge Prof. Daniel Kiener, for the production of nano-grained samples used in Chapter 6, and the help of Prof. Peter Hosemann and Mr Hi Vo with *in-situ* pillar compression experiments, the results of which are presented in Chapter 7.

There are many people I'd like to thank for all the help they've given me in completing this thesis and throughout the duration of my PhD. Firstly, my supervisors Dr Chris Hardie and Dr Andy Bushby. When Chris took me on as a graduate placement student I don't think he expected to be stuck with me for an additional four years but I hugely appreciate all that he's taught me and the amount of effort he has put into making me the (hopefully slightly better) scientist I am today. Early on Andy imparted on me the value of conferences, at which I learnt so much and met some great people who I was later lucky enough to collaborate with. His in-depth knowledge of this subject has also helped enormously with the interpretation of results, for which I am extremely grateful.

I would also like to thank everyone at UKAEA who has supported me in various ways: Joven, for his many (many) hours on the TEM; the iMeter group, for their technical help and scientific discussions; the MRF ops team, who enabled experiments to take place; Kate, for keeping me sane after long hours in the lab; James and Jason, who provided much-needed coffee and advice in equal measures; and everyone else along the way.

Finally, thank you to my family. My parents' encouragement throughout school, university, and now my career has got me to where I am today and this thesis is a testament to that. Thanks to my sister, for always showing an interest in what I'm doing even though you're not quite sure what that is! And to Dave; you always had faith in me, even when I wanted to give up, and I'll always be so grateful for all your support and for the countless other ways in which you've helped me.

Abstract

Over the last decade mechanical size effects have been recognised as a real phenomenon in which a material appears stronger when the volume of material under stress is reduced to dimensions of less than a micrometre. These size effects in the plastic deformation result from microstructural features in the material, such as crystal size or object spacing, or from the stressed volume imposed during nanomechanical tests. Plasticity size effects are particularly evident in materials that deform by dislocation plasticity, such as metals and some semi-conductor and ceramic materials. The relationships between test scale and internal microstructural features were examined for pure copper and the precipitation-hardened alloy copper-chromium-zirconium. A variation in test scale was achieved using spherical nanoindentation with a range of tip radii, as well as Berkovich indentation. The microstructural length-scales considered were Cr precipitate spacing, grain size, and nano-scale defects due to proton irradiation.

The work has implications in the application of small-scale test techniques such as nanoindentation. Understanding size effects is important for interpreting the results of such tests and for exploiting the size effect as a new strengthening mechanism in materials. For the nuclear power generation industry small-sized test samples have significant advantages; reduced volumes of material have lower levels of radioactivity, and non-destructive test methods enables continued structural monitoring using the same witness sample. An understanding of the size effects will also assist in adoption of these test methods in the nuclear power and other critical industries.

Table of contents

List of figures

List of tables

Nomenclature

Greek Symbols

ε	Strain
λ	Characteristic mean free path
σ	Stress
σ_y	Yield stress
ϕ_c	Critical angle
ρ	Dislocation density
τ_0	Intrinsic shear strength
τ_c	Critical shear stress
τ_{th}	Theoretical (maximum) shear strength
υ	Poisson's ratio

Other symbols

a	Indentation contact radius
A_c	Projected contact area with surface
b	Burgers vector
C_i	Frame compliance
d	Grain diameter

E	Elastic modulus
E_i	Indenter modulus
E_r	Reduced modulus
E_s	Sample modulus
F	Indentation load
G	Shear modulus
H	Hardness
h_c	Contact depth at peak load
h_e	Elastic recovery displacement
h_r	Residual indent depth
h_t	Total indenter displacement
k_{HP}	Hall-Petch constant
K_f	Frame stiffness
L	Intrinsic length scale
m	Schmid factor
P_m	Mean pressure
R	Indenter tip radius
R'	Residual indentation tip radius
S	Indenter stiffness
T	Dislocation line tension

Acronyms / Abbreviations

BCC	Body-centred cubic

CRSS	Critical resolved shear stress
dpa	Displacements per atom
EDS	Energy dispersive X-ray spectroscopy
EELS	Electron Energy Loss Spectroscopy
FCC	Face-centred cubic
FIB	Focused ion beam
GND	Geometrically-necessary dislocation
ISE	Indentation size effect
NI	Nanoindenter
RSS	Resolved shear stress
SEM	Scanning electron microscope
SGP	Strain gradient plasticity
SSD	Statistically stored dislocation
STEM	Scanning transmission electron microscope
TEM	Transmission electron microscope
TKD	Transmission Kikuchi diffraction

Chapter 1

Introduction

Encouraged by the standardisation of methods and advances in precision instrumentation such as the focused ion beam, the use of small-scale testing techniques is now commonplace in many industries. This is particularly true of the nuclear industry, which has several reasons to help drive the miniaturisation of samples. Most importantly, there are significant health and safety benefits to reducing the volume of neutron-irradiated materials used for mechanical testing. Dedicated facilities with remote handling capabilities are required to process highly active samples but if the sample size, and hence the activity levels, can be sufficiently decreased then they may fall within manual handling safety limits. It is also hugely costly to insert samples into materials testing reactors and space is at a premium, therefore small-scale tests can increase the amount of data that can be obtained from each valuable specimen. To avoid the hazards of active samples completely, ion-irradiation is often used as a surrogate to neutron irradiation to induce similar microstructural damage without activation of the material. However, this technique only produces localised damage, typically on the order of several micrometers into the surface of the sample, meaning that miniaturised tests are often the only available option.

Whilst the benefits of small-scale techniques are clear, there is one major drawback in terms of the interpretation of results. A considerable amount of research over the past two decades has established that there are significant size dependencies in mechanical behaviour when sample length-scales approach microstructural length-scales. This is related to the classical 'size effect' in materials science, whereby a reduction in microstructural length-scale increases mechanical strength. It is therefore important to understand both the test methods and the influence of

microstructure on the measured values at reduced volumes if small-scale testing is to produce engineering-relevant data.

The work contained within this thesis aims to evaluate the mechanical response of materials with different microstructural length-scales when measured using small-scale techniques. Nanoindentation using Berkovich and spherical tips was the principal method used, with the indentation size effect first established in single crystal copper to determine the extrinsic length-scales of importance without influence from complex microstructural features. These tests were then repeated in copper-chromium-zirconium, an alloy with current and future applications in the nuclear industry. Three different dominant intrinsic length-scales were investigated: precipitates, with a variation in size and spacing; grain boundary density, whereby grain size was reduced using severe plastic deformation; and irradiation defects induced by proton irradiation. For the latter of these, in-situ micro-pillar compression testing was also carried out. Finally, the results from these experiments were used to evaluate current size effect models and the dislocation plasticity mechanisms they are based on.

Chapter 2

Literature review

It has long been known that the mechanical properties of a material can be altered by modifying its microstructure, with a reduction in the dominant intrinsic length-scale resulting in an increase in strength being commonly referred to as the 'size effect' in materials testing. Over the last two decades a second size effect has also been recognised whereby a material appears stronger in regimes where the stressed volume of material is less than a micrometre. Given the increasing interest in small-scale test techniques in numerous industries - e.g. electronics, nuclear, thin films - the nature of this so-called 'extrinsic' size effect needs to be characterised and the mechanisms behind it better understood.

Plastic deformation in metals predominantly occurs by the creation and movement of dislocations. Microstructural features such as grain boundaries or precipitates interact with dislocations and therefore change the response to deformation, which is measured as a change in mechanical properties thus giving rise to the intrinsic size effect. It stands to reason that extrinsic size effects are also related to dislocation behaviour; by reducing the stressed volume, dislocation multiplication by Frank-Read sources must be limited by the space in which they have to operate, and free surfaces will affect potential interactions with preceding dislocations.

This chapter aims to give a brief introduction to the nature of dislocations and dislocation-mediated plasticity, as well as provide a review of the various approaches to understanding size effects identified in recent literature. The discussion will be restricted to the deformation of face-centred cubic (FCC) structures and highlight particularly relevant work on copper and irradiated samples.

2.1 Plastic deformation in metals

In order to relate material response during deformation to potential dislocation mechanisms it is important to first establish the fundamental properties and concepts surrounding dislocations, since these form the basis of more complex models. This section will therefore lay-out some of the main textbook principles that are prevalent in many later theories and which will be referred to in the following section when describing various strengthening processes in metals.

2.1.1 The nature of dislocations

When metals first begin to deform under load they do so elastically by the stretching of atomic bonds and when the load is removed the material returns to its original shape. Within the regime of elastic deformation the applied stress, σ, is proportional to the strain, ε, and related by the modulus of elasticity, also known as Young's modulus, E,

$$\sigma = E\varepsilon \tag{2.1}$$

If the applied stress is increased to a point where the material does not return after the load has been removed then the material has been plastically deformed, whereby the atomic arrangement of the material has changed through the breaking and re-joining of atomic bonds. In metals, shear deformation is accommodated by the slip of atomic planes over one another. In the case of small strains the theoretical shear stress τ_{th} required for one row of atoms to slip over the row below can be expressed as,

$$\tau_{th} = \frac{b}{a}\frac{G}{2\pi} \tag{2.2}$$

where G is the shear modulus, b is the spacing between adjacent atoms on the same row, and a the atomic spacing. This implies that the maximum shear strength approaches a sizeable proportion of the shear modulus, which is not what is observed experimentally. Instead, it was found that crystals deform through the propagation of discrete linear faults called dislocations.

The concept of a dislocation was first postulated in papers by Orowan [2], Taylor [3] and Polanyi [4] published concurrently in 1934. Taylor proposed that the difference between theoretical and measured shear strength could be reasoned if "*slipping is considered to occur not simultaneously over all atoms in the slip plane but over a limited region, which is propagated*

from side to side of the crystal in a finite time" [3]. He illustrates an example in which there is an additional half plane of atoms present as the top rows of atoms slips over the bottom rows; this is now known to be an edge dislocation, with a second type - the screw dislocation - identified later by Burgers [5]. Schematics of edge and screw dislocations can be seen in Figure 2.1.

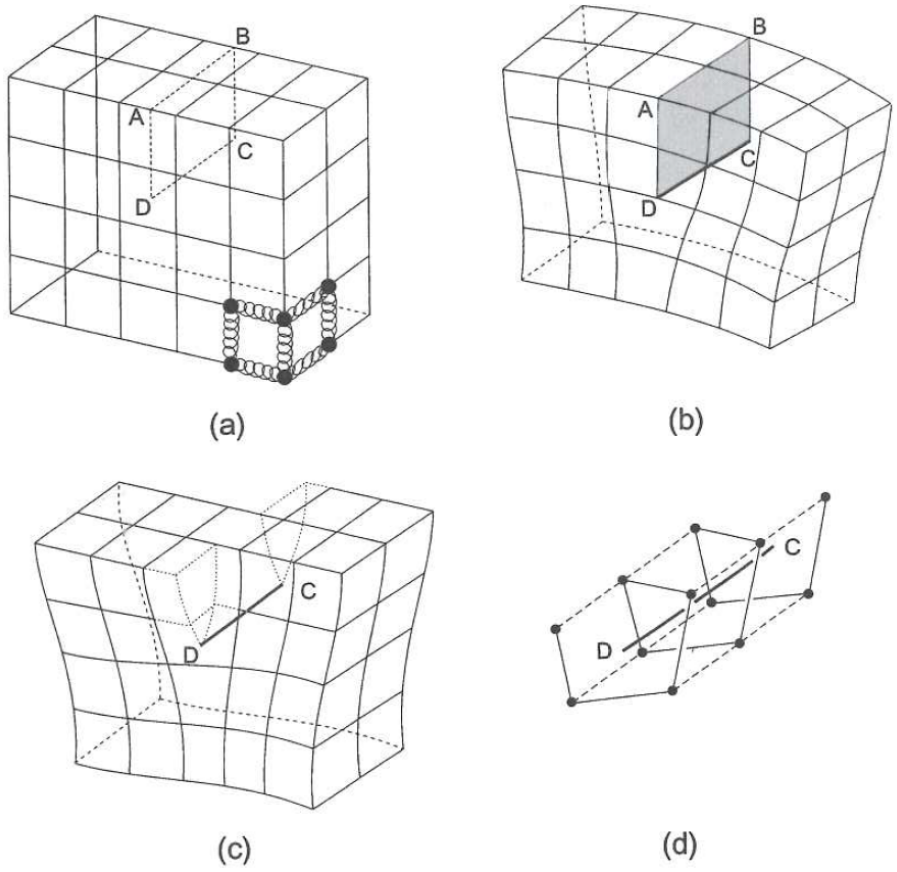

Fig. 2.1 (a) Illustration of a simple cubic structure, (b) an edge dislocation DC produced by an extra half-plane of atoms shown by the shaded region, (c) a screw dislocation DC created by displacing the faces either side of the shaded plane in the direction of AB, and (d) the spiral of atoms that surround the screw dislocation shown in (c) (reprinted from [6]).

Both types of dislocation are generally defined by their Burgers vector, **b**, which is the vector difference between a continuous atom-to-atom circuit containing the dislocation and the same circuit in an equivalent clean (dislocation-free) crystal. For an edge dislocation the Burgers vector is normal to the dislocation line and for a screw dislocation the Burgers vector is parallel to the dislocation line. In reality, dislocations are almost always curved and therefore a combination of both edge and screw. It is also worth noting that dislocation lines cannot end within a crystal and therefore must either reach a free surface or, more commonly, form a closed loop.

Dislocations necessarily induce a strain field due to the elastic distortion surrounding them. Since a deformed crystal is not in its lowest energy state it is possible to define the additional energy due to the presence of a dislocation, the so-called 'strain energy'. The total strain energy is composed of a core and an elastic part; given in terms of energy per unit length the elastic part can be expressed by the following equations for an edge and screw dislocation [6]:

$$E_{el}(screw) = \frac{Gb^2}{4\pi}\int_{r_0}^{R}\frac{dx}{x} = \frac{Gb^2}{4\pi}\ln\left(\frac{R}{r_0}\right) \tag{2.3}$$

and

$$E_{el}(edge) = \frac{Gb^2}{4\pi(1-\nu)}\int_{r_0}^{R}\frac{dx}{x} = \frac{Gb^2}{4\pi(1-\nu)}\ln\left(\frac{R}{r_0}\right) \tag{2.4}$$

where ν is Poisson's ratio, b the magnitude of the Burgers vector, and R and r_0 the outer and inner radii, respectively, of a cylinder of material containing the dislocation line at its core. An inner radius term is present because at the very core of a dislocation stress and strain approach infinity as $r \to 0$, at which point elasticity theory breaks down and an atomistic model is required to resolve it. Using typical values for R and r_0 both equations can be simplified to,

$$E_{el} = \alpha G b^2 \tag{2.5}$$

where $\alpha \approx 0.5 - 1.0$, depending on the character of the dislocation (edge or screw).

Equations 2.3 and 2.4 demonstrate that the elastic strain energy of a dislocation drops off logarithmically as a function of radial distance from the core. It is also evident that when multiple dislocations are present it is possible for long-range strain fields to cancel each other out. Most importantly, since strain energy is proportional to the length of a dislocation an externally applied force is required to change the length and this concept will come into use in the following section.

2.1.2 Dislocations during deformation

As mentioned previously, metals deform via slip - the glide of multiple dislocations. Slip occurs on particular slip planes that typically contain the highest density of atoms, and in the direction of the shortest lattice translation. In the case of a FCC metals this means that slip is most often on the {111} planes in the <110> directions, which results in 12 possible slip systems thus

making deformation relatively easy. The shear stress required to initiate slip on one plane is referred to as the critical resolved shear stress (CRSS), which is expressed as

$$\tau_c = \frac{F}{A}\cos(\phi)\sin(\lambda) \tag{2.6}$$

where F is a force applied along the crystal axis, A the cross-sectional area of the sample, ϕ the angle between the direction of applied force and the slip plane normal, and λ the angle between the applied force and direction of slip (see Figure 2.2). The angular terms are commonly combined into one quantity, the Schmid factor, $m = \cos(\phi)\sin(\lambda)$.

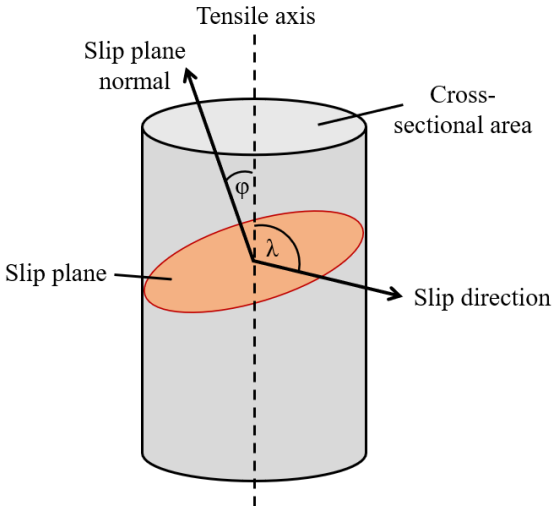

Fig. 2.2 Slip plane directions and angles used in the calculation of Schmid factor.

As can be seen from Eq. 2.5 the energy of a dislocation is proportional to b^2. In FCC systems it is therefore energetically more favourable for slip to happen through the movement of partial dislocations with a Burgers vector of $\frac{1}{2}$<110>, which represents the shortest lattice vector in the crystal. Between two partials lies a stacking fault, a type of surface defect where the normal stacking sequence of atomic planes is interrupted. During deformation the leading partial creates a stacking fault and the following partial clears it, leaving behind a perfect crystal. If the stacking fault energy (related to crystal structure) is low then partials are able to spread out, making deformation via cross-slip difficult. In addition to this screw dislocations cannot disassociate, therefore only part of the total length of a mixed dislocation can separate into partials.

When a large shear stress is applied to a material, dislocation multiplication is necessary in order to accommodate a perceptible amount of deformation. The amount of slip required for experimentally observed plastic deformation could not be produced by the passage of single dislocations from one side of a crystal plane to the other. Instead, a source must activate on a suitable slip plane from which dislocations are emitted in directions away from each other and with opposite Burgers vector signs. One way in which this can be achieved is through the operation of a Frank-Read source [7]. A representation of dislocation generation by a Frank-Read source is shown in Figure 2.3.

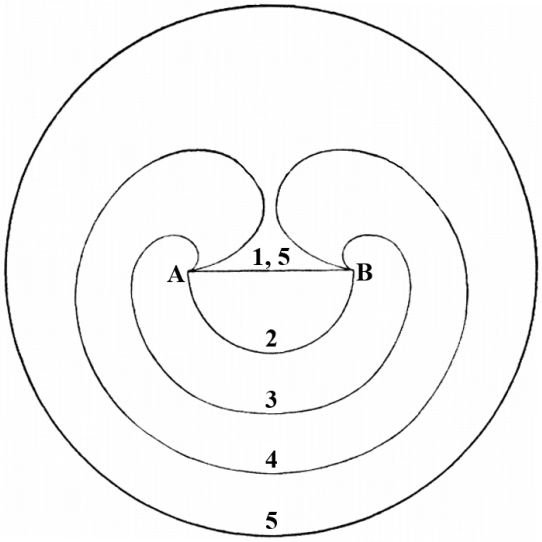

Fig. 2.3 Generation of dislocations via a Frank-Read source. The initial dislocation line (position 1) is pinned by points A and B. Under an applied stress it bows out between these two points (positions 2 - 4) until two elements of the dislocation meet and annihilate, producing a closed loop dislocation that progresses outwards as well as a dislocation segment again pinned by points A and B (position 5). Redrawn from [7].

In this mechanism a dislocation is pinned at both ends and begins to bow out under an applied stress. According to Eq. 2.5, any change in dislocation length results in an increase in its energy. This energy increase per unit of additional length is referred to as line tension, T, and is defined as,

$$T = \alpha G b^2 \tag{2.7}$$

From this an expression can be obtained that defines the shear stress required to bend a dislocation to a radius of curvature R,

$$\tau_0 = \frac{\alpha G b}{R} \tag{2.8}$$

Due to the inverse relationship between τ_0 and R, as the shear stress increases the radius of curvature decreases until R reaches a minimum. This minimum is at position 2 in Figure 2.3 when $R = L/2$, where L is the distance between pinning points. If the dislocation expands further, R increases and the dislocation is no longer stable so it continues to bow out until two segments meet. These segments annihilate, resulting in a dislocation loop that expands outwards and a "new" dislocation again pinned between the original points. This process is subsequently able to repeat as long as the applied stress is large enough to initiate it.

It is also possible to have a single-ended source and this is in fact now thought to be a more common occurrence than the type shown in Figure 2.3. In the single arm source, also known as a spiral source, only one end of the dislocation is anchored. The dislocation line is able to move freely in one slip plane, leading to it winding into a spiral about the pinning point. Each full rotation of the dislocation results in a shift of the lattice of one atomic spacing with respect to the rest of the lattice below the slip plane. This process can also repeat multiple times, therefore producing a larger displacements. The passage of multiple dislocations will also result in a small (but measurable) rotation of the crystal.

Once the maximum shear stress required for source operation has been reached (Eq. 2.8), dislocations are able to glide away from the source. If they encounter a free surface or grain boundary they will disappear, leaving behind a perfect crystal with a slip step at the boundary. If dislocations travel down a strain gradient and run out of driving force then they can become stuck in the lattice. Finally, if one dislocation encounters another gliding in the opposite direction they may annihilate (if they have opposite sign) or become locked, often resulting in the generation of a new source.

There are two key points that should be highlighted from the above theories. Firstly, dislocations have an associated strain energy that is a function of the dislocation line length, therefore an external force must be applied in order to bend a dislocation, for example when bypassing an obstacle in the crystal structure. Secondly, plastic deformation in metals initially only requires the movement of dislocations, however to accommodate any discernible amount of plastic deformation dislocations must multiply. One way to do this is via a Frank-Read source; this mechanism requires dislocations to bend outwards (or wind around) pinning points and according to the former point this requires a shear stress. It can be shown that this stress is inversely proportional to the radius of curvature, which in turn depends on the distance between

pinning points. Changing the distance between obstacles that act as pinning points subsequently affects the force required to deform the crystal structure, thus altering its mechanical strength. Some of the different physical approaches that can be used to exploit this phenomenon will now be explored in the following section.

2.2 Strengthening in metals

The process of strengthening metals by altering their microstructure has been carried out for thousands of years, far before the physics behind the techniques was understood. The alloying of iron with carbon to produce steel, for example, is thought to have been carried out as early as 2500–2000 B.C. [8] and water-quenching the tip of a sword to increase its hardness was documented in China around the year 100 B.C. [9]. There has since been extensive research into the mechanisms behind such metallurgical strengthening techniques and the different theories behind some of these will now be explored.

2.2.1 Grain size strengthening

Materials scientists have long exploited the knowledge that that grain boundaries could offer some kind of strengthening mechanism. In 1951 E. O. Hall published a paper suggesting that the lower yield point is inversely proportional to the square root of grain diameter [10]. This, along with similar research carried out by N. J. Petch [11], lead to the now well-known 'Hall-Petch' relationship, which has since been supported by many other experiments on a range of other metals (e.g. [12] and [13]). A general form of the Hall-Petch equation takes the following form:

$$\sigma_y = \sigma_0 + k_{HP} d^{-0.5} \tag{2.9}$$

where σ_y is the yield stress, σ_0 is the yield stress of a single crystal, k_{HP} is a material constant, and d is the grain size. This relation arose empirically, with the inverse square-root dependence on grain diameter being based on its ability to provide a good fit to data from a range of metals. Most commonly it is reasoned that reducing the grain size, and therefore increasing the density of grain boundaries, leads to an increase in hardness due to dislocation pile-up at the boundaries. In this situation there is a stress concentration ahead of the pile-up that is proportional to the

number of dislocations, which in turn exerts a back-stress on the source within the grain. Thus, for the source to continue to generate dislocations within the same grain a force higher than the critical stress for normal source generation is required. Similarly, yield will only occur when slip is able to cross the grain boundary. The required yield stress is related to the pile-up length, L, and critical stress, τ_c, [14],

$$\tau_y = \tau_0 + \left(\frac{\alpha \tau_c G b}{L d_g} \right)^{1/2} \tag{2.10}$$

where d_g is the dislocation loop diameter and other terms are as previously described. There is, however, a lack of experimental evidence of pile-up particularly in FCC metals and only limited examples in other material systems.

In the 1960's a new model was introduced by Li [15] based on the proposition that grain boundaries could be a source of dislocations. When first describing strain-hardening, Taylor [3] developed the following expression to relate flow stress to dislocation density,

$$\tau = \tau_0 + \alpha G b \sqrt{\rho} \tag{2.11}$$

where α is a dimensionless material parameter and ρ is the dislocation density. It can be shown [16] that the dislocation density is the ratio of the number of grain boundary ledges to the grain diameter, $\rho = m/d$. Substituting this into the Taylor equation gives,

$$\tau_y = \tau_0 + \alpha G b m^{1/2} d^{-1/2} \tag{2.12}$$

which has the same form as Eq. 2.9 with the constant k_{HP} encompassing the grain boundary number term.

Later, the concept of a new category of dislocations was used to explain strengthening due to grain refinement. In 1970 Ashby [17] coined the term 'geometrically-necessary dislocations' (GNDs); unlike statistically stored dislocations (SSD), which accumulate during homogeneous deformation, GNDs are necessarily present to accommodate non-uniform strain. When a shear stress is applied to a polycrystalline material, GNDs must be present along grain boundaries otherwise voids or overlaps between adjacent grains would occur as shown in Figure 2.4.

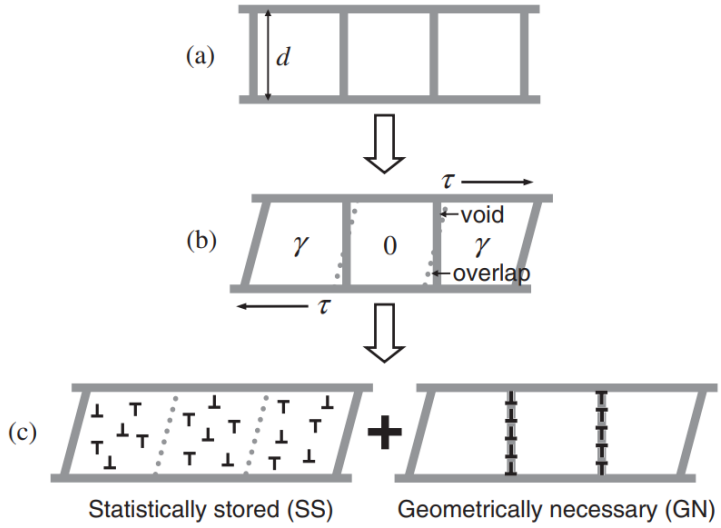

Fig. 2.4 Schematic representation of (a) undeformed grains with diameter d. (b) When a shear stress is applied voids and overlaps between grains are created if the strain of the central grain differs from those either side. (c) SSDs are created during uniform deformation and (d) GNDs allow the accommodation of voids and overlaps. Reprinted from [16].

At small scales GNDs are grain size dependent, with the GND density being much larger than SSD density during inhomogeneous deformation, therefore strength increases with a reduction in grain size. As will be demonstrated in later sections, the concept of GND density can also be used to describe some forms of extrinsic size effects.

Due to the anticipation of an increase in strength with a decrease in grain size there was growing interest in the development of nanocrystalline materials. However, in 1989 Chokshi *et al.* [18] were the first to publish results showing that for Cu and Pd with $d < 20nm$ the opposite was true, with a negative slope to the Hall-Petch equation. This is now referred to as the inverse Hall-Petch effect. A critical review of data that supposedly supports the inverse Hall-Petch theory is given in [19]. In this paper the authors conclude that the majority of experiments have "*obvious or possible artefacts*" that could be responsible for the decrease in strength of nanocrystalline materials, for example porosity or changes in chemistry due to the manufacturing technique of the test material. A few, however, appear to be reliable and in addition to supporting computer simulations they suggest that the inverse Hall-Petch effect is real for grain sizes less than ~10 nm. The mechanisms behind this phenomenon are still being debated; since multiple dislocations cannot be contained in a single grain when grain sizes are ~40 nm the possible alternative causes include grain-boundary sliding and partial dislocation

emission/absorption at boundaries (referred to as 'grain boundary mediated' mechanisms) in order for the material to plastically deform [20].

Most recently, the exact form of the Hall-Petch equation has been put into question for even the standard regime (10's nm – 100's μm). In [21] Dunstan and Bushby consider a number of classic datasets (including W, Fe, Cu and brass) that have been used to verify the Hall-Petch formula. They demonstrated that although the data does fit Eq. 2.9 well, it similarly fits several variations on the formula, for example if the grain diameter exponent was instead $1/4$ or unity. Furthermore, if the grain size exponent is allowed to be a free parameter decided by the least-squares fit then there is no obvious preference for it universally being $-1/2$. The authors conclude that "*there is no conclusive experimental evidence for the inverse square-root dependence of strength upon grain size*" and subsequently suggest that the exponent may be another fitting parameter. If this is done, then the material-dependant constant k_{HP} could be set at unity for all materials.

2.2.2 Precipitation and dispersion hardening

When adding one (or more) elements to another to produce an alloy there is a limit to the concentration of solute atoms that can be contained coherently within the base matrix. When the saturation limit is exceeded the added element will produce second phase particles, such as those found in oxide dispersion strengthened steels, or precipitates. Precipitates can also be achieved by ageing or annealing a solid solution alloy. Strengthening particles such as these act as obstacles to the glide of dislocations during plastic deformation, thus increasing the CRSS of the material.

For slip to occur dislocations must either shear through precipitates or bow out between them. In the case of small and hard precipitates, deformation occurs via the former of these mechanisms. Obstacles exert a resistance force 'F', as shown in Figure 2.5. At equilibrium $F = 2T\cos\phi$, where T is the line tension force. Substituting in Eq. 2.7 this becomes $F \simeq Gb^2\cos\phi$. The localised flow stress required to overcome the maximum resistance force is thus,

$$\tau_{loc} = \frac{F_{max}}{bL} = \frac{2T}{bL}\cos\phi \simeq \frac{Gb}{L}\cos\phi_c \tag{2.13}$$

where L is the obstacle spacing and ϕ_c is the critical angle, both as shown in Figure 2.5. For strong obstacles $\phi_c \approx 0$ and for weak obstacles $\phi_c \approx \pi/2$.

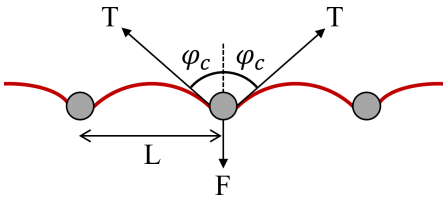

Fig. 2.5 Dislocation bow-out between particles. For a weak obstacle the dislocation line can pass at $\phi_c \approx \pi/2$ and for strong obstacles at $\phi_c \approx 0$.

As precipitates grow and the resistance force increases, it is energetically more favourable for dislocations to bypass precipitates by bowing out between them. As was shown previously in the description of Frank-Read sources, a shear stress is required for dislocations to bow out between obstacles and this is proportional to the distance between pinning points as per Eq. 2.8. Figure 2.6 (a) demonstrates the situation in which the obstacles are impenetrable when d_ρ, the diameter of curvature of the dislocation, is greater than the particle spacing, L. Figure 2.6 (b) shows the bypassing condition when $d_\rho \leq L$.

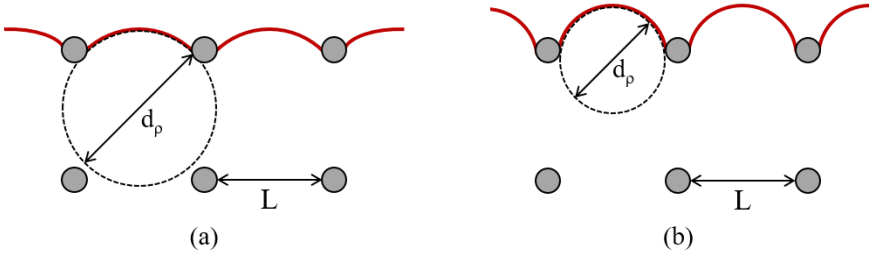

Fig. 2.6 Two cases of a dislocation encountering solute obstacles:(a) resistance to deformation when $d_\rho > L$, and (b) the bypass condition when $d_\rho \leq L$. Redrawn from [22].

An extension to this bypassing process is propagation via the Orowan mechanism. If dislocations bow out between pinning points and expand sufficiently far then segments of the dislocation line are able to meet and annihilate, as was described for Frank-Read sources. This results in an Orowan dislocation loop encasing the precipitate as well as a line dislocation that continues to propagate through the matrix. A schematic showing each of these stages can be seen in in Figure 2.7.

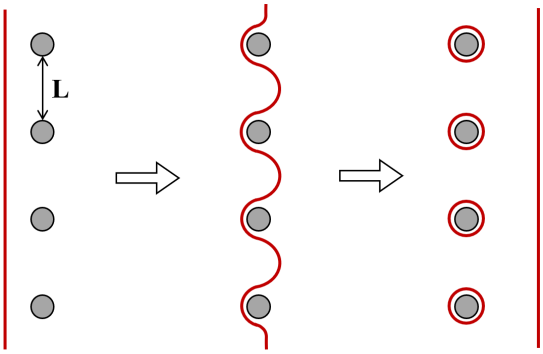

Fig. 2.7 The Orowan mechanism, whereby a dislocation line (red) bows out between strong obstacles, leaving a dislocation loop behind as it passes through the material.

An important aspect of precipitation hardening is that the size and spacing between precipitates can be altered via annealing. This is a highly-reproducible technique commonly used in industry to increase the strength of alloys without changing the chemical composition. The change in yield stress typically exhibited by annealing a precipitation-hardened alloy can be seen in Figure 2.8, where the x-axis could equally represent annealing time or temperature.

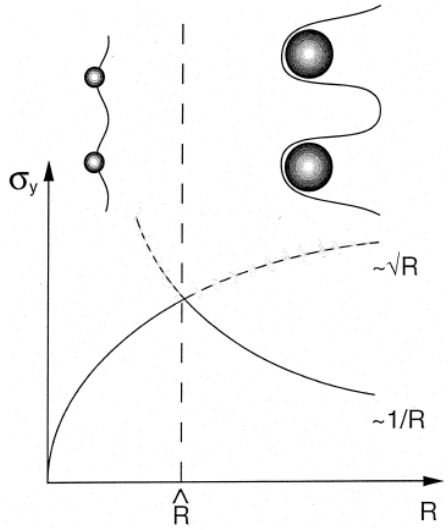

Fig. 2.8 Precipitation hardening resulting from an initial $\sqrt{R}$ dependence due to particle cutting followed by a $1/R$ dependence for the bypassing stress. Maximum yield strength is obtained at a characteristic particle radius $\hat{R}$. Figure taken from [22].

Upon heating a homogeneous solid solution the solutes begin to nucleate, initially producing a fine dispersion of small coherent precipitates that cause an increase in strength due to the strain fields surrounding them. With further heating the precipitates grow and at some point peak strength is achieved when there is a critical dispersion of both coherent and semi-coherent precipitates. If the material continues to be annealed, the alloy becomes over-aged as the

precipitates coarsen - also referred to as Ostwald ripening - and become incoherent, with little lattice strain to resist dislocation motion thus resulting in a decrease in strength.

There are various models that can be used to predict the change in particle size distribution in heat-treated precipitation-hardened alloys (e.g. [23], [24]). Likewise, simulations based on the dislocation-particle interaction mechanisms discussed above have been shown to successfully replicate the strengthening response due to precipitates [25, 26]. Studies such as the aforementioned references, however, suffer from the simplification that a dislocation is treated as a 2D object travelling on a single plane. Since dislocations are often referred to as line defects and textbook schematics are inherently 2D, it easy to overlook that they are in fact 3D objects that move within a volume of material. More recently, 3D dislocation dynamics (DD) simulations have been used that are able to better model the physical processes that can take place during deformation. For example, Santos-Güemes *et al.* used 3D DD to analyse the interaction between dislocations and precipitates in an Al-Cu alloy [27]. They found that including cross-slip in the simulations led to a change in the dislocation path and a reduction in the calculated CRSS when compared to simulations where the dislocation was forced to remain on the initial slip plane. Similarly, dynamical processes such as the Hirsch mechanism [28], dislocation climb [29] and the creation of pinning points [30] can be accounted for in 3D DD simulations to investigate other behaviours observed during mechanical testing.

2.2.3 Solid solution strengthening

In solid solution hardening, atoms of an alloying element are added to the crystalline lattice of the base element and are accommodated coherently. If the atoms of the alloying element take up a vacant position in the host lattice a 'substitutional solid solution' is produced but it is also possible for small atoms to fit between lattice positions, in which case they are considered 'interstitials'. In these systems strengthening occurs as a result of an increase in stacking fault energy and additional lattice friction, both of which alter the behaviour of partial dislocations.

In early work by Nabarro [31] (in collaboration with N.F. Mott) he considered the local stresses induced by the misfit of solute atoms in the solvent matrix and the resultant effect this would have on dislocation motion. It was assumed that a dislocation line would not be able to pass multiple solutes simultaneously if they were closely spaced, instead segments of the dislocation line would be required to move piecewise.

For Nabarro and Mott's model the yield stress is consequently a function of the atomic concentration of the solute [32],

$$\tau = G\varepsilon_b^2 c^{5/3} (\ln c)^2 \tag{2.14}$$

where ε_b is a factor that accounts for the size misfit and c is the solute concentration. Expanding on this, Fleischer [33] later formulated relations for the interaction energy between a solute atom and matrix to take account of the contribution from different shear moduli, introducing an additional factor $\varepsilon_G = (1/G)(dG/dc)$. This was shown to have a considerable effect even at low solute concentrations and brought the theoretical predictions more in line with experimental observations.

In the aforementioned models, solute atoms were assumed to be uniformly dispersed. In reality, it is possible that solute atoms could closely group together and create a situation whereby such groups would be "seen" by a dislocation as a single obstacle with higher strength than individual solute atoms. This clustering effect was addressed by Labusch [34], who modified Eq. 2.14 and produced a new relation for critical shear stress,

$$\tau = \frac{A}{b}\left(\frac{f_m^4 c^2 w}{E}\right)^{1/3} \tag{2.15}$$

where A is a constant that depends on the interaction between a dislocation and obstacle, f_m is the maximum obstacle-dislocation interaction force, w is the interaction range of a cluster obstacle, and E is the line energy of a dislocation per unit length (calculated using Eq. 2.7). It is worth noting that the concentration dependence was also modified from $c^{5/3}$ to $c^{2/3}$ in line with experimental results.

The piece-wise movement of a dislocation line past individual solutes was revised by Nabarro [35]. If an obstacle creates an internal shear stress of τ_i then the maximum force on a dislocation encountering it is $\tau_i b$ per unit length. For a strong barrier the flow stress required to pass it can be defined as,

$$\tau(strong) \simeq \frac{2}{\pi}\tau_i \tag{2.16}$$

In the case of a concentration of closely-packed weak particles, line segments of dislocations are able pass multiple obstacles in one movement. If the particles are randomly spaced an

average distance of Λ apart and the total length of a dislocation line segment is L (see Figure 2.9 (b)) then it can be shown that the flow stress required to overcome the mean internal stress of the combined obstacles along the segment length is [6],

$$\tau \simeq \frac{2\tau_i}{\pi}\left(\frac{\Lambda}{L}\right)^{1/2} \tag{2.17}$$

It is difficult to estimate L but if it is assumed that the radius of curvature of the segment, R, is much greater than its length then the flow stress for a field of weak obstacles is,

$$\tau(weak) \simeq \frac{2}{\pi^{4/3}}\tau_i\left[\frac{\tau_i\Lambda}{Gb}\right]^{1/3} \tag{2.18}$$

It can then be shown that for a dispersion of weak obstacles dislocations pass through multiple obstacles at once at a flow stress of,

$$\tau_{loc}(weak) \simeq \frac{Gb}{\Lambda}(\cos\phi_c)^{3/2} \tag{2.19}$$

where Λ is the fine spacing shown in Figure 2.9. It can be seen that as obstacles get larger and the spacing between them decreases, the flow stress increases. This type of weak force is only applicable to small precipitates, however, and cannot be used when the number of atoms within the obstacle exceeds ~10^5 [6].

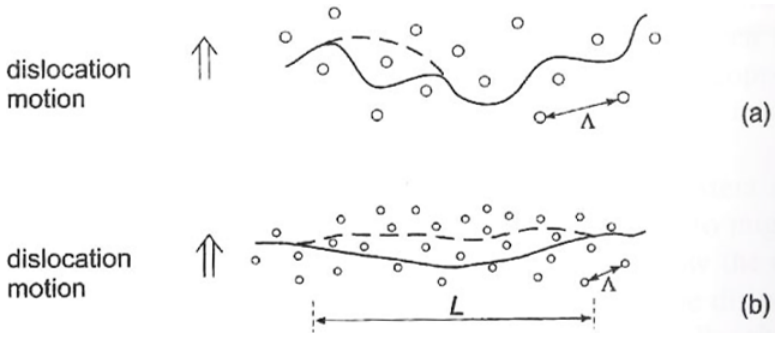

Fig. 2.9 Dislocation line advancing through a field of (a) weak and (b) strong obstacles, where the dashed line represents the new position when critical yield stress is met. Reprinted from [6].

It should be noted that strong obstacles, such as precipitates, are not necessarily more effective at strengthening compared to weak obstacles. Since weak obstacles are generally much smaller than strong obstacles, more can be distributed over the slip area.

Another important aspect of solid solution strengthening is the thermally activated motion of dislocations, with some alloys showing significant changes in yield stress over a range of temperature. Yield stress tends to decrease up to temperatures typically ~$1/3$ of the melting point and a good review of the temperature dependence on CRSS can be found in [32]. Since the work presented in this thesis is only concerned with relative response at room temperature, such thermally-induced differences are considered outside the scope of this review.

2.2.4 Forest hardening

The final strengthening mechanism to be discussed is forest hardening. As a crystal is plastically deformed it becomes increasingly difficult to cause further deformation, which is a quality known as strain (or work) hardening. As discussed above, plastic deformation causes the movement and production of dislocations. Dislocations initially glide freely along the primary slip plane, however at larger strains a second slip system can activate allowing for dislocations on two different planes to encounter each other. For some slip configurations it can be energetically favourable for a sessile lock to be formed. These are junctions between the slip planes of the two combining dislocations and they act as obstacles to further dislocation motion. As the dislocation density increases during plastic deformation so does the density of junctions, thus giving rise to strain hardening via forest hardening.

If local stresses are sufficient it is possible to destroy a junction, enabling dislocations to cross one-another. The critical stress required to do this is inversely proportional to the distance between obstacles, which in turn scales with the inverse square root of the dislocation density. This leads to the expression for CRSS that was included in Eq. 2.11 developed by Taylor,

$$\tau_{CRSS} = \alpha G b \sqrt{\rho_f} \tag{2.20}$$

where α is the average value of junction strength (over all possible slip configurations) and ρ_f is the forest dislocation density. Establishing the value of α is difficult since there are a wide range of possible dislocation interactions, however for FCC crystals an average value of 0.35 has been estimated from both theoretical and experimental studies [36, 37].

As previously mentioned, for FCC materials it is energetically favourable for glide to occur through the movement of partial dislocations with a stacking fault ribbon between them. The

product of the intersection of two partial dislocations forms in the $< 110 >$ direction between stacking faults lying on two of the $\{111\}$ planes [6]. Since the burgers vector of this resultant partial dislocation is perpendicular to the dislocation line, it cannot be in either of the $\{111\}$ planes containing the stacking faults and is thus trapped. Along with the two partials from which it originated, this forms a sessile junction called a Lomer-Cottrell lock that is a strong obstacle to further dislocations encountered on the same slip plane.

There are several physical processes that are not accounted for in this model of forest hardening, however. For example, when dislocations of opposite sign come within a critical distance of each other they annihilate and would therefore not contribute towards an increase in dislocation density. The dislocation density is also often taken to be homogeneous, which does not reflect the formation of dislocation cell structures during deformation that have been commonly observed experimentally for multiple materials (e.g. [38, 39]). Finally, when a dislocation lock is formed it is also able to create a new spiral source. This would have the effect of enabling further deformation to be accommodated, as opposed to strengthening the material.

2.3 Extrinsic length-scale effects

The previous sections have demonstrated how microstructural features and the intrinsic length-scales associated to them can strengthen a metal. In addition to this it has been shown that the length-scale of the test itself, which is associated to the geometry and size of the specimen, also changes the measured material strength. This so-called extrinsic size effect has been observed for various mechanical testing techniques. Some of the earliest experiments were performed on thin whiskers [40], where it was found that the tensile strength decreased with an increase in whisker diameter. Following similar observations of the size effect in indentation and wire torsion experiments, Fleck and Hutchinson [41] developed a strain gradient plasticity (SGP) theory. This theory was based on the idea that GNDs must be produced during testing in order to accommodate strain gradients during plastic deformation. At smaller test dimensions plasticity is confined to a smaller volume introducing a greater strain gradient and thus a higher GND density, causing an increase in hardness. However, size effects are also present in pillar compression tests, for example those performed by Uchic *et al.* [42]. For pillars the GND density is limited due to the lack of confinement of the deforming volume, indicating that SGP

theory cannot be solely responsible for such size effects. Micro-cantilever bending experiments performed by Motz *et al.* [43] demonstrated similar results, where the SGP model could not fully explain the inverse dependence of flow stress on the beam thickness. They suggested that two additional mechanisms - dislocation source limitation and stresses due to dislocation pile-up along the beam centre - must also be taken into account to fully describe the size effect.

The main focus of this review on extrinsic size effects will be the indentation size effect (ISE), since this technique was used extensively in this work. Pillar compression testing will also be covered, particularly in its application with irradiated material.

2.3.1 Berkovich indentation

Indentation testing using a pyramidal indenter tip was first employed in the 1920's with the development of the Vickers hardness test [44]. This method relied on a measurement of the residual indent impression by imaging with an optical microscope after the load had been removed. By the 1980's instruments had developed greatly, with the ability to continuously measure load and displacement allowing the calculation of contact area, and thus hardness, throughout the test cycle [45]. Shortly after this development it was shown that by fitting a linear line to the unload curve elastic properties could be calculated [46–48], however it was later found that a more accurate and "*physically justifiable*" analysis could be achieved by fitting a power law relation [49]. It is the latter of these approaches that has formed the basis of Berkovich indentation methods to obtain hardness and elastic modulus measurements on a range of materials. Due to the sharp tip, and hence the extremely small penetration depths that can be achieved, Berkovich indentation has proved particularly popular for testing thin films [50–52] and ion-irradiated layers [53–55].

Berkovich tips have self-similar tip geometry, meaning that they maintain a consistent geometry at all indentation depths. Correspondingly, Berkovich indentation measures at constant indentation strain throughout the test. For Berkovich indentation the size effect exhibits as an increase in hardness at decreasing indentation depths. Nix and Gao [56] applied the aforementioned (SGP) theory to the ISE, making the assumption that an indenter tip is accommodated by circular loops of GNDs having Burgers vectors in the direction normal to the sample surface, as shown in Figure 2.10.

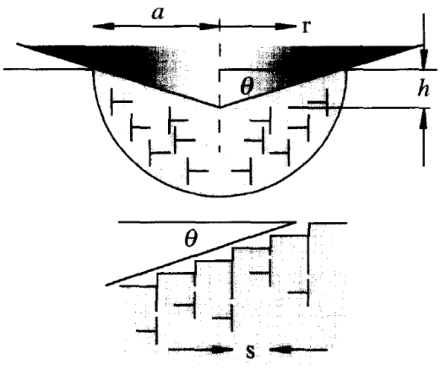

Fig. 2.10 Schematic of GNDs created during an indentation test. Reprinted with permission from [56].

From this they produced a model that has since been commonly applied to indentation testing, which takes the following form:

$$\frac{H}{H_0} = \sqrt{1 + \frac{h^*}{h}} \tag{2.21}$$

where H is the hardness measured at any given depth h. H_0 is the bulk (size independent) hardness, which is calculated as

$$H_0 = 3\sqrt{3}\alpha G b \sqrt{\rho_s} \tag{2.22}$$

where ρ_s is the density of statistically stored dislocations, α is a geometrical constant (generally taken to be 0.5), G is shear modulus and b the Burgers vector. h^* is a characteristic length based on the indenter shape as well the material and is calculated as,

$$h^* = \frac{81}{2} b \alpha^2 \tan^2\theta \frac{G}{H_0}^2 \tag{2.23}$$

The hardness value used in the above equations is effectively a measure of mean pressure at maximum load,

$$H = \frac{F_{max}}{A} \tag{2.24}$$

where A is the projected contact area between indenter tip and sample. In instrumented indentation the contact area is calculated from the contact depth using a tip area function, which does not take into account differences in the elastic-plastic response from the sample that can lead to significant piling-up or sinking-in of material around the indenter tip. Errors in the value of A can greatly alter hardness results as well as the calculation of elastic modulus. McElhaney *et al.*

[57] addressed this issue in copper by determining contact compliance as well as imaging indent impressions in the SEM to accurately measure contact area. They found that in strain-hardened copper the ratio of measured contact area to that determined from the tip area function was over 1.2, indicating significant pile-up and resulting in erroneously high measured hardness.

It has been shown that after correcting for pile-up there can be significant deviations from the Nix-Gao theory. Lim and Chaudhri [58] performed Berkovich indentation experiments over a range of indenter loads on two copper samples, using atomic force microscopy (AFM) to image the residual indent impressions from which the actual projected contact area was measured. They demonstrated that for the work-hardened copper there was not a linear relationship between the inverse of indentation depth and area-corrected hardness squared. The annealed copper, however, exhibited a consistently decreasing hardness with increasing indentation depth. The authors suggest that this demonstrates the importance of the stress-strain behaviour of the material, something that is generally not considered in Berkovich indentation since this technique measures at constant strain.

Various modifications have since been made to the SGP model to better reflect what is observed experimentally. For example, Durst *et al.* [59] consider how the plastic zone size beneath an indent would change depending on the material by introducing a scaling factor 'f'. If taken to be unity in the original Nix-Gao model, the authors find a better fit to experimental data can be achieved with $f = 1.9$. The authors propose that this scaling factor is representative of the area within which the strain is sufficiently high to enable the initiation of plastic deformation. A maximum allowable GND density has also been employed [60] to model nanoindentation at small indentation depths, where measured hardness is generally significantly lower than that predicted by the Nix-Gao model. This overcomes the issue of infinite hardness at indentation depths approaching zero and is physically justifiable since there will be a strong repulsive force between GNDs, pushing them beyond the hemispherical region considered (Figure 2.10). In [60] the maximum GND density was determined experimentally to be on the order of $10^{16} m^2$.

Alternatively, it has been suggested that the ISE in Berkovich indentation is related to changes in the primary deformation mechanism. Rester *et al.* [61] measured crystal orientations in the volume beneath nanoindentations made in Cu and it was found that larger misorientations were present beneath deeper indentations than shallow indentations. They propose that for big indentations, such large misorientations were due to dislocation pile-up near the interface

between sample and indenter tip, which imposed a back-stress on sources. For shallow indents, the region in which sources can be activated is reduced therefore the stress required to push previous dislocations away from the indenter tip is greater due to a shortened dislocation segment length. The authors thus produce a model similar to the Hall-Petch relation, with deformation volume replacing grain size, which showed good agreement with experimental data.

2.3.2 Spherical indentation

Indentation with a sphere dates back to 1900 when the eponymous Brinell hardness test was developed [62]. Shortly after this, in 1908, Meyer's hardness was defined [63] as the maximum load applied by a spherical indenter divided by the projected area of the indent. This was as opposed to the surface area of the residual indent used in the calculation of the Brinell hardness number. Meyer's law was also established at this time, which is an empirical relationship between applied load, P, and the indentation diameter, d,

$$P = kd^n \tag{2.25}$$

where k is a material constant and n is a parameter to express the degree of strain hardening in the material.

Unlike for the Berkovich tip the geometry of a spherical indenter is not self-similar, therefore indentation strain varies with penetration depth. It was shown by Tabor [64] that an indentation stress-strain curve could be produced, with stress equivalent to $P_m/2.8$ (where P_m is mean indenter pressure) and indentation strain as $0.2a/R$, where a is the contact radius and R the indenter tip radius. The shape of such indentation stress-strain curves was found to be analogous to those produced by uniaxial tensile tests but without the requirement of such a large volume of material to perform the test. In this work Tabor used large indenter tips and tested relatively soft metals, therefore the indentation size effect was not evident. This has also been demonstrated by Lim *et al.* who performed tests in oxygen free Cu [65].

Related to the above, another benefit of spherical indentation over indentation with a sharp tip is that contact is initially elastic, followed by yielding, plastic flow, and fully plastic deformation as load increases. As was seen for Berkovich indentation, the advancement of instrumented indenters in the 1980's enabled load-displacement data to be collected throughout the duration

of a test, thus enabling this full range in behaviour to be observed. Field and Swain [66] first developed a model that could simulate the behaviour during spherical indentation provided that some main material parameters, including Young's modulus and Poisson's ratio, were known. Based on Hertzian contact mechanics [67] between a ball and infinite half-space and using Sneddon's theory for elastic displacements [68], this model allowed the contact depth to be calculated from the unloading portion of the load-displacement curve. By performing multiple cycles and assuming that reloading is completely elastic, hardness measurements could be made at increasing depths for a single indent. Additionally, if the tip area function can be obtained then the elastic modulus of the material can also be determined. A now commonly-used method to do this was established by Bushby [69] who used indentation into four reference materials of known modulus and hardness to find the tip radius as a function of indentation depth.

More recently there has been a renewed interest in the possibility of using spherical indentation as a substitute for uniaxial testing to produce flow curves from which mechanical properties can be inferred [70, 71]. Being able to produce large quantities of data at high-throughput from reduced sample volumes has important applications in the nuclear industry in particular, where samples are generally limited in size. Spherical indentation has been shown to successfully characterise shallow ion-irradiated layers [54, 72] and proton irradiated steel [73], however there are still some issues surrounding the interpretation of data from tests such as these and spherical indentation in general. For example, the absolute definition of stress and strain is still under debate [74] and there are various models used to determine properties from the strain-strain curves [75–77]. Results have also been shown to be rate-dependent, as demonstrated by strain-rate jump tests carried out by Leitner *et al.* [78].

In spherical indentation the ISE goes with indenter tip radius, with measurements from smaller tips exhibiting higher indentation stress than from larger tips [65, 79]. The SGP theory discussed above for Berkovich indentation was extended to apply to spherical indentation by Swadener *et al.* [80], who modified Eq. 2.21 to express the dependence of hardness on tip radius,

$$\frac{H}{H_0} = \sqrt{1 + \frac{R^*}{R_p}} \tag{2.26}$$

where R^* is the material length scale and R_p is the radius of the residual indent impression. Experiments were carried out using five indenter tip radii in iridium and the hardness at

$a/R = 0.05$ compared to that predicted from Eq. 2.26. Although the authors claim there is a reasonable agreement between experiment and model, only three of the five data points lie discernibly along the model curve for a single set of parameters, and the smallest tip ($R = 14\mu$m) diverges considerably. The inapplicability of the model for small R is discussed further in [81] and shown in Figure 2.11. There were also several potential sources of errors in the methods used to produce the experimental data. For example, the use of different tip materials (diamond, sapphire, and steel) and the lack of contact area correction to account for pile-up.

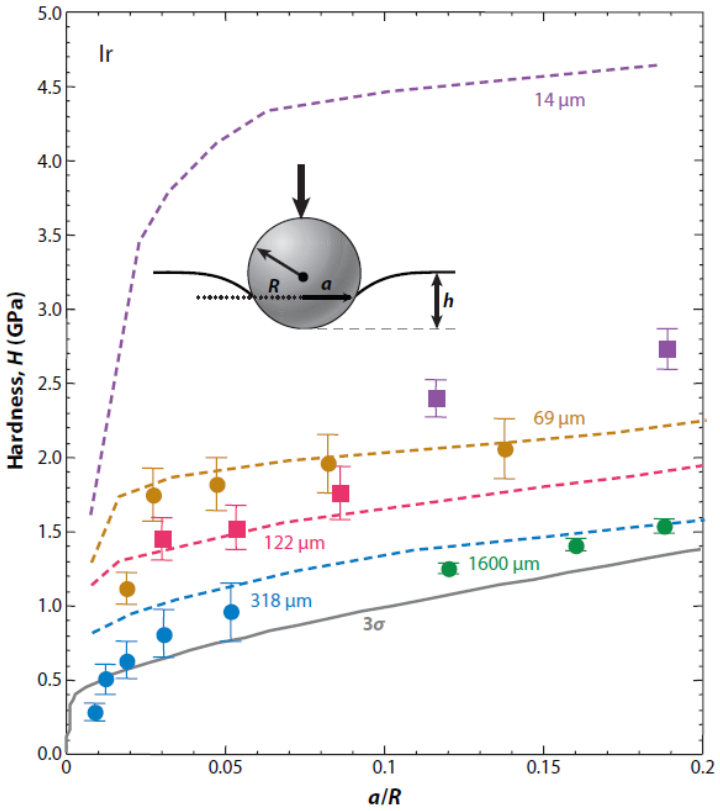

Fig. 2.11 Experimental data (solid markers) from spherical indentation in an Ir alloy using a range of indenter tip radii. The dashed lines are model predictions based on strain gradient effects. Reprinted with permission from [81].

Most significantly, a size effect is also seen in the yield stress both experimentally [82] and as predicted from finite element analysis simulations [83]. Since there is no plastic strain gradient, and hence no GNDs, at yield this effect cannot be explained by SGP theory. It is not always straight-forward to define the yield point for metals as the transition from the elastic regime often occurs at low indentation strain and is therefore beyond the capabilities of the indenter to record at low load measurements. To address this, a method was developed by Zhu

et al. [84] to infer the yield point by extrapolation of the plastic data back to the elastic line (see Figure 2.12). This was shown to be applicable to metals and the authors find that the yield strength is inversely proportional to $\sqrt[3]{R}$, where R is the indenter radius.

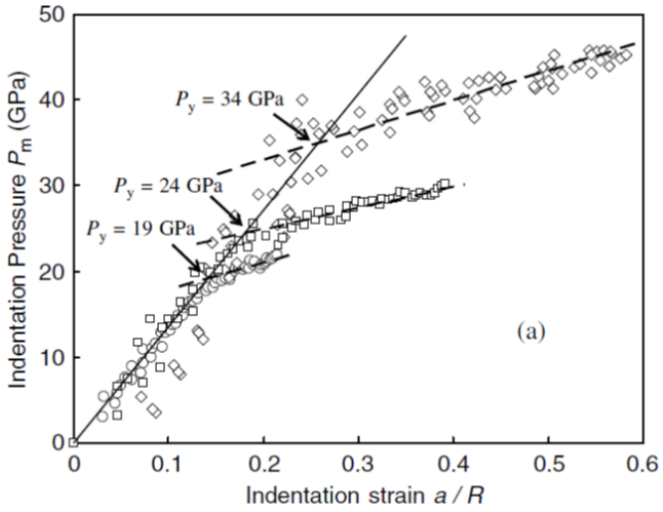

Fig. 2.12 Spherical ISE in αAl_2O_3 using tips of radii 0.5 μm (diamonds), 3 μm (squares), and 10 μm (circles). Reprinted with permission from [14].

2.3.3 Micro pillar compression

Uniaxial compression testing using micron-sized pillars is a relatively recent addition to the range of mechanical test techniques. First introduced by Uchic *et al.* [85], pillar compression was designed to explore sample size effects in the absence of strain gradients. Some of the earliest studies into specimen size effects already tested this; in the 1950's thin whiskers were used for tensile and torsional testing [40], however this technique required whiskers to be grown, which restricted its application to certain materials. The same does not apply to pillars, as illustrated by Uchic who introduced a method using FIB milling [86] that enabled the site-specific fabrication of pillars in virtually any material. Since there is no constraint on the deformed material during compression of a pillar there are no strain gradients, hence these types of tests allow other mechanisms responsible for the size dependence in CRSS to be explored. For example, several studies on pillar compression experiments in gold [87–89] suggest that the high observed strengths in the smallest diameter pillars (400 nm) may be due to dislocation starvation. Dislocations can only travel a short distance before being able to escape at the free

surfaces, thus the overall dislocation density becomes reduced in small geometries leading to high stresses required to nucleate new sources for further deformation to take place.

To characterise the sample size effect in pillars the yield (or flow) stress is often plotted against pillar diameter on a log-log plot. A straight line fit of the form Ad^{-x}, where A is a constant and d is sample size, can then be made to obtain a value for the scaling law exponent, x (see e.g. [88, 90]). The value of this exponent has been found to be material-dependent and range anywhere between zero and one. As part of a review on size effects, Greer *et al.* [20] compiled a substantial amount of data from micro- and nano-compression experiments performed on Au, Cu, Ni, and Al, which can be seen in Figure 2.13. By scaling the shear flow stress by shear modulus a universal power law exponent of 0.6 was found for these FCC metals. There was a great deal of scatter in the data, which was attributed to the initial microstructure but only discussed qualitatively. One of the main conclusions of this study was that for micron-sized pillars containing multiple dislocations the length of single-arm sources operating within the sample defined strength, and the limits imposed by pillar dimension leads to the observed size effect. It should be noted that there is no physical basis for a exponential scaling law and that a 'fit to the data' does not assist with the understanding of fundamental behaviour.

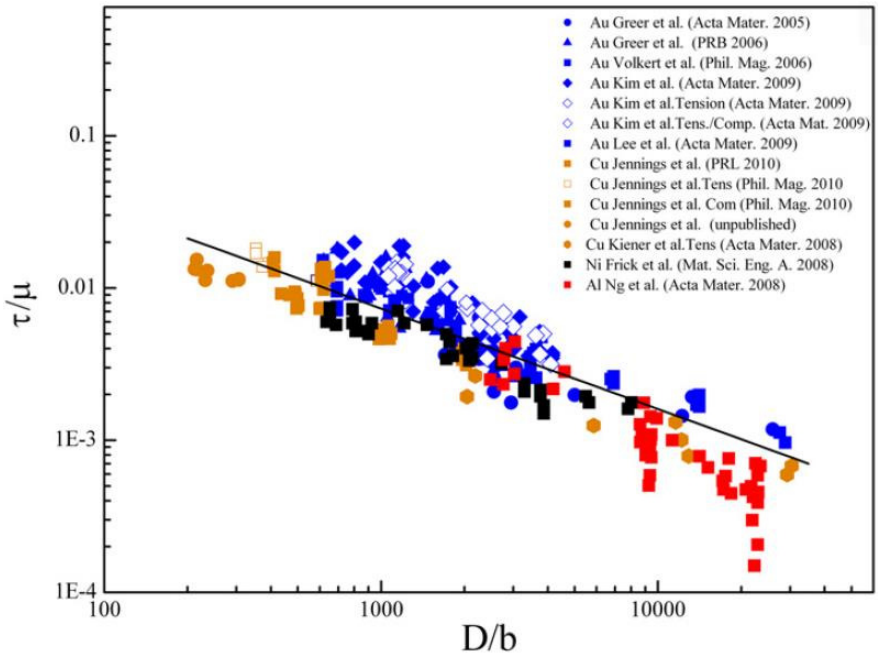

Fig. 2.13 Shear flow (normalised by shear modulus) from FCC micro- and nano-pillars in compression and tension, plotted against pillar diameter (normalised by Burgers vector). Reprinted with permission from [20].

The idea of a scaling law exponent has been the focus of many other studies. Korte and Clegg [91] explored the relationship between the exponent and bulk shear yield stress, τ_0. Comparing data from literature on FCC, body-centred cubic (BCC), and ceramic materials it was identified that the magnitude of the exponent decreased as τ_0 increased. This implies that the size effect is less dominant in materials with a higher intrinsic strength. In addition to this, even for a single material system a variation in exponent can be found depending on crystal orientation and whether a hard or soft slip system operates during the test. Phani *et al.* [92] developed a model to demonstrate that the behaviour of pillars depends on the existing dislocation population. Both the spatial distribution and activation strength of dislocations was randomised in a statistical model from which yield strength was then calculated. The model predicted strengths that were bound by two limits - the upper bound being the theoretical (dislocation-free) strength and the lower bound being bulk strength. The extrinsic size effect indicates the transition between these two limits as a function of specimen length, with the scaling exponent simply depending on bulk strength and sample size without providing information on the deformation mechanisms. Monte Carlo simulations also demonstrated scatter within these bounds, which is observed experimentally and purely reflects the statistical variation in dislocation density and arrangement. Such scatter was even evident for very small specimens, as shown in Figure 2.14.

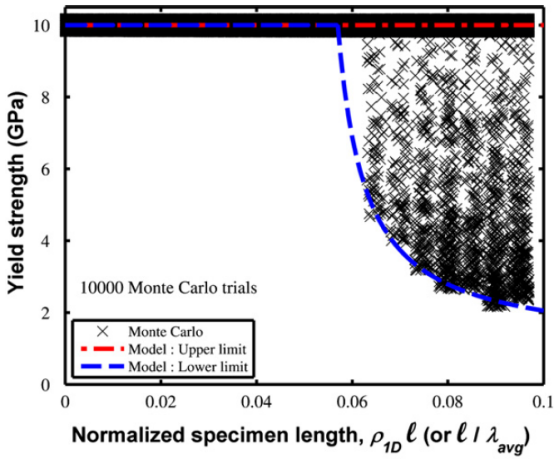

Fig. 2.14 Scatter in yield strength predicted by model (dashed lines) and Monte Carlo simulations (markers) for reduced specimen lengths. Reprinted with permission from [92].

The current leading theory of size effects in pillar experiments is that of source size. CRSS is defined by the stress required to activate dislocation sources, and plastic flow requires significant dislocation multiplication. In the case of a double-pinned Frank-Read source an

ejected dislocation will be truncated by the sample dimensions, thus becoming a single-ended source as shown schematically in Figure 2.15. The arm length determines the critical stress for yield and hence smaller pillars can be expected to exhibit increased strength. It was proposed by Parthasarathy *et al.* [93] that sample size strengthening is hence a result of dislocation truncation. They developed a theory to relate CRSS from pillar compression experiments to the dimensional constraints that prevent a dislocation source from operating. In this work they derive the following equation,

$$CRSS = \frac{\alpha Gb}{\bar{\lambda}_{max}} + \tau_0 + 0.5Gb\sqrt{\rho_{tot}} \tag{2.27}$$

where α is a geometrical constant related to the character of the dislocation, λ_{max} is the source length, τ_0 is the friction stress and ρ_{tot} the dislocation density. Existing mobile dislocations in the pillar quickly exit at free surfaces and dislocation multiplication is required to accommodate deformation. In the original analysis only the pillar dimensions are considered to confine dislocation sources but it is reasonable to extend this to the case of microstructural features, which would also reduce the source length.

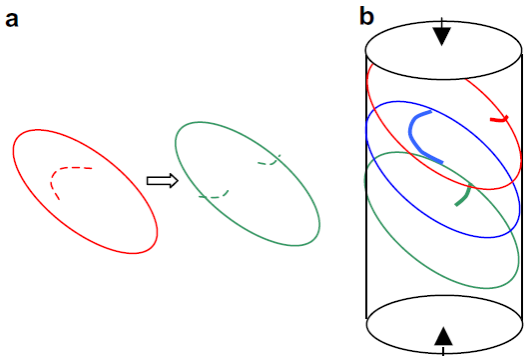

Fig. 2.15 (a) The double-pinned Frank-Read source can become single-arm (spiral) sources in a finite sample; (b) is representative of this in a pillar sample, where the longest source (blue) will define the CRSS. Reprinted with permission from [93].

The idea of a variable scaling law exponent has been critiqued by Dunstan and Bushby [94]. They demonstrate that only a small degree of scatter in the data is required for straight lines of very different slopes to be fit to a log-log plot; since each pillar inherently gives a result dependent on its initial microstructure, as discussed above, there will always be scatter in the data. This leads to wide variations in the scaling exponent that may fit the model whilst not necessarily supporting it. In line with the source curvature theory, they suggest that it should

consistently be unity since the stress required to bend a dislocation to a radius of r goes as r^{-1} (see Eq. 2.8). This predicts the minimum strength at a given length scale, which is equivalent to the lower bound predicted by Phani *et al.* [92]. Physically, this minimum strength represents the energy required to operate a single dislocation source within the confined space. Evidence supporting this can be seen in Figure 2.16, where no data - collected from a range of experiments, including pillar compression, wires in torsion and tension, and foils in flexture - is found below the solid line. This line defines the minimum strength,

$$\varepsilon_y = 1.5 l_{eff}^{-1} + G^{-1}\tau_0 \tag{2.28}$$

where l_{eff} is a length scale that combines sample and microstructural dimensions (see e.g. [95, 96]), and G and τ_0 are as previously defined. This physically-based result demonstrates that minimum strengths should be predictable for any given length-scale, which is an important aspect of material engineering. Secondly, the fact that this lower bound appears to be common to a range of experiments suggests that all size effects have the same underlying basis.

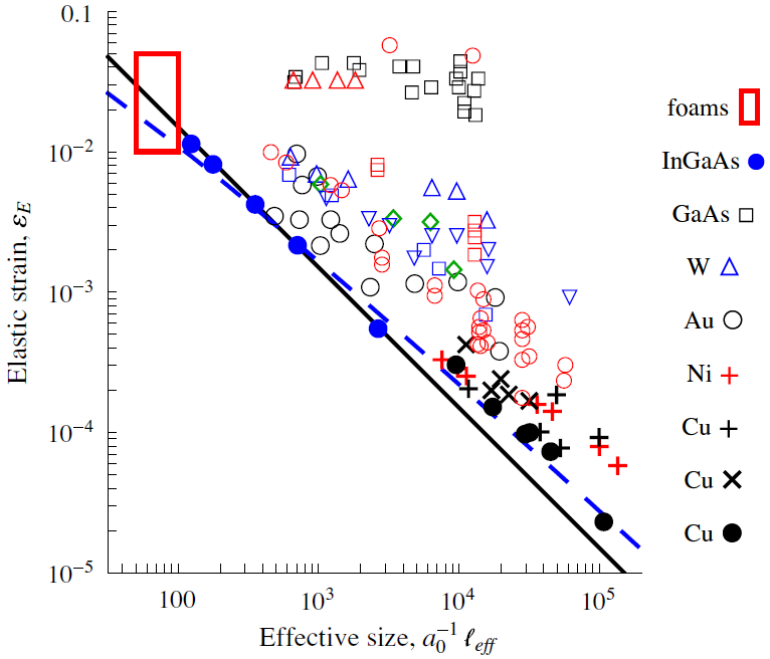

Fig. 2.16 Elastic strain versus effective size using data from a wide range of experiments on pillars, wires (in torsion and tension) and thin foils (in flexture). The solid line is equal to $1.5 l_{eff}^{-1}$. Reprinted with permission from [94].

A comparison between results from 3D DDD simulations and a large amount of data from physical experiments was carried out El-Awady [97]. The aim was to evaluate the applicability

of a generalised size-dependent model that can take into account pillar size (in the paper referred to as 'crystal size') and dislocation density. Additionally, since dislocation movements are tracked in DDD simulations they are able to give further insights into the evolution of plasticity deformation mechanisms. Figure 2.17 summarises the results of this study, showing the shear strength, τ, (normalised by shear modulus, μ) versus dislocation density, ρ.The best fit to both simulated and experimental data was found to be,

$$\frac{\tau}{\mu} = \frac{\beta}{D\sqrt{\rho}} + \alpha b\sqrt{\rho} \tag{2.29}$$

where $\beta = 1.76 \times 10^{-3}$ and $\alpha = 0.57$ are both dimensionless constants, D is crystal diameter, and b is the Burgers vector. The authors propose that the initial regions displaying negative correlation are indicative of dislocation starvation followed by single-source strengthening. Although not expressly stated, the minima of each curve should represent the case of only a single source present within the crystal, which is in fact equivalent to the minimum strength evaluated by Dunstan and Bushby using Eq. 2.28. Finally, for higher dislocation densities deformation is controlled by what the authors call "exhaustion hardening" and forest hardening.

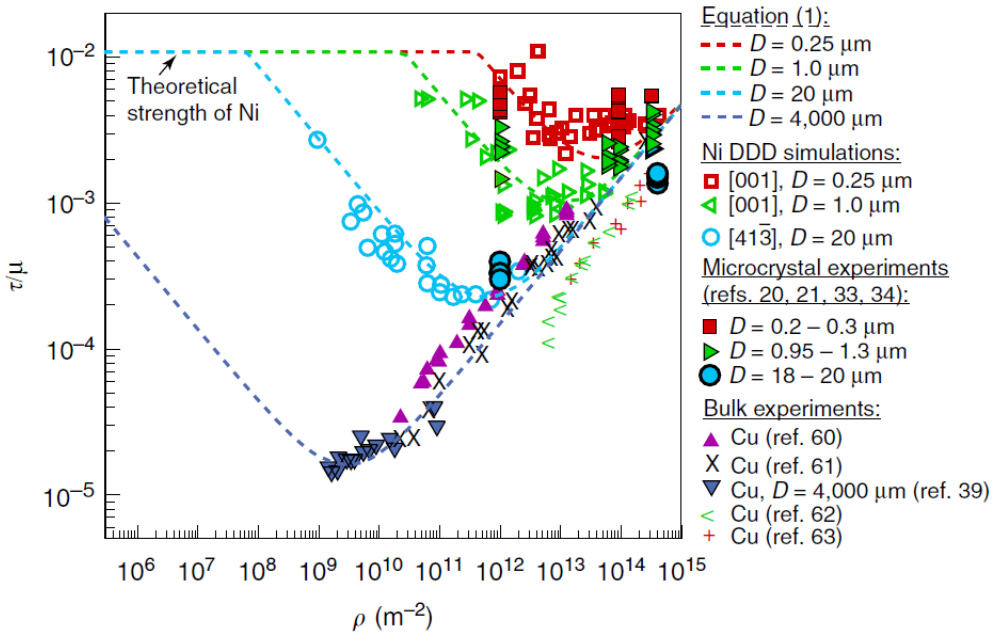

Fig. 2.17 Model predictions and experimental data for shear strength (τ), normalised by shear modulus (μ), versus dislocation density (ρ). The legend can be referred to for crystal size (D) and material. Reprinted from [97].

2.4 Interaction between length scales

Since the materials used for industrial applications are rarely single crystal pure elements, it is important to understand how microstructural length-scales interact with the extrinsic size effects that have just been discussed. Hou *et al.* [98] performed spherical indentation tests on copper samples having a range in grain size using indenter tips of radii between 3 and 20 μm, as well as Rockwell tests with a 200 μm radius indenter. Doing this allowed them to observe the interaction between the ISE and the Hall-Petch effect over a wide range of length-scales. The authors suggest that these two size effects can be combined in quadrature to find a single effective length parameter, D, using the following equation:

$$\left(\frac{1}{\sqrt{D}}\right)^2 = \left(\frac{K_1}{\sqrt{a}}\right)^2 + \left(\frac{K_2}{\sqrt{d}}\right)^2 \tag{2.30}$$

where K_1 and K_2 are fitting constants, a is the contact radius, and d is mean grain size. Doing this resulted in indentation pressure at $a/R = 0.25$ for different radius indenters falling along a single line when plotted against $D^{-1/2}$. This relationship was empirically determined, however it was proposed that because K_1 and K_2 were found to have similar values, both close to unity, there may be one underlying mechanism behind both strengthening effects. This work also demonstrated that the Hall-Petch effect is not apparent when the mean grain size of the material is greater than ~6 times the contact radius. This is because the zone size of the indentation does not interact with grain boundaries at these sizes.

Expanding on their previous work, Hou and Jennett [99] later modified Eq. 2.30 in line with slip-distance theory. This theory was originally based on dislocation-dislocation interactions and is based on the idea that plastic strain is dependent on the mean free path of a dislocation moving through a crystal. A new constitutive equation for the effective length parameter was defined as,

$$\frac{k_{HP}^2}{D} = \frac{k_1}{a} + \frac{k_2}{d} + k_3\sqrt{\rho_s} \tag{2.31}$$

where k_{1-3} are scaling parameters and $\sqrt{\rho_s}$ is the averaged spatial frequency of pinning points, for example impurities or sessile dislocations. This was then combined with the original

Hall-Petch equation (Eq. 2.9) to produce the following model for indentation hardness,

$$P_m = P_y + \left(\frac{k_1}{a} + \frac{k_2}{d} + k_3 \sqrt{\rho_s} \right)^{0.5} \tag{2.32}$$

where for a constant strain P_m is the mean indentation pressure and P_y is the size-independent yield stress of the material. Simulated values of P_m over a range in indentation depth was found to correspond well with experimental data from Berkovich data from single crystal and polycrystalline copper of different grain sizes. Similarly good fits were achieved for spherical data produced with different tip radii, which is perhaps unsurprising given the number of fitting parameters. In this model it is suggested that strengthening at small scales is due to an increase in the spatial frequency of pinning defects and reduction in plastic zone size of indentation, which combine to cause strain-hardening.

Similar to the Parthasarathy theory discussed in the previous section, Dunstan *et al.* [95] considered size effects in the context of dislocation source restriction. They propose that critical thickness theory could be applied to explain both the structure size effect and grain size effect seen for thin wires in torsion. In a structure of width h containing grains of average diameter d the average spacing between mobile dislocations is defined as,

$$l_{eff}^{-1} = \sqrt{\rho} + h^{-1} + d^{-1} \tag{2.33}$$

where ρ is the mobile dislocation density. This is very similar to the format of Eq. 2.30 but with a different underlying physical basis. As grain size and/or structure size decrease then so does the average spacing between obstacles (or free surfaces). Since dislocations need space to operate it is reasoned by the authors that "*the physical principle determining the elastic limit and early strain hardening of a soft metal is the constraint that size, whether grain size or structure size, puts on dislocation curvature*". In a recent review paper [100] this theory was re-visited where its applicability to a wider range of data was demonstrated.

2.4.1 Irradiated materials

When a material is subject to irradiation within a nuclear reactor, defects are produced within the structure due to collisions with either the neutrons or the atoms they have displaced. The

initial types of defects formed are typically point defects, such as vacancies or intersitials, and line defects such as dislocation loops [101, 102]. Over time these defects accumulate and can result in the formation of voids or bubbles, which also evolve and migrate [103, 104].

Any changes in mechanical properties during the lifetime of a reactor component must be understood to ensure its suitability in the role for the expected time period. Studies on irradiation defects are confined to small scale testing techniques for two main reasons: to reduce the sample activity, or because of the limited volume of irradiated material. The former of these is primarily driven by safety concerns, whereas the latter is often because irradiation with ions or protons has been used. Ion-irradiation has commonly been used as a surrogate for neutron irradiation [105, 106] since it has the advantage of not being activated, however damage typically only extends a few microns into the surface.

Irradiation defects generally increase the yield strength of a material via Orowan hardening due to dislocation loops and irradiation-induced precipitates. It has been shown using indentation techniques that the hardness of an Fe-Cr alloy significantly increases following ion-irradiation [107] and the authors associate this hardening with the formation of Cr-rich precipitates that formed due to the clustering of chromium atoms. An additional study on the same material [54] emphasised the importance of data interpretation when testing such thin irradiated layers. Images produced by transmission electron microscope (TEM) of cross-sections through both Berkovich and spherical nanoindentations demonstrated that the plastic zone was reduced in the irradiated material compared to the unirradiated material, therefore the ISE is likely to also be contributing towards the observed increase in hardness.

Previous studies that have considered the coupled effect of varying both intrinsic and extrinsic length-scales include work by Hardie *et al.* on irradiated Fe6%Cr [108]. The spacing between microstructural obstacles (namely dislocation loops) varied between samples that had been self-ion or neutron irradiated; Berkovich indentation and micro-cantilever bend tests were then performed over a range of test dimensions. The results of nanoindentation demonstrated hardening for both irradiated samples, however it was found that for the smallest cantilever beams the extrinsic size effect obscured such hardening in the case of the ion-irradiated material. An attempt was made to extrapolate the micro-cantilever results to the macro-scale but this was found to be unsuccessful. The authors suggest that a more complex model is required that can account for multiple size effect mechanisms, such as the analytical model used in [43]

that includes the contribution from the pile-up of dislocations along the neutral axis as well as dislocation source starvation.

Pillar compression is also commonly used to test irradiated material. A study comparing nanoindentation and pillar compression in ion-irradiated material [109] demonstrated that each of these tests can yield different results. For example there was a difference in flow stress observed in nanoindentation but not in pillar compression. It was suggested that this was due to the relative deformation mechanisms, which in irradiated pillars was observed to be the formation of distinct slip bands whereas for indentation multiple slip systems can operate.

Kiener *et al.* [110] performed *in situ* TEM pillar compression of proton-irradiated copper in order to obtain more information on the deformation mechanisms during testing. They found that size-independent results could be achieved from samples as small as 400 nm. These results can be seen in Figure 2.18.

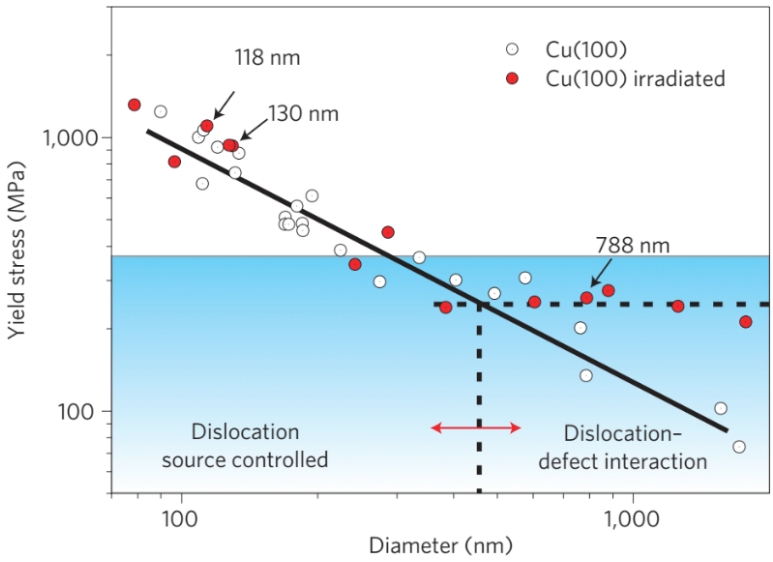

Fig. 2.18 Measured yield stress for irradiated (red) and unirradiated (open circles) Cu. Reprinted with permission from [110].

It was proposed that for irradiated pillars down to 400 nm in diameter the yield strength is determined by the interaction between dislocations and radiation-induced defects, in this case mostly stacking fault tetrahedra that act as barriers to dislocation cross-slip. Below this size the sample dimensions start to induce an extrinsic size effect as the stress required to initiate ever-smaller dislocation sources is more significant than the obstacle strengthening from defects. A similar result was found in pillar compression experiments on an ion-irradiated FeCr oxide

dispersion strengthened (ODS) alloy [111]. In this study the size effect due to pillar dimension was only observed for pillars $\leq$100 nm in diameter.

2.5 Rationale

The existence of size effects is now widely recognised in a range of mechanical test geometries. However, the material and test length-scales that give rise to this increasing strength with decreasing size are still not clearly understood. The work in this thesis attempts to address this issue in a series of experiments in which the length-scale of the materials and the test were systematically varied. The test length-scale was varied by using different indenter tip shapes in nanoindentation experiments, including Berkovich indentations over a range of depths and spherical indenter tips with different radii. The materials were chosen to allow the material microstructural length-scale to be varied in a controlled manner. Firstly, copper single crystals are used so that the only length-scale is that of the test and not the material (Chapter 4). Secondly, introducing alloys containing elements in solid solution and in the form of precipitates, in which the size and spacing of precipitates could be varied (Chapter 5). Thirdly, by introducing sub-micrometre grains into these materials by severe plastic deformation (Chapter 6). In Chapter 7, proton-irradiated material was introduced and tested by Berkovich indentation and micro-pillar compression.

The results from these experiments are aimed at answering the following research questions:

1. How does the plastic zone size beneath a spherical indent evolve with indentation strain as a function of tip radius?

2. Can the observed size dependence on material strength be explained by the dislocation source model, or do other interactions also have to be considered?

3. How can results from small-scale testing techniques be related to bulk-scale mechanical response, and hence provide engineering relevant data when sample sizes are limited?

Chapter 3

Materials and Experimental Methods

The processes used to prepare various materials and sample geometries tested in this study are described at the beginning of this section. The experimental techniques and analysis methods are then also provided.

3.1 Single crystal Cu

A high-purity (99.999%) single crystal copper sample was acquired from Goodfellow© with surface normal n=[010]. It came in the form of a cylindrical bar from which a single disc of approximate thickness 2 mm was cut. Standard mechanical polishing was performed using increasingly fine silicon carbide (SiC) papers, finishing with a 2.5 μm grit size (FEPA grade P4000), followed by electropolishing with Struers D2 electrolyte for 10 s. The electrolyte was rinsed off using deionised water, then rapidly dried using compressed air. The sample was finally mounted on a standard aluminium pin stub using Crystalbond® adhesive and silver paint. Work on this material is presented in Chapter 4.

3.2 CuCrZr

A 35 mm thick plate of Cu-1.0 Cr-0.06 Zr (wt%) was acquired from ZOLLERN GmbH & Co. The as-received material had been solution annealed at 970 (±10) °C followed by a water quench. Chemical composition was confirmed using XRF (results from this are in Table 3.1) and found to contain slightly less Cr than specified by the manufacturer (99.17 wt% Cu and

0.83 wt% Cr). The Zr content was below the limit of detection for this technique. From this plate seven blocks were cut; one was set aside and represents the solid solution case, whilst the remaining six were individually heat treated in a vacuum furnace, held at the following temperatures for two hours: 400, 480, 550, 600, 650 and 700 °C. Such heat treatments cause a coarsening of the Cr precipitates, as described by numerous previous studies [112–114].

Specimens of approximate dimensions 10 x 10 x 2 mm were cut from all blocks using a Struers Minitom (slow saw) and mechanically polished using SiC papers, with the final grade being P4000. For grain size analysis in the scanning electron microscope (SEM) the samples were subsequently mechanically polished using 1 and 0.25 μm diamond suspensions, followed by a chemo-mechanical polish using colloidal silica (Col-K) to produce a surface with minimal polishing damage. For indentation testing, a separate sample set was electropolished in order to produce a flat surface with minimal surface deformation and residual stress. Electropolishing was carried out using a nitric acid and methanol 1:4 mix held at –40 °C by submerging the beaker in a bath of liquid nitrogen. After electropolishing for 20 s at 2 A and ~30 V the samples were immersed in a beaker of cooled pure methanol, then rinsed with fresh methanol followed by ethanol and finally deionised water. They were then dried using compressed air. All samples were finally mounted on standard aluminium pin stubs using Crystalbond® adhesive and silver paint so that they could be imaged by electron microscopy.

Table 3.1 XRF results for bulk CuCrZr. LOD = limit of detection.

Cu (wt %)	**Cr (wt %)**	**Zr (wt %)**
99.17 ± 0.02	0.83 ± 0.02	LOD

3.3 Fabrication of thin films

For transmission Kikuchi diffraction (TKD) and transmission electron microscopy (TEM), electron-transparent thin samples were fabricated using two techniques: focused ion beam (FIB) lift-out and twin jet electropolishing. Thinned lift-out samples were also produced in single crystal Cu for plastic zone size characterisation.

3.3.1 FIB lift-out technique

A FEI (now Thermo Fisher Scientific) Helios 600i NanoLab dual beam SEM/FIB equipped with a gallium ion source was used to fabricate lamellae for TKD, EBSD, and TEM. The initial stages of the lift-out procedure were common to all samples. Firstly, a platinum layer was deposited over the lift-out location to prevent surface damage during subsequent stages. Material to either side was then removed using high beam currents until a thickness of ~2 μm was achieved. Undercutting whilst the sample was held at 45° to ion beam normal allowed the lamella to be lifted in-situ using a micromanipulator needle. The lamella was then mounted in a Cu TEM grid using further platinum deposition.

For EBSD samples, only one side of the foil needed to be polished. This was done with the sample initially tilted 2° to the ion beam direction to compensate for the Gaussian beam profile and reduce Ga implantation, which can result in poorer Kikuchi patterns during analysis. The sample was cleaned using decreasing beam voltages and smaller tilt angles until it was ~1 μm thick, with a beam voltage of 2 kV used to perform final polishing with the sample held at 7° to the beam direction. For TKD and TEM this thinning procedure was followed on both sides of the lamella until electron transparency at 10 kV was obtained. Polishing at 2 kV with the sample tilted at 7° to ion beam normal was then carried out on both sides.

3.3.2 Electropolishing

Using mechanical grinding to a final grade of P4000, squares of the CuCrZr sample set were ground down until they were approximately 300 μm thick. 3 mm discs were then punched from each of these and mechanically polished further on both sides to a final thickness of less than 100 μm. A Struers Tenupol twin jet polishing unit, with 1:4 nitric acid to methanol mix electrolyte held at -40 °C, was then used to create a central region of electron transparency in each of the discs.

3.4 Proton irradiation

Three CuCrZr sample conditions were irradiated: the as-received material, and samples that had been heat-treated at 480 °C and 650 °C. Specimens were cut to approximate dimensions of 14 x 14 x 3 mm and mechanically polished on one side before irradiation. Proton irradiation was

carried out at the Dalton Cumbrian Facility, Cumbria. To avoid any activation of the sample the lower energy ion accelerator 'BABY' was used, which is a pelletron ion accelerator [115]. Samples were secured onto the holder using a tantalum mask (see sample arrangement in Figure 3.1). Slits within the beam line then reduced the irradiated area to a 10 x 10 mm central region.

The radiation damage profile as a function of depth into Cu for protons was calculated using open source software SRiM [116]. All samples were irradiated at 1 MeV and 25 μA, generating a fluence of ~3.37×10^{18} ions/cm^2, for six hours. This produced an approximately uniform damaged region of 0.4 displacements per atom (dpa) in the first 5 μm of material. Despite the high current, active water cooling applied to the sample holder meant that the samples did not exceed 40 °C, with sample temperature bring measured using two thermocouples clamped between the sample and mask.

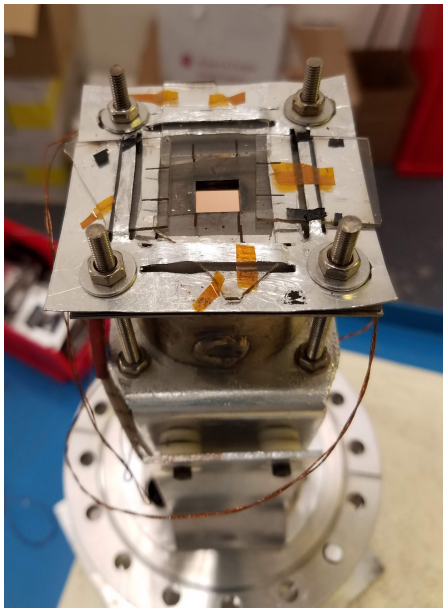

Fig. 3.1 Sample within irradiation holder for the BABY beam line.

3.5 Micro-pillar fabrication

A wire saw was used to cut samples of approximate dimensions 14 x 2.5 x 2 mm from both unirradiated and irradiated CuCrZr material in the three conditions (as-received and two heat-treated), which had already been polished on the face exposed to incident protons. The cut face of the sample edge was polished down to a Col-K finish to remove any residual cutting damage. Pin stubs were machined to cut away a portion of the top surface, leaving a lowered region

where the samples were attached using superglue. This resulted in the sample surface protruding no further than 1mm from the original top of the pin stub, and the sample edge aligned with the middle of the pin stub (see Figure 3.2). This positioning is required for the samples to comply with the in-situ indenter arrangement (see Section 3.14) where there is limited stage movement possible.

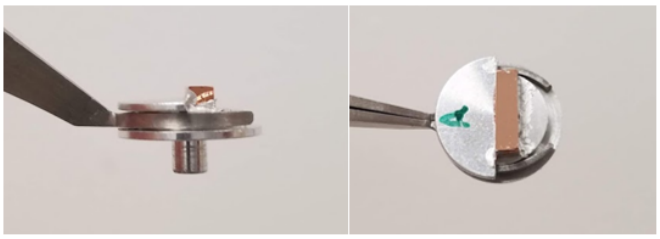

Fig. 3.2 Sample attached to modified pin stub for in-situ pillar compression testing.

A FEI Helios 600i NanoLab dual beam SEM/FIB was used to remove material and fabricate the pillars with a square cross-section. The micro-pillars were manufactured along one edge, within the first 6 μm of the irradiated surface (see Figure 3.3). This was so that for the proton-irradiated samples the pillars were contained within the uniform irradiated layer and, in both cases, to enable them to be viewed-real time during in-situ compression. To avoid re-deposition, milling was always performed on pairs of adjacent pillar edges and polishing with a low beam current on the final step reduced any significant Ga implantation from previous stages. Three sets of pillars with different dimensions (but constant width to height ratio of 1:2.5) were produced in all samples - three with pillar widths of 4 μm, and four each of widths 1 μm and 400 nm.

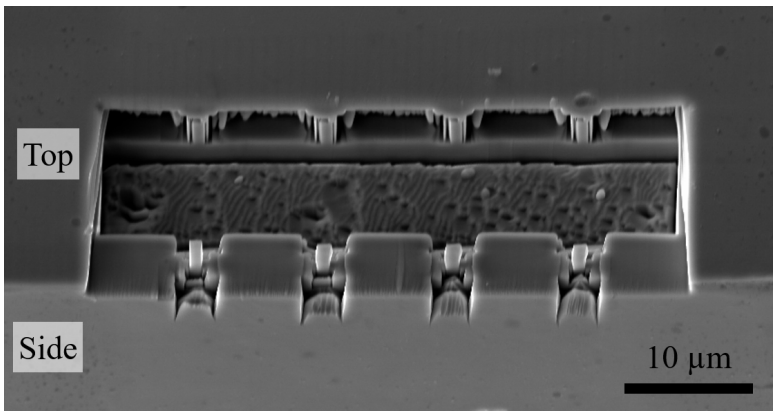

Fig. 3.3 Example pillar fabrication site.

3.6 High pressure torsion

Two samples were subjected to high pressure torsion (HPT) to produce a nano-grained microstructure [117, 118], which provided samples to investigate grain size. This work was carried out at the Erich Schmid Institute of Materials Science in Leoben, in Austria, in collaboration with Dr Daniel Kiener. Large sections were cut from both the as-received and 550 °C heat-treated blocks. These were subsequently machined to produce a set of discs of diameter 35 mm and thickness 3.5 mm. One disc of each material variety was then placed within the HPT mechanism, a schematic of which can be seen in Figure 3.4. Ten turns were made at a speed of $\frac{1}{15}$ rpm whilst applying a pressure of 4 GPa along the axis of rotation. A slow rotation speed was used so that there was no appreciable heating of the sample during fabrication. For grain measurement and indentation the material was mechanically polished using the same method for the other CuCrZr bulk samples, as described in Section 3.2, and mounted on pin stubs.

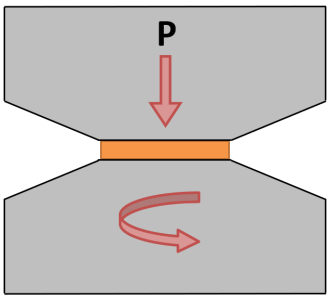

Fig. 3.4 Schematic of high-pressure torsion instrument.

3.7 Tube furnace annealing

After having produced a nano-grained microstructure in the as-received and 550 °C material via HPT, the grains were grown via annealing at two different temperatures. Two sections of approximate dimensions 15 x 4 x 5 mm were cut from both HPT samples using a Struers Minitom. A tube furnace (PTF three zone tube furnace, Lenton Thermal Designs) was used to anneal pieces of each material type at peak temperatures of 200 °C and 600 °C, with the furnace held at these temperatures for 10 minutes before cooling down. During annealing the samples were placed at the same central position within a quartz tube under vacuum (~1 mbar) and the temperature was measured at three points along the tube – the two furnace extremities and the centre point. Since cooling was achieved only by switching the heaters off it is important to note

that the time the samples were at high temperatures was considerable. Although it took only 20 minutes to raise the tube temperature to 600 °C , the time taken to cool down to 75 °C was 6 hours. For the heat treatment at 200 °C the cool-down time was 3 hours. Venting to air would have resulted in faster cooling times, however the samples would have built up a significant layer of oxide doing this.

3.8 Electron backscatter diffraction

A Tescan MIRA3 FEG SEM was used to perform electron backscatter diffraction (EBSD) and generate crystal orientation maps. EBSD maps are produced by scanning a focused electron beam over a highly tilted (typically 70 °) sample. The incident electrons interact within a small (10s - 100s nm^3, depending on the accelerating voltage) volume of the crystal lattice beneath the sample surface and those that undergo coherent Bragg scattering are elastically back-scattered. Some of the scattered electrons are collected on a phosphor detector and produce Kikuchi patterns, which are made up of bands that correspond to the crystal planes that caused Bragg scattering. Likewise, intersections of bands correspond to zone axes. The position and angle of Kikuchi bands are then measured in order to index the pattern and identify the crystal orientation. Automated software does this for every scanned point within a defined area in order to produce orientation maps. A Nordlys Max EBSD detector and AZtec 3.3 software, both Oxford Instruments, were used for this work. Grain size measurements were then made in Channel5 software Tango using the elliptical fit method with a grain boundary misorientation defined as 10 °. Only grains consisting of 10 or more pixels were included in the analysis and any grains located on the map border were ignored. Grain boundaries with a <111> misorientation (Σ3 twin boundaries) were also disregarded since dislocations can easily transmit through them and therefore should not contribute as a strengthening mechanism [119].

3.9 Transmission Kikuchi diffraction

Transmission Kikuchi diffraction (TKD) is a technique similar to EBSD in that it is performed using the same SEM detector. However, instead of collecting back-scattered electrons from the surface of a bulk sample, the electron beam scans a thin foil and forward-scattered electrons

that are produced from the back surface of the sample form Kikuchi patterns. An example of the sample arrangement can be seen in Figure 3.5. Due to a reduced interaction volume of the electrons used in TKD compared to EBSD, and a smaller sample tilt angle (for this work, 20 °), a much greater spatial resolution can be achieved, particularly in the longitudinal direction [120].

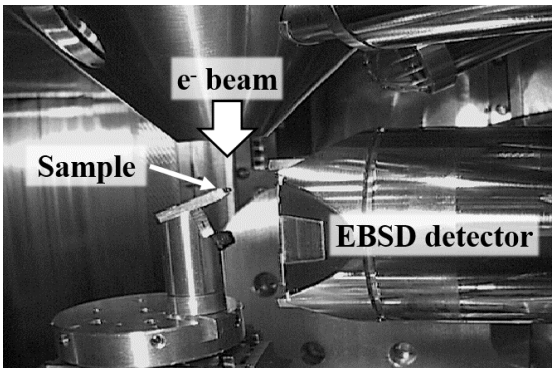

Fig. 3.5 TKD arrangement in the SEM chamber.

3.10 Measurement of plastic zone size

To characterise the deformed region beneath a spherical indentation imprint, strain mapping software CrossCourt4 (BLG Vantage, UK) was used. CrossCourt measures small elastic strains and lattice rotations through the cross-correlation of features within sub-regions of high-resolution Kikuchi patterns. When EBSD and TKD maps of indent cross-sections were acquired for strain mapping, Kikuchi patterns were saved for every pixel of the map. These were required inputs to the software, along with information on the crystal structure (i.e. FCC copper) and specifics on the detector arrangement derived through calibrations on single crystal silicon (most notably by how much a Kikuchi pattern shifts across the detector as a function of beam position).

Once opened in the software, a reference point was selected that represents a region of the material that has not undergone deformation, i.e. the original crystal structure. For indent cross-sections the reference was chosen to be a point near the surface of the sample (below the protective platinum layer) and as far away from the indentation as possible. For cross-correlation, 20 square regions of interest (ROI) were evenly distributed across the diffraction image. It is through the use of multiple ROIs that this technique is able to measure sub-pixel changes in the

pattern and thus high strain sensitivity of ~10^{-4} [121]. Cross-correlation was then performed within the software. Changes in lattice plane spacing are identified as elastic strain and shifts in the whole pattern are identified as a change in crystal orientation, i.e. a lattice rotation. A second pass at cross-correlation reduced the chance of erroneously high strain calculations.

Three infinitesimal rotation maps are produced in this way (alongside various other parameters that were not used for this work) that measure in-plane crystal rotations about the three coordinate space axes. The software uses a right-handed system, with axes labelled 1, 2, 3 having directions as given in Figure 3.6. The ω12 infinitesimal rotation maps representing rotations about the 3rd (sample normal) axis were used to observe the deformed region below an indent because these were most indicative of material that had been deformed to accommodate the indenter tip.

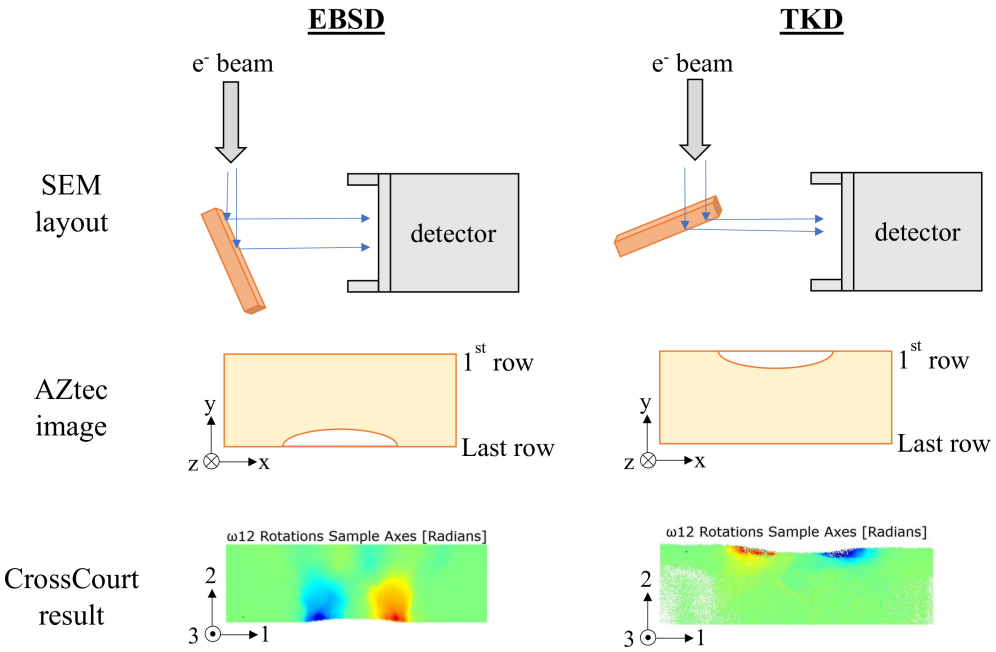

Fig. 3.6 Axis conventions used in EBSD, TKD, and CrossCourt.

3.11 Transmission electron microscopy techniques

In addition to traditional bright- and dark-field imaging in the TEM, two analytical techniques were used to characterise the Cr precipitate size and spacing across the CuCrZr sample set: energy dispersive X-ray spectroscopy (EDS), and electron energy loss spectroscopy (EELS). In

both cases the instrument was operated by Dr J. Lim, UKAEA using TEMs at the University of Manchester School of Materials Electron Microscopy Centre.

3.11.1 EDS

EDS was carried out using a 200 kV FEI Talos scanning-TEM (STEM) on samples produced using twin jet electropolishing, the specifics of which are given in Section 3.3.2. EDS is an analytical technique that identifies the chemical composition of a material. In the case of EDS within a SEM or TEM, it does this by subjecting the sample to a high-energy electron beam that can stimulate the excitation and emission of electrons. This leaves a hole in one of the inner atomic electron shells, which, when filled by an electron from a higher energy-state shell, results in the release of an X-ray of well-defined energy. These X-rays can be collected by a detector and the spectra analysed to identify any intensity peaks across a range of energies. The X-ray energies are characteristic of the distance between shells for specific species of atom, therefore each peak can be indexed to a particular element and shell transfer to establish the material composition. Chemical maps can be produced using this technique by scanning the electron beam over an area of the sample and collecting the X-ray spectrum for each pixel.

Multiple regions on each sample were imaged so that homogeneity across different grains and grain boundaries could be established. Maps were produced using the SuperX detector (Oxford Instruments) with four silicon drift detectors. The net Cr maps were subsequently handled within open source software 'FIJI' [114], where a Gaussian blur algorithm was applied to remove background noise, followed by thresholding to generate a new image with pixels of a brightness above a certain value (indicating Cr content) converted to black and all other pixels converted to white. Finally, the plugin 'Particle analysis' was used to analyse the binary image, with edge particles excluded from the analysis and a lower particle size selected so that as many precipitates as possible were captured without single pixels contributing towards the count. This plugin fits ellipses to every particle identified; average Cr particle diameter was thus calculated as the mean value of the major and minor ellipse diameters.

3.11.2 EELS

EELS was carried out using a 200 kV FEI Titan STEM on samples produced using the lift-out technique described in Section 3.3.1. This preparation technique was used because EELS results

are thickness-dependent and so benefit from the sample having consistent thickness throughout the mapped volume. During EELS analysis, as the electron beam passes through the sample it interacts with the material and can be inelastically scattered, loosing energy and momentum in the process. These scattered electrons can be collected by a spectrometer that generates an energy-loss spectrum containing two main features: a zero-loss peak (ZLP), created by electrons that have passed through the sample with negligible energy loss, followed by subsequent core-loss peaks that represent electrons that have lost energy due to interactions with the sample. As in EDS, the intensity peaks are characteristic of particular atomic shell ionisation events that identify the elemental composition of the sample.

In dual-EELS mode two spectra were acquired simultaneously: one to cover the low-loss region (-100 – 950 eV) that contained the ZLP and core loss peaks, and one covering the high-loss region (350 – 1375 eV) encompassing plasmon peaks. The convergence and collection semi-angles used were 21 ° and 62 ° respectively. Major and minor edge energies for Cu, Cr and Zr are given in Table 3.2. It was not possible to detect Zr since the edge peaks occur at high energies outside of the spectral range acquired, however for this analysis it was not required.

Table 3.2 Major and minor edge energies, as defined by Gatan [122], for elements considered in EELS analysis.

Element	**Major edges (eV)**	**Minor edges (eV)**
Copper	L_2 - 951 L_3 - 931	L_1 - 1096
Chromium	L_2 - 584 L_3 - 575	L_1 - 695
Zirconium	L_2 - 2307 L_3 - 2222	L_1 - 2532

Unlike EDS, peak-fitting is not automatically carried out within the software and there are several post-analysis steps that must be taken before the data can be interpreted. These steps were carried out within the software Digital Micrograph (DM) and are as follows:

- X-ray removal: high-intensity, single pixels caused by stray X-rays are removed from all spectra by defining an intensity threshold.
- Align zero-loss peaks: locate the zero-loss peak in one spectrum and use the DM tool ‘Align SI by peak’ to shift the spectrum so that the peak is at zero energy loss. Apply this correction to all spectra.

- Calibrate the spectrum to correct for zero peak position: applied only to the low-loss map.
- Compute the sample thickness: using the low-loss map, use the 'Compute thickness' function within DM to calculate relative and absolute thickness maps. Relative thickness is calculated using the log-ratio formula,

$$\frac{t}{\lambda} = \ln\left(\frac{I_t}{I_0}\right) \tag{3.1}$$

  where λ is the characteristic mean free path of the material, and I_t and I_0 are integrals over the entire spectrum and zero loss-peak, respectively. Absolute thickness was calculated using the assumption that the whole sample was Cu, for which $\lambda = 120$ nm.

Finally, a Python code (provided by C. Makepeace, Oxford Materials) that implemented an independent component analysis approach was used to produce Cr maps. It was based on a method described in [123], as cited in [124]. Analysis was performed using multivariate curve fitting, whereby the fine structure of edge peaks in the spectra were automatically fit with a function that contained a component expressing the decaying 'shoulder' signal on the high energy side. This allowed even small peaks to be extracted from the background signal of previous edges.

3.12 Atomic force microscopy

Atomic force microscopy (AFM) is a technique most commonly used to produce a 3D topographic map of a sample with very high spatial resolution [125]. It does this by rastering a sharp tip (apex radii are typically < 50 nm [126] and fabricated from silicon) over the sample surface, with the tip either directly in contact with the material (contact mode) or hovering just above it with a small applied oscillation (tapping mode). The sample is usually mounted on a piezoelectric stage to allow precise positioning in the x and y axes, and movement under the tip. The tip is mounted to a cantilever, which bends due to height changes across the sample profile; the deflections are measured by reflections from a laser focused on the back of the cantilever and this signal is converted into a height measurement.

A Veeco Dimension 3000 AFM in contact mode with a silicon tip of radius 8 nm (as supplied) was used to characterise deformation around a residual indent pit. The data was

analysed within open source software Gwyddion [127]. To correct for shifts in the fast scanning axis (x-axis) the 'Align rows' function was used and horizontal line defects were interpolated using surrounding pixels. Spots due to surface contamination were also removed but care was taken not to modify the shape of the pit or the pile-up around it.

3.13 Indentation testing

3.13.1 Vickers hardness testing

Vickers hardness testing is commonly used in industry as it is able to produce high-throughput hardness measurements and/or property mapping with a high level of automation. In this work a Leco LM-100 microindentation hardness tester was used to perform indentation on the CuCrZr sample set as a means of initial verification of a change in hardness due to the heat treatments. A force of 100 gf was applied to a square-based pyramidal tip with a half angle of 136/2° and held for 15 s after contact was made with the sample surface. The force was then removed and the residual imprint imaged using an optical microscope so that the contact area could be measured.

Vickers Hardness was calculated using the following equation:

$$HV = \frac{F}{A} \tag{3.2}$$

where F is the force applied in kgf and A is the contact surface area of the residual impression. A is calculated using the average of the two diagonal lengths, d, measured from the imprint,

$$A = \frac{d^2}{2sin(136°/2)} \tag{3.3}$$

where 136 ° is the angle between faces on the Berkovich tip.

Sixteen indents were made per sample and all imprint area measurements were reviewed and manually re-measured when necessary, e.g. if surface features influenced the automatic edge detection.

3.13.2 Berkovich indentation

For the majority of the Berkovich indentation results presented herein a multi-cycle displacement controlled loading method was developed. This enabled observation of the extrinsic size effect by testing at a range of indentation depths for a single indent. The multi-cycle method was applied with incrementally increasing maximum loads, and elastic modulus and indentation stress being calculated from each unload curve as described below. A continuous stiffness measurement (CSM) method was additionally used for testing proton-irradiated material.

Depth-controlled method

Indentation with a Berkovich tip was carried in an Agilent G200 instrumented indenter using the manufacturer-supplied software 'Nanosuite'. A schematic of this device can be seen in Figure 3.7. In this instrument, load is applied through the indenter head using an electro-magnetic coil and sample positioning is controlled by a precision positioning table.

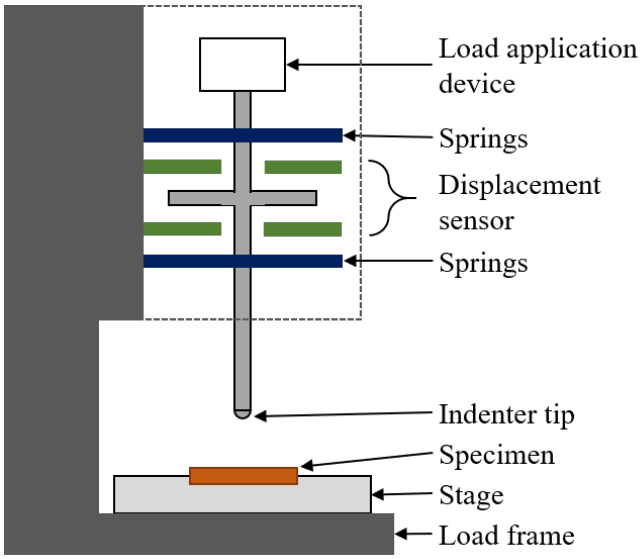

Fig. 3.7 Schematic of G200 nanoindenter, re-drawn from [128].

The multi-cycle method was based on a standard routine within Nanosuite that used theory based on eminent work by Oliver and Pharr [49], which itself uses key contributions from Sneddon [68]. Force applied and tip displacement were recorded throughout the test, which consisted of ten cycles to a maximum indentation depth followed by unloading to 30% of the maximum force for that cycle. For each cycle elastic modulus and hardness can be calculated as follows.

As per the Oliver and Pharr approach, the unload portion of each load-displacement cycle was fitted with a power law of the form

$$F = \alpha(h - h_f)^m \tag{3.4}$$

where F is the force and h the displacement during unloading. α and m are constants, and h_f the residual indent depth, found by fitting using the least squares approach. It is possible to apply this equation to many simple punch geometries by varying the exponent m. Eq. 3.4 was differentiated and solved at peak load and displacement to obtain the gradient of the initial portion of the unloading slope, which is referred to as the stiffness,

$$S = \frac{dF}{dh} \tag{3.5}$$

Contact depth at peak load, h_c, was then calculated using the following adaptation of an expression derived by Sneddon [68],

$$h_c = h_{max} - \varepsilon \frac{F_{max}}{S} \tag{3.6}$$

where h_{max} is per cycle displacement at maximum load, F_{max} is per cycle maximum load, and ε is a constant equal to 0.75 for a Berkovich indenter. This value of h_c is then used to calculate the projected contact area, A_c, which is calculated using the polynomial equation of fit obtained during tip calibration (as described in the below sub-section).

The reduced modulus, which encompasses contributions from both the tip and specimen, was calculated as,

$$E_r = \frac{S\sqrt{\pi}}{2\sqrt{A_c}} \tag{3.7}$$

Finally, the specimen elastic modulus was evaluated at maximum load by solving the following equation,

$$\frac{1}{E_r} = \frac{1 - \upsilon_i^2}{E_i} + \frac{1 - \upsilon_s^2}{E_s} \tag{3.8}$$

where E is the elastic modulus, υ is Poisson's ratio and the subscripts i and s denote the indenter tip and sample respectively. For the diamond Berkovich tip, $\upsilon_i = 0.07$ and $E_i = 1140$ GPa.

Indentation hardness for a Berkovich tip was calculated as the ratio of force to projected area,

$$H = \frac{F_{max}}{A_c} \tag{3.9}$$

To create a set of data for comparing multiple intrinsic length-scales, depth-controlled Berkovich indents to a final depth of 2 μm were made into all samples investigated in this work. A total of 16 indents were made and averaged to get representative properties across different areas. Data for each of the indents was reviewed individually and indents with a high measured thermal drift (>0.06 nm/s) were disregarded, as were any that had a poor initial surface find as this could indicate contact with surface contamination.

An example of good raw load-displacement data produced by a single indent can be seen in Figure 3.8(a). Beside this, in Figure 3.8(b) is an example of data excluded from the final analysis where cycles with an irregular shape and inconsistent loading gradients is indicative of poor initial contact detection and/or surface contamination.

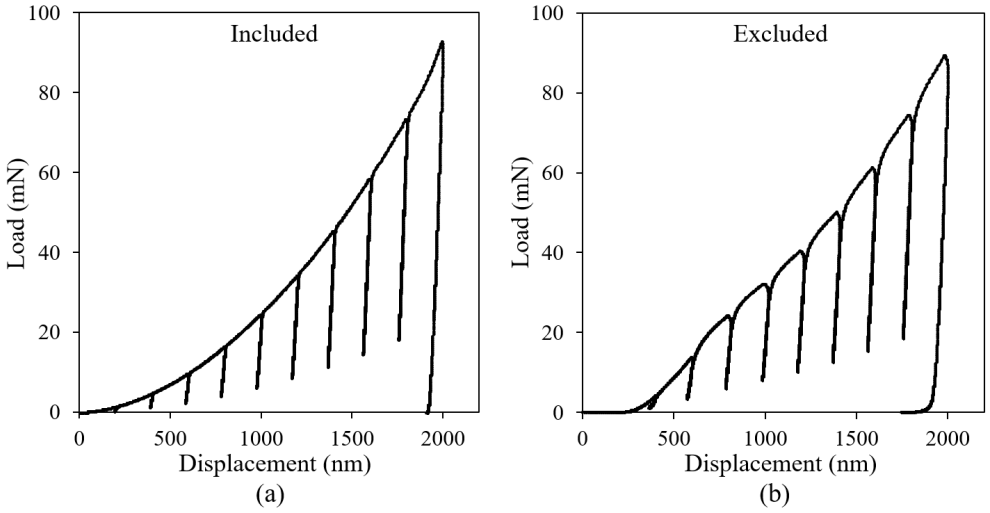

Fig. 3.8 Load-displacement data for two Berkovich indents in AR CuCrZr. An example of included data is shown in (a), whereas (b) is an example of data excluded from the final analysis due to a large degree of 'nosing' indicative of significant indentation creep.

Continuous stiffness measurement

The CSM method is so-called because it is able to provide measurements throughout the depth of the indentation test. During indentation using the CSM method [49] a small dynamic oscillation at high frequency is superimposed with the load applied to the tip. The amplitude of the resulting

displacement is measured using a frequency-specific amplifier, which allows contact stiffness to be continually measured throughout the loading segment of the test as opposed to measuring it from the unload curve, as was described above. As a result the hardness and modulus can also be calculated throughout the entire depth range. In this work a frequency of 45 Hz was used with a harmonic displacement target of 2 nm.

Frame compliance and tip calibration

For an ideal sharp indenter the projected (cross-sectional) contact area A_c, can be geometrically calculated at any indentation depth, h_c, as

$$A = 3\sqrt{3}tan^2\alpha h_c^2 \tag{3.10}$$

where α is the angle between the central axis of the tip (along which the force is applied) and any of the faces. For a Berkovich tip $\alpha = 65.27°$ so the ideal area function can be approximated to

$$A \approx 24.56h_c^2 \tag{3.11}$$

However in reality the tip will never be perfectly sharp, therefore a more complex equation is required to accurately characterise the contact area as a function of contact depth.

Tip calibration and frame stiffness calculations were carried out using the semi-automated calibration tool within Nanosuite. Six indents were made in a fused silica reference sample of known, independently verified elastic modulus (72 GPa) to a depth of ~2500 nm using the CSM method. The contact area is calculated at each point by rearranging Eq. 3.7,

$$A = \frac{\pi}{4}\left(\frac{S}{E_r}\right)^2 \tag{3.12}$$

where E_r is a known value when indenting into a reference sample. This data is then fit using an equation of the form,

$$A(h_c) = m_0h_c^2 + m_1h_c^1 + m_2h_c^{1/2} + m_3h_c^{1/4} + \ldots + m_nh_c^{1/2^{n-1}} \tag{3.13}$$

where h_c and the coefficients $m_{0\to n}$ are the tip geometry coefficients, which are calculated within via fitting to the experimental data. In this work the lead term (m_0) was not fixed and the number of terms was increased to three; the mean squared error was then less than 2 %.

Frame stiffness was calculated at the same time, using data from the same set of indents into fused silica. During an indentation test it is not just the stiffness of the specimen that is sampled but instead a composite stiffness, K^*, that has a contribution from the frame:

$$\frac{1}{K^*} = \frac{1}{S} + \frac{1}{K_f} \tag{3.14}$$

where S is the specimen stiffness, as previously defined, and K_f is the frame stiffness. Eq. 3.7 can be rearranged for S and substituted into the above equation, which gives the following,

$$\frac{1}{K^*} = \frac{\sqrt{\pi}}{2E_r}\frac{1}{\sqrt{A}} + \frac{1}{K_f} \tag{3.15}$$

Here, E_r is a known quantity but the area function term may not be. Therefore A is replaced using Eq. 3.9,

$$\frac{1}{K^*} = \frac{\sqrt{\pi H}}{2E_r}\frac{1}{\sqrt{F}} + \frac{1}{K_f} \tag{3.16}$$

Hence, if indents are made into a material of known elastic modulus and uniform hardness the frame compliance is found to be the y-intercept of a plot of $1/K^*$ versus $F^{-1/2}$.

3.13.3 Spherical indentation

The size effect in spherical indentation is observed as an increase in yield strain with decreasing tip radii [83, 129]. Therefore a range of tips with varying tip radii were used to carry out this work. Also, unlike indentation with a Berkovich tip, the imposed strain changes as a function of indentation depth. A multi-cycle method was used that indented to incrementally increasing depths within a single test, with material properties being calculated for each cycle as described below; this provided elastic modulus and stress as a function of strain.

Multi-cycle Method

As with the Berkovich indentation, testing was carried out using an Agilent G200 nanoindenter (see Figure 3.7). The cyclic load-controlled routine based on Field and Swain's approach

[66, 130] was developed within Nanosuite. A total of 40 cycles were made per indent, with each cycle unloading to 30% of the maximum load; an example of this is show in Figure 3.9.

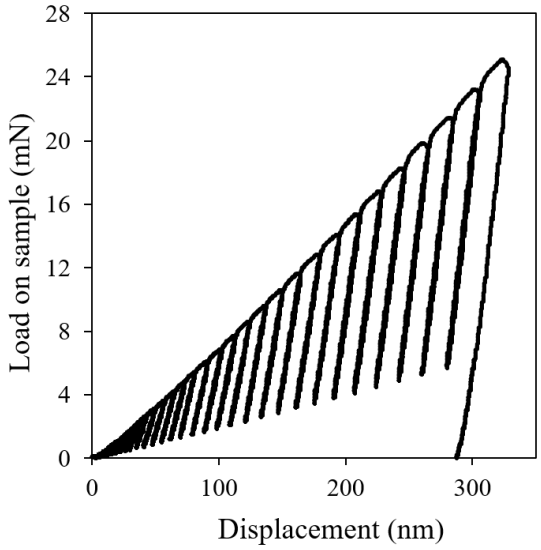

Fig. 3.9 Multi-cycle load displacement response during spherical indentation

The contact mechanics between two bodies was first evaluated by Hertz in the 1880's [67]. Later, Johnson [131] described a special case of this - the displacement of a sphere into a flat surface - as

$$\delta = \left(\frac{9}{16} \frac{F^2}{E^{*2}} \frac{1}{R} \right)^{(1/3)} \tag{3.17}$$

where F is the force acting on the sphere, E_r is the reduced elastic modulus described by Eq. 3.8, and R is the radius of the spherical tip.

When indenting into an elastic-plastic material, after the yield point has been exceeded a residual impression will remain in the surface when the indentation force is removed; this is shown schematically in Figure 3.10. There is a degree of elastic recovery of the material as evidenced by the difference between loading and unloading curves in the force-displacement plots. The amount of elastic recovery, h_e, can be calculated per cycle and is equal to the difference between maximum tip displacement, h_{max}, and residual impression depth, h_r:

$$h_e = h_{max} - h_r \tag{3.18}$$

At maximum displacement, the contact depth, h_c, is assumed to have equal contributions from the elastic (recoverable) and plastic (permanent) components [68]:

$$h_c = \frac{h_{max} + h_r}{2} \tag{3.19}$$

The contact radius, a, can similarly be expressed using geometrical relationships,

$$a^2 = 2Rh_c - h_c^2 \tag{3.20}$$

Hertz's equation (Eq. 3.17) must be re-written to adjust for loading onto a concave surface (the residual impression) as opposed to a flat surface

$$h_e = \left(\frac{9}{16}\right)^{(1/3)} \left(\frac{F^2}{E_r^2}\right)^{(2/3)} \left(\frac{1}{R} - \frac{1}{R'}\right)^{(1/3)} \tag{3.21}$$

where R' is the radius of the residual indent impression, which is included to account for the relative radius of curvature between the tip and concave surface. Since the elastic recovery is in a direction normal to the sample surface the radius of curvature of the residual impression will always be greater than the apparent tip radius. R' can be expressed in terms of the contact radius and residual depth using the geometry of a sphere elastically deforming in half space,

$$R' = \frac{a^2 + h_r^2}{2h_r} \tag{3.22}$$

Eq. 3.21 can be rearranged to take the following form,

$$F^{2/3} = \left(\frac{16}{9}\right)^{(1/3)} \frac{E^{*2/3} R^{1/3}}{\left(1 - \frac{R}{R'}\right)^{1/3}} h_e \tag{3.23}$$

Therefore a plot of $F^{2/3}$ against h_e has a gradient found by calculating the first differential,

$$\frac{dF^{2/3}}{dh_e} = m = \left(\frac{16}{9}\right)^{1/3} \frac{E_r^{2/3} R^{1/3}}{\left(1 - \frac{R}{R'}\right)^{1/3}} \tag{3.24}$$

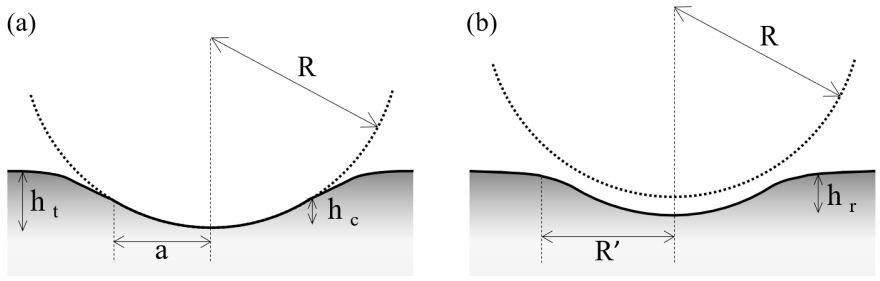

Fig. 3.10 Definition of parameters used in spherical indentation calculations. (a) is the situation of the tip under load and (b) is with the tip retracted from the sample surface.

Traditionally h_r has been calculated per cycle using the load and displacement values at only two points - fully loaded, and fully unloaded [132]. However, the method used for this work included all data points during unloading (an adaptation implemented by Dr J Hickey, Imperial College London). By plotting $F^{2/3}$ against h_e the unload data could be fit with Eq. 3.24 and h_r found by calculating the x-axis intercept. An example of the load-displacement data produced using this method in a plot of $F^{2/3}$ vs. h_e can be seen in Figure 3.11 (a). The fit to unloading data is shown in Figure 3.11 (b), where a fitting range of 95 – 50% F_{max} was employed. The first 5% of unload data was excluded from the fitting because in this region a phenomenon called 'nosing' can occur [133], which is an artefact resulting from creep of the material under load.

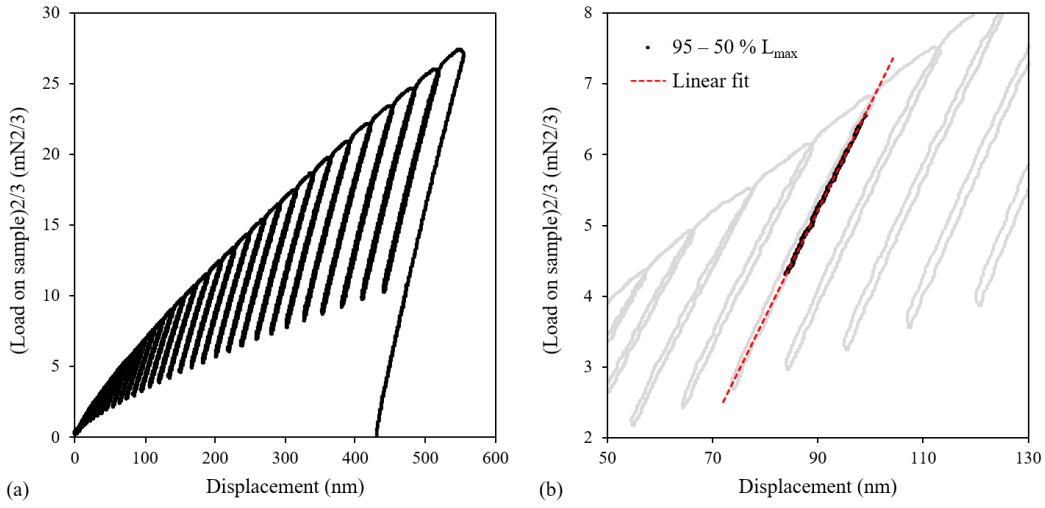

Fig. 3.11 (a) Full $F^{2/3}$ versus displacement data for a single indent, R = 30 μm, in CuCrZr and (b) magnified example of linear fit to one unloading segment

Finally, rearranging Eq. 3.24 enables the calculation of reduced modulus, and thus elastic modulus via Eq. 3.8, on a per-cycle basis,

$$E_r = \sqrt{\frac{9m^3}{16R}\left(1 - \frac{R}{R'}\right)} \tag{3.25}$$

where R' is calculated per-cycle using h_r, based on the tip calibration function (see the following sub-section).

Indentation stress and indentation strain are also calculated on a per-cycle basis using the following equations,

$$\sigma = \frac{F_{max}}{\pi a^2} \tag{3.26}$$

$$\varepsilon = \frac{a}{R} \tag{3.27}$$

It is important to note that all load-displacement data was corrected for thermal drift and load frame compliance post-test. The total displacement, h_t, was adjusted to account for thermal drift as follows,

$$h_t = h_i - \dot{h_t} t \tag{3.28}$$

where h_i is raw displacement, $\dot{h_t}$ is the rate of thermal drift, and t is the test time. Here the thermal drift refers to a single value, measured at the end of the test by holding the tip on the sample at 25% of F_{max} for 75 s, and assumed to be constant throughout the test. Frame compliance and surface find corrections were similarly accounted for in the displacement data, h,

$$h = h_t - FC_i - h_{sf} \tag{3.29}$$

where F is the applied load and C_i is the frame compliance value as calculated during tip calibration, the details of which are provided in the following sub-section. h_{sf} is the surface find correction, which was manually carried out within Nanosuite for all indents. Surface point corrections were made based on the principle that the measured elastic modulus from a spherical indent into a homogeneous material is constant with indentation depth. Surface effects such as pile-up, roughness, or contamination can cause a deviation from this; to account for this, small adjustments were made to the original (automatically-detected) displacement at initial contact until the modulus was constant throughout the test.

Up to 20 indents were made to a final nominal strain of $a/R \approx 0.2$ per tip, per sample. In order to average the data across all the indents a custom Python routine was used, a considerable amount of which was developed by Mr P. Klupś, University of Oxford. Within the code all data was linearly interpolated so that it was discretised to the same values of indentation strain. This initial step was necessary since there will always be minute variations in displacement into the material despite the application of consistent loads, therefore the 40 data points produced by each cycle do not occur at the same values of strain. In this way, single stress-strain and modulus-strain curves were produced per sample for every tip radius.

Frame compliance and tip calibration

As with other types of instrumented indentation, it is important to accurately characterise the contact area between tip and sample by defining an effective radius at every point during the test; this is used in the calculation of indentation stress and elastic modulus and an incorrect measurement can lead to large errors in these calculations. Since diamond is an anisotropic crystal it is difficult to achieve a perfect spherical tip by polishing and the tip radius varies slightly over the surface profile. Therefore calibration of a spherical tip is required and results in a tip radius function that describes the radius as a function of indentation depth.

There are several approaches to spherical tip calibration. Manufacturers often image the finished tip in a scanning electron microscope and fit a circle to the tip shape, which then defines the tip radius. Whilst this is an efficient approach, there are inherent flaws due to user interaction (i.e. deciding to what extent along the tip the circle should be fit) and imaging (i.e. accurate focus, microscope calibration). Also, it does not account for the fact that the radius is not constant over a range of indentation depths. A more precise approach is to image the tip using an atomic force microscope (AFM) [128]. This is much more labour-intensive and requires a good understanding of the AFM technique, however it is able to produce a nanometre-resolution 3D map of the topology that can then be used to calculate the tip radius as a function of indentation depth. Finally, tip calibration can be performed by indenting into several reference samples of known Poisson's ratio and elastic modulus [69, 129]. This was the method employed to calibrate all spherical tips used in this work and was carried out as follows.

Multiple indents (a minimum of three) were made into four calibration materials with known, independently verified elastic moduli and Poisson's ratios: fused silica, glassy carbon, borofloat

glass, and sapphire. The properties for each of these materials are given in Table 3.3. The indents were made using a load-controlled partial unloading method to approximately $a/R = 0.3$ whilst keeping within the elastic deformation regime.

Table 3.3 Elastic moduli and Poisson's ratios for samples used for spherical tip calibration.

Material name	Elastic modulus (GPa)	Poisson's ratio
Fused silica	72	0.17
Glassy carbon	36.5	0.2
Borofloat glass	64	0.2
Sapphire	420	0.2

Equations 3.20 and 3.22 can be substituted into Eq. 3.24 to produce a quadratic of the form,

$$32h_cE_r^2R^2 + (18m^3h_r - 18m^3h_c + 16h_r^2E^{*2})R + 9m^3(h_c^2 - h_r^2) = 0 \tag{3.30}$$

As was previously demonstrated, m and h_r can be deduced by fitting to the unload data and E_r is now also a known value for each of the reference samples. Therefore by solving the above quadratic the apparent tip radius, R, can be plotted as a function of contact depth, h_c. A best fit to this data was then made using a function taking the form of either a linear or polynomial formula. For the 30 μm and 90 μm tips it was found that the calibration data deviated from the ideal tip radii functions at very small penetration depths, therefore the first 120 nm and 50 nm of data, respectively, were fit with separate power law functions to achieved a better fit.

Throughout this work the spherical tips are referred to by their average measured radii. Table 3.4 summarises the tip manufacturer, nominal (as purchased) tip radii, and actual (as calibrated) radii.

Table 3.4 Nominal and measured tip radii, and supplier name.

Nominal tip radius (μm)	Measured tip radius (μm)	Supplier
10	8	Micro star tech.
30	15	Micro star tech.
50	30	Synton-MDP
150	90	Synton-MDP

The frame compliance of the system (i.e. how much flexture there is in the indenter arrangement) can also be established as part of this tip calibration routine. Within an Excel spreadsheet it was varied iteratively until the curves of effective radius functions for all reference samples are coincident.

It is important to note that, as with other indentation methods, pile-up and sink-in is not accounted for in any calculation of contact area. So although thorough tip calibration helps to calculate a more accurate theoretical contact area between tip and sample, the response from different material properties or crystal orientations could not be accounted for in real-time during the test.

3.14 Pillar compression

Pillar compression experiments were carried out at the University of California, Berkeley, (UCB) with the assistance of Mr H. Vo. A Hysitron PI88 indenter equipped with a flat punch tip of radius 15 μm was used within a FEI Quanta 3D FIB/SEM. Pillar measurements were first taken to record individual pillar cross-sections and heights. Samples were then mounted on the indenter stage and the rig installed within the FIB (see Figure 3.12).

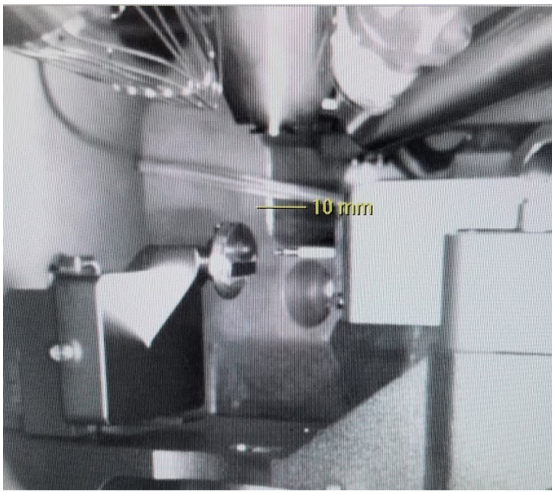

Fig. 3.12 CCD camera view of in-situ indenter mounted inside FIB chamber

The stage and indenter rig were tilted to 4 ° to enable some of the top sample surface to be viewed, which helped with tip alignment as some shadowing could be seen. The tip positioning was checked before every pillar compression and aligned such that the centre of the tip was centralised (or as close to this as possible) with the pillar. All tests were run with a displacement rate of 0.01 nm/s to a total displacement of 20 % of the pillar height, or until the slipped portion made contact with material surrounding the pillar. The Hysitron software recorded load-displacement data as well as live electron-beam imaging throughout the test. In addition to this, images were taken immediately before and after each compression.

Post-processing of the data was required to correct the initial point of contact and convert the load-displacement data into stress-strain curves. This was done in a MatLab code originally produced by Dr C. Hardie [134] for analysis of cantilever data but modified so that it could be applied to pillar data. Firstly, a linear line was fitted to all load-displacement data in the initial linear elastic region (manually identified by mouse-clicking on first and last points) and the entire curve shifted so that this line intersected with the axis origin. Load and displacement were then converted into engineering stress and strain using the standard equations,

$$\varepsilon = \frac{\triangle l}{l} \tag{3.31}$$

$$\sigma = \frac{F}{A} \tag{3.32}$$

where F is the load on the indenter, A is the pillar cross-sectional area, $\triangle l$ is the compression distance, and l is the original pillar height. The stress, strain and displacement-corrected data were then exported into Excel spreadsheets to be able to compare between material conditions.

3.15 Impulse excitation technique

A GrindoSonic ® MK7 instrument was used to obtain a measure of Young's modulus using the Impulse Excitation Technique (IET). This non-destructive technique measures the resonant frequency of a transient vibration produced in a material after it has been stuck with a small sphere at the end of a flexible rod. The equation used to calculate Young's modulus is as follows:

$$E = 0.9465 \frac{m f_f^2}{b} \frac{L^3}{t^3} T_1 \tag{3.33}$$

where m is the mass of the bar, b the width, L the length, and t the thickness. f_f is the fundamental resonant frequency of the bar, as measured using a transducer, and T_1 a correction factor that takes into account the Poisson's ratio of the bar. Two bars were machined from the as-received CuCrZr, each having dimensions of 10 x 20 x 80 mm.

Chapter 4

Material response with no intrinsic length-scale

4.1 Introduction

There have been many studies on the size effect in mechanical properties of material systems due to sample dimensions when testing at the micron and sub-micron scales (e.g. [58, 135, 42, 83]). Within these studies there are a range of theories as to what mechanisms are responsible for this size effect, not all of which can consistently be applied to the various small-scale testing techniques. For example, the presence of strain gradients has been used to justify size effects in nanoindentation [56, 80] but the same cannot be said for micropillar compression tests, where there are no strain gradients [87]. Even comparison between results collected using the same test approach is not straightforward since differences in fabrication techniques (e.g. focused ion beam machining versus additive manufacturing [136]) and initial microstructure have also been found to influence the extrinsic size effect [137].

To isolate and understand size effects purely attributable to extrinsic length-scale - i.e. establish a base-line condition free from the complexities of variables attributed to microstructure - indentation testing was carried out on pure single crystal copper. Both Berkovich indentation and spherical nanoindentation were carried out to observe the result of varying penetration depth and tip radius, respectively. Due to a lack of grain boundaries or alloying elements, single crystal copper was chosen because it has no obvious inherent intrinsic length-scale other than a constant (low) dislocation density. Any change in response during mechanical testing is

therefore predominantly a direct result of the indentation size effect (ISE) and the deformation mechanisms associated to this. There is also a great deal of existing data on single crystal copper that can be included for comparison.

In addition to this, an attempt was made to investigate how the volume of deformed material underneath a spherical indent evolves with increasing indentation strain. When describing the ISE it has traditionally been contact radius that is used to characterise the extrinsic length scale [99, 71]. However, indentation is a tri-axial test and as such it is the response from a 3D volume of material below the tip that determines the mechanical properties. To address this point the size of the deformed region under residual indent impressions as a function of tip radius and indentation strain was explored using electron diffraction techniques in combination with strain mapping software.

4.2 Indentation size effect

The ISE exhibits differently for spherical and Berkovich indentation; in this section, the ISE for both techniques will be demonstrated. For all experiments described in this chapter a single crystal copper (SX Cu) sample was used with surface normal [001]. It was electropolished using Struers D2 electrolyte, as described in Section 3.1, and stored under vacuum when not in use. The exact surface normal was measured by electron back-scatter diffraction (EBSD) after electropolishing and found to have Euler angles of ϕ_1=208.2°, Φ=3.1°, ϕ_2=20.8°, i.e. close to the ideal [001] alignment (see Figure 4.1).

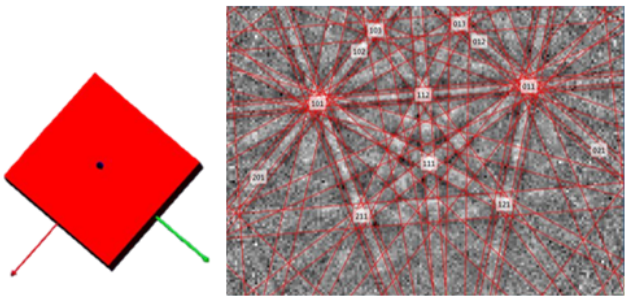

Fig. 4.1 FCC unit cell orientation and corresponding Kikuchi diffraction pattern for the SX Cu sample with surface normal near [100].

4.2.1 Berkovich indentation

Indentations using a Berkovich tip were made using the multi-cycle displacement-controlled method described in Section 3.13.2 with ten cycles. The final displacement was set at 2 μm and a total of 16 individual indents were made. When reviewing the raw data, indents with a high measured thermal drift (>0.06 nm/s) were disregarded, as were any that had a poor initial surface find as this could indicate contact with surface contamination. The elastic modulus and indentation hardness were calculated on a per-cycle basis using the unloading curve, as described using Equations 3.8 and 3.9 in Section 3.13.2. Results for all accepted indents can be seen in Figure 4.2.

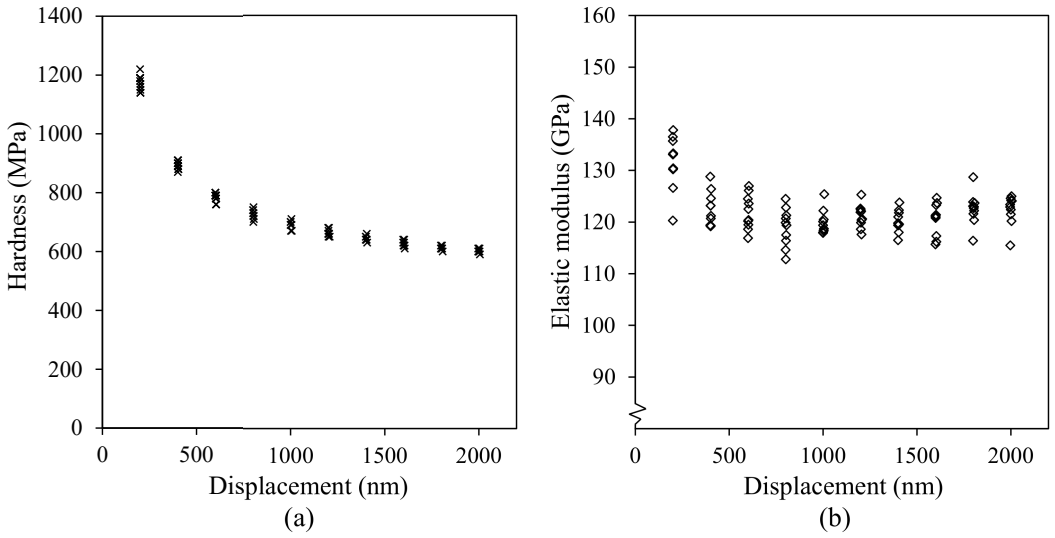

Fig. 4.2 Berkovich (a) hardness and (b) elastic modulus data for multiple indents as a function of indentation depth, in SX Cu.

In order to produce a single curve that represented the averaged data of all included indents, a Python routine was used to interpolate between individual cycles and generate modulus and hardness data on the same displacement abscissa. The displacement ranged from the smallest to largest value common to all indentation data so that no extrapolated data was used, only measured values. The results of this are shown in Figure 4.3.

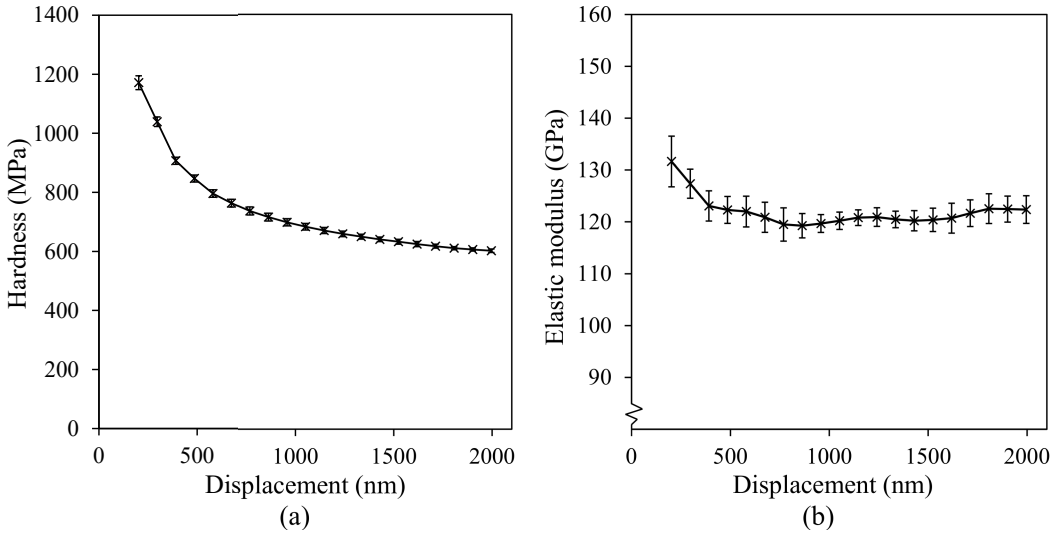

Fig. 4.3 Interpolated Berkovich (a) hardness and (b) elastic modulus as a function of indentation depth for SX Cu.

Pure Cu has an elastic modulus of around 120 GPa but as can be seen in Figure 4.3 there was a small deviation from this value at small indentation depths. The tip calibration was reliable (i.e. gave the expected elastic modulus for fused silica) at depths as little as 30 nm, therefore it is likely that this deviation was due to pile-up. Cu has been shown to be prone to pile-up [138] and this results in an error in the measurement of elastic modulus due to the dependence on contact area in its per-cycle calculation (Eq. 3.7). At small indentation depths pile-up causes the most significant deviation from actual contact area, resulting in the largest error in elastic modulus. In this case it only resulted in an increase of ~10% for the first two data points and therefore does not greatly influence the overall result.

The hardness results and overall trend in ISE shown here compare well with similar experiments on pure Cu. To demonstrate this, data was collected from published work by Lim and Chaudhri [58] and McElhaney *et al.* [57]) and presented alongside the Berkovich data produced in this thesis in the form of a Nix-Gao plot in Figure 4.4. Note that all data sets were area-corrected. At large indentation depths (i.e. low $1/h$) there was a similar hardness response measured in all studies, however there are deviations as the test scale decreases. This is likely due to slight variations in the samples as well as the preparation methods used; Lim used polycrystalline oxygen-free Cu whilst McElhaney used single crystal Cu with a surface normal of (111), and both mechanically polished the specimens as opposed to using electropolishing,

which has been found to exaggerate the indentation size effect [139]. This demonstrates that the intensity of the size effect depends on the condition of the material.

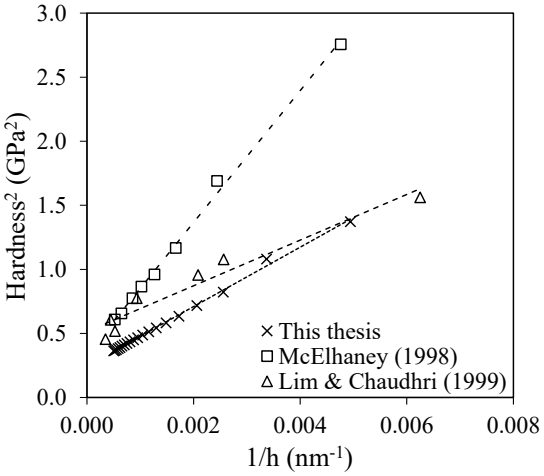

Fig. 4.4 Nix-Gao plot comparing the Berkovich results shown in Figure 4.3 and data produced by Lim and Chaudhri [58] and McElhaney *et al.* [57]. Dashed lines represent linear trendlines for each data set.

4.2.2 Spherical indentation

Unlike indentation with a Berkovich indenter, where the ISE goes with indentation depth, for spherical indentation it is the indenter radius that changes the measured mechanical properties. In addition to this the indentation strain changes with displacement, allowing for the variation from elastic to plastic behaviour to be measured. As was done for the Berkovich indentation experiments, 16 indents were made into the SX Cu using the multi-cycle, load-controlled method described in Section 3.13.3. Spherical tips of (measured) radii 8, 15 and 30 μm were used and to obtain a higher resolution in strain the number of cycles within a test was increased to 40. Sixteen indents were produced by each tip and an example of a load-displacement curve produced by an individual indent is given in Figure 4.5.

Indentation stress and strain were calculated on a per-cycle bases and defined as the force at maximum load divided by contact area, and contact radius divided by tip radius, respectively [130]. The tip shape as a function of indentation depth was obtained for each tip radii via calibration into reference samples of known elastic properties using a procedure fully described in Section 3.13.3.

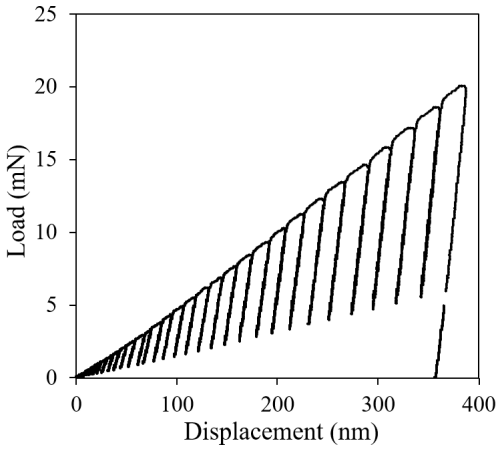

Fig. 4.5 Load-displacement data for a single indent into SX Cu using a 15 μm spherical tip.

Stress-strain curves representing the averaged response from each tip was produced using the interpolation method described in Section 3.13.3. Figure 4.6 shows these curves alongside the associated measured elastic modulus measurements.

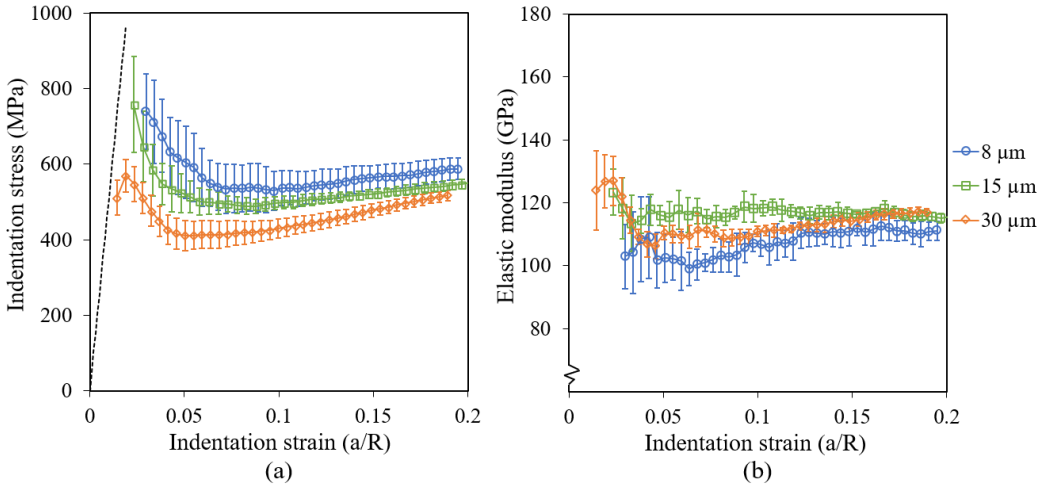

Fig. 4.6 Single crystal Cu (a) indentation stress-strain and (b) elastic modulus for tip radii of 8, 15 and 30 μm.

The ISE is evident and as expected in Figure 4.6 - the smaller the tip radius, the higher the measured indentation stress at constant strain. This is typical of the indentation size effect, for example in metals as shown in [83], as well as other materials such as ceramics, e.g. [84]. Also as expected, and in-line with previous studies, the elastic modulus remains constant across all tip radii. There was slightly more scatter in the results from the 8 μm tip, as evident from the larger error bars, but this is likely as a result of uncertainty in the indentation depth measurement at low loads. There is also a deviation from the expected modulus at small indentation depths

for the 30 μm tip, which is possibly due to surface roughness affecting the material response at small indentation depths. However as for the Berkovich indentation data this only applies to the very initial measurements.

It should be noted that for all tip radii the increase in indentation stress at low indentation strains, seen in Figure 4.6, is an artefact of averaging over data from multiple indents, some of which exhibited pop-in behaviour. A pop-in measures as a sudden increase in displacement at constant load, leading to high calculated values of stress before the pop-in followed by a sudden drop.

4.3 Characterising plastic zone size

Unlike some mechanical testing techniques where the scale of the test is determined by the sample dimensions, e.g. pillar diameter in compression tests or gauge cross-section in tensile samples, the extrinsic length-scale of indentation is less straightforward. In instrumented indentation the unloading curve is fit with an equation to calculate the indent depth and hence contact area on a per-cycle basis. It has traditionally been the contact area, or some factor of this, that is used to describe the scale of an indentation test. In publications by Kalidindi and Pathak (e.g. [1]) they suggest that an "*idealised primary zone of indentation*" beneath an indent has dimensions of $2a$ wide and $2.4a$ deep (where a is contact radius) and the strain is therefore $\varepsilon = h_e/2.4a$, i.e. equivalent to a cylinder of the same dimensions being compressed by the indentation distance h_e.

Imaging of indent cross-sections has previously been done using X-ray tomography [140] and EBSD [141]. These techniques are effective at exploring the 3D variation of strain throughout the sample volume but are not capable of providing the high level of spatial resolution required to look at indents crated by small tip radii. To quantify the deformed region under spherical indentations in this work, electron diffraction techniques - transmission Kikuchi diffraction (TKD) and EBSD - were used in combination with strain mapping software CrossCourt. One sample was additionally viewed using transmission electron microscopy (TEM) to provide more information on the dislocation network produced by indents.

The general shape of the deformation was first confirmed using atomic force microscopy (AFM). AFM can produce surface topography maps with a resolution on the nanometre-scale,

resulting in a 3D profile containing information on indent depth, imprint diameter, and response surrounding material. Because the cantilever tip must be in contact with (or, for tapping mode, slightly above) the sample to map its topography, this technique cannot be used to observe the progression of deformation and only gives information on the final residual indent post-test. Surface profiles of indents in single crystal copper made using the 8 and 30 μm tips to a maximum strain of ε=0.2 can be seen in Figure 4.7.

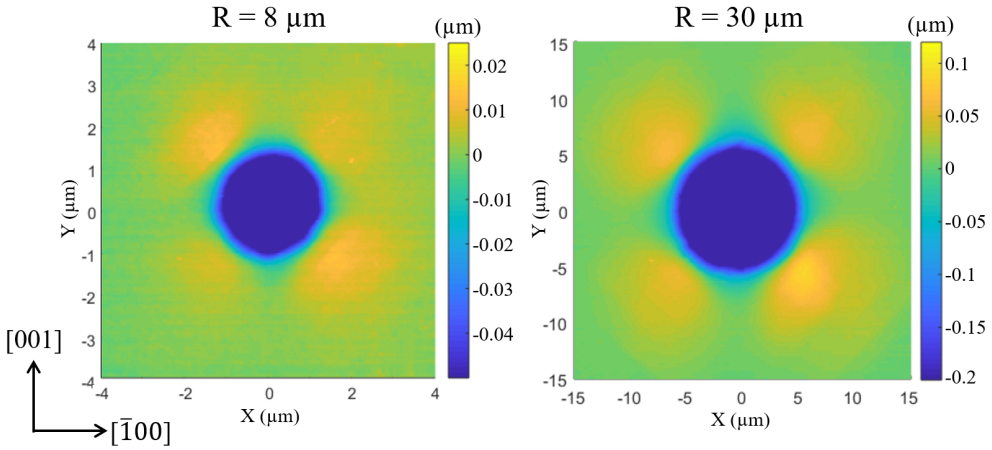

Fig. 4.7 AFM surface profile of indent pits created with the 8 and 30 μm spherical tips.

The AFM maps were produced from raw data using tools within open source software Gwyddion [127], as described in Section 3.12. Pile-up was observed to form in four distinct lobes along the $< 101 >$ directions, corresponding to the known slip systems for FCC metals. The symmetrical nature of the pile-up provided a good indication that both tip and sample were well aligned within the nanoindenter.

4.3.1 TKD and EBSD

In order to view the region containing maximum sub-surface deformation it was determined that cross-sections would be made through the $< \bar{1}01 >$ direction. Two marker indents either side of the pit to be cross-sectioned were used to accurately align the sample orientation horizontally within the FIB. The lift-out location was then determined by eye according to the pile-up lobes, as indicated in Figure 4.8.

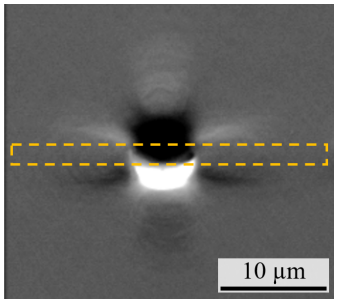

Fig. 4.8 Location of indent cross-section, outlined by yellow dashed lines.

Thin lamellae were produced in the FIB using the method described in Section 3.3.1. These were then attached to copper grids that could be secured in a holder held in the SEM at either 20° or 70° for TKD or EBSD, respectively. Indents made with three spherical tip sizes to three different maximum strains were used in this investigation. Table 4.1 indicates which techniques were used for each condition. The step sizes used are also in Table 4.1 and these define the map resolution. In all cases, the cross-section was taken such that the viewed face had a plane normal of $[\bar{1}0\bar{1}]$, with horizontal and vertical map directions in the $[\bar{1}01]$ and [010] directions respectively.

Table 4.1 Experimental parameters for investigated indent cross-sections.

Tip radius (μm)	**Maximum ε**	**Step size (nm)**	**Method used**
8	0.1	10	TKD
8	0.15	12	TKD
8	0.2	13	TKD + TEM
15	0.1	13	TKD
15	0.2	25	TKD
30	0.1	50	EBSD
30	0.15	50	EBSD
30	0.2	50	EBSD

Data collected by TKD and EBSD were then used to produce infinitesimal rotations and geometrically necessary dislocation (GND) maps using CrossCourt4. The results of this can be seen in Figures 4.9 - 4.11. Note that no deformation could be seen in the 8 μm, $\varepsilon = 0.1$ strain maps but it has been included for completeness.

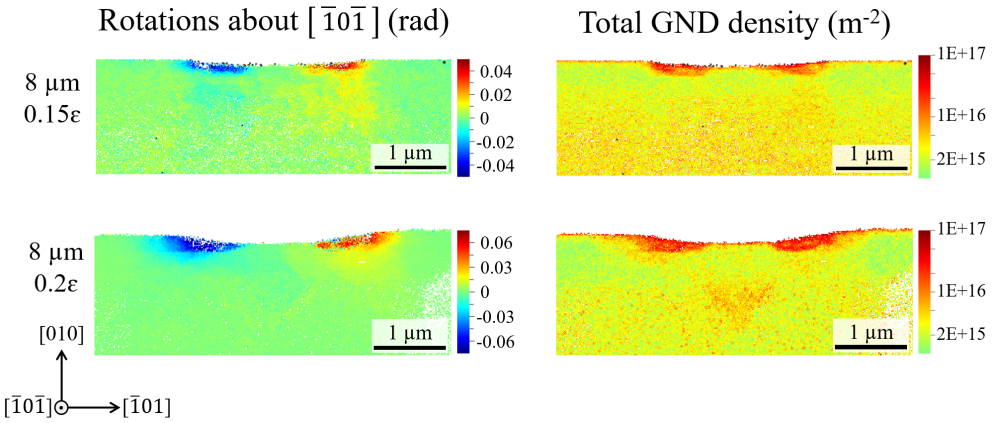

Fig. 4.9 ω12 rotation and GND density maps for the 8 μm tip.

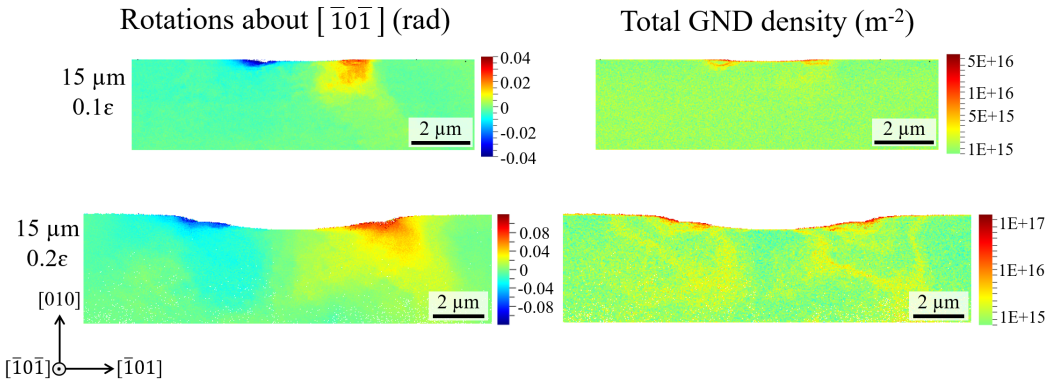

Fig. 4.10 ω12 rotation and GND density maps for the 15 μm tip.

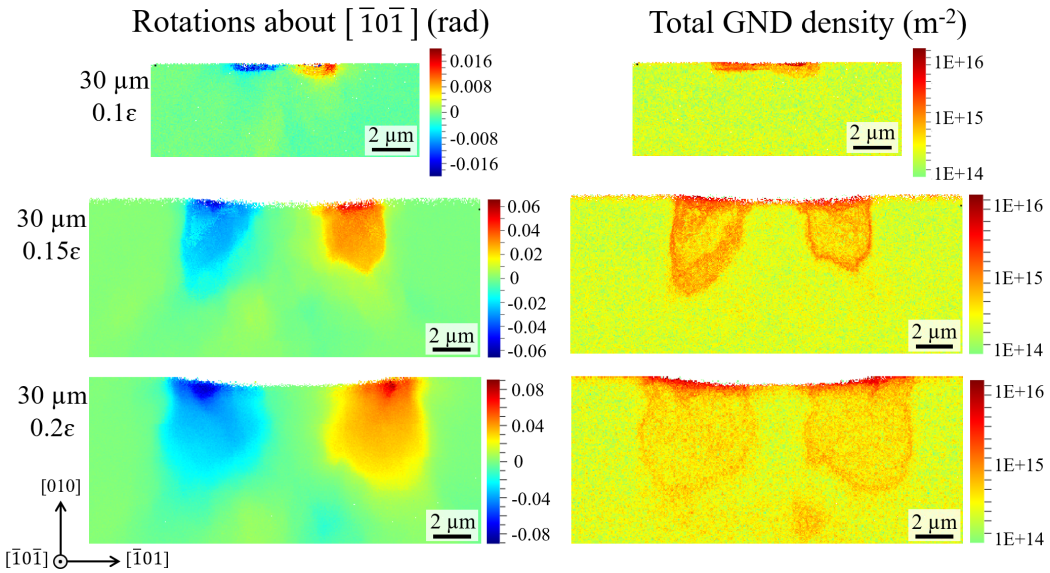

Fig. 4.11 ω12 rotation and GND density maps for the 30 μm tip.

To help visualise the extent and magnitude of plastic deformation, contouring was performed on absolute values from the rotation maps in FIJI using the plugin 'Contour plotter'. Due to the pixelated nature of the data the contour lines were discontinuous, however they still enabled certain regions to be highlighted and provided a visual aid to areas having similar crystal rotation. Contours were coloured according to the percentage above the maximum value contained within the CrossCourt map: yellow $\geq$ 20%, green $\geq$ 40%, blue $\geq$ 60%, and red $\geq$ 80%. The results of this can be seen in Figures 4.12 - 4.14.

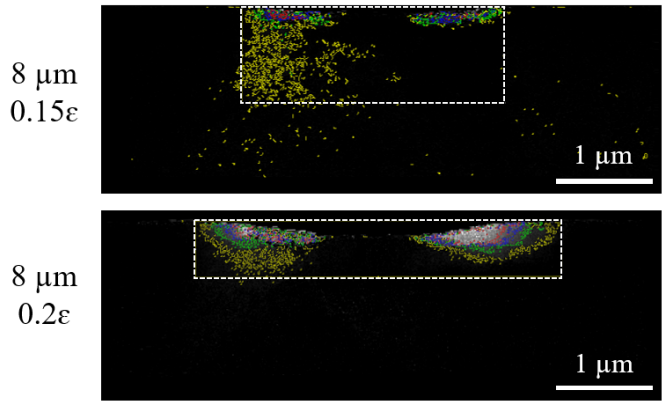

Fig. 4.12 Estimation of plastic indentation zone size under indents made with 8 μm tip radius.

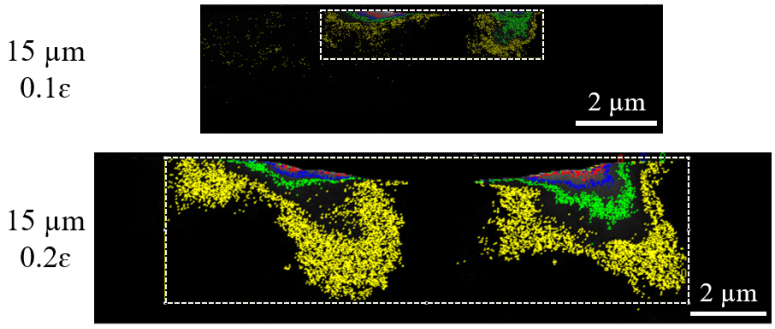

Fig. 4.13 Estimation of plastic indentation zone size under indents made with 15 μm tip radius.

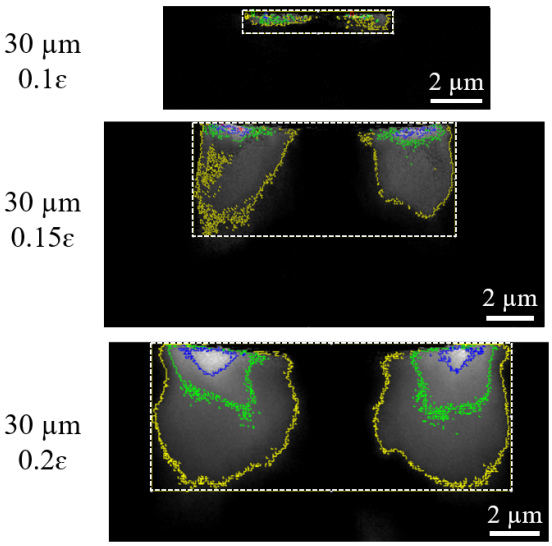

Fig. 4.14 Estimation of plastic indentation zone size under indents made with 30 μm tip radius.

To obtain an estimation of the size of the deformed area beneath an indent, rectangular regions were drawn that were deemed to best encompass dense areas of high measured crystal rotations. This was similar to the approached used by Demir *et al.* [141] for similar experiments. Although there is a significant degree of user interpretation in this method the aim was to qualitatively characterise how indentation zone size evolves as a function of tip radius and indentation strain. The results of this analysis can be seen in Figure 4.15 alongside a curve that represents the idealised primary zone as defined by Kalidindi and Pathak. In both cases the zone sizes are normalised by tip radius squared to compare across all three tip radii.

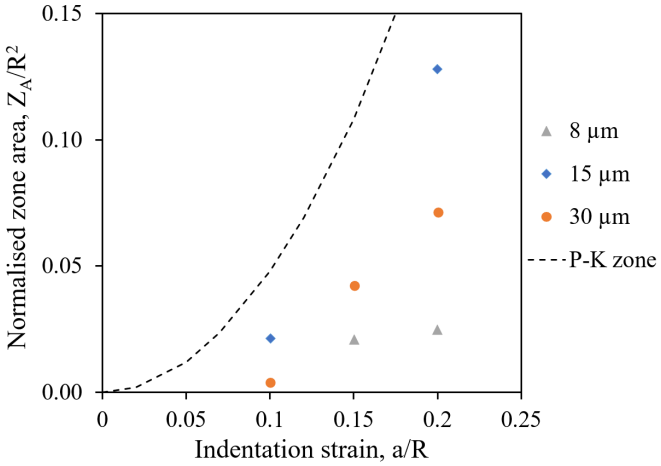

Fig. 4.15 Indentation zone size for three tip radii, R, normalised by R^2. Solid markers represent experimental data and the dashed line is an approximation suggested by Kalidindi and Pathak [1].

No obvious relationship between tip radius, maximum strain, and plastic zone size could be found, however the results shown in Figure 4.15 do suggest that using a value of $2.4a$ is a vast over-estimation of the zone size depth and the indents imaged in this work were never observed to reach this extent. There are a couple of important factors that should be taken into account when considering results obtained from the techniques used here. Firstly, in producing the samples and exposing the indent cross-section there is likely to have been some degree of stress relaxation, potentially loosing dislocations through the free surface(s). Secondly, the results still only represent one slice of the deformed volume. Different results would have to be obtained by cross-sectioning along a different plane but being an FCC material some degree of symmetry can be assumed (as inferred from Figure 4.7).

4.3.2 TEM

One of the indent cross-sections – 8 μm, $\varepsilon = 0.2$ – was additionally observed by STEM. Bright- and dark-field images were taken with the sample tilted so that the beam was aligned with the $[\bar{1}0\bar{1}]$ axis. It is easy to observe dislocations in this mode since bending of the crystal lattice around dislocations results in a change in the diffraction condition and produces a strong contrast change. A bright-field micrograph of the sample is shown in Figure 4.16, with the contrast in negative so that dislocations are highlighted in white.

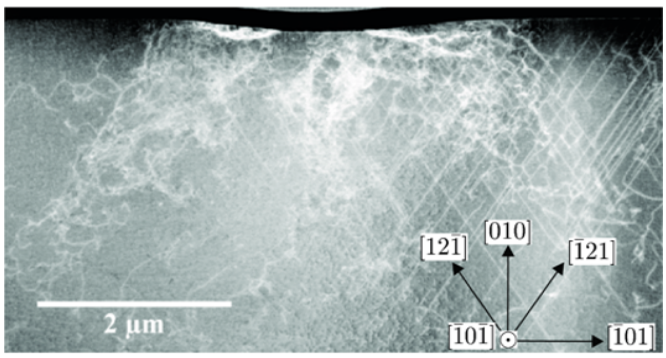

Fig. 4.16 Bright-field STEM micrograph of indent cross-section.

A dense network of dislocations can be seen directly beneath the indent impression; these are generated when the material deforms to accommodate the indenter tip and have a higher concentration when the strain gradient is greatest. These are a mixture of statistically stored dislocations (SSD) and geometrically necessary dislocations (GND). Slip traces (diagonal white lines) can also be seen due to the $[011](\bar{1}\bar{1}1)$ and $[\bar{1}\bar{1}0](\bar{1}\bar{1}1)$ slip systems. The extent of the

deformation, if considered in terms of the extent of dislocations, is much further than inferred from the TKD results. This is thought to be due to the fact that disperse, runaway dislocations do not contribute much to residual deformation. The shape of the deformation is also different from what may be expected, with the two side lobes extending diagonally outwards by approximately double the residual contact radius.

4.4 Discussion

In this chapter the mechanical response of single crystal copper to nanoindentation at various length-scales was explored. For Berkovich indentation the ISE exhibited as a decrease in hardness at larger indentation depths, as expected. It was shown that pile-up can cause an over-calculation of elastic modulus using the unload curve in multi-cycle indentation, since the real contact area deviates from the value generated from the tip area function produced during tip calibration. For the Berkovich data this effect was not significant and only influenced the initial data points. For spherical indentation the ISE was seen as an increasing indentation stress for decreasing tip radii. Again, this was as expected and the measured values compared well with those reported in previous studies (e.g. [98]). The effect of pile-up was less significant in the spherical data and found to cause deviations of only ~10% in the initial data produced at small indentation depths.

The deformed region beneath residual indent impressions was observed for indentations produced by three tip radii at different values of maximum strain. It was found that deformation formed in two distinct lobes beneath the edges of the contact area between tip and sample, comparing well with model predictions [142]. The plastic zone was restricted to the area directly below the indent impression and quickly diminished further into the bulk material. The highest measured crystal rotations and GND densities were contained in a more localised, dense area beneath indents produced by the smallest tip radius (8 μm) compared to the larger two radii, which showed more extensive areas of deformation at the same indentation strain. In a similar study by Demir *et al.* [141] the authors report that GND density decreased for smaller indentation depths, in opposition with strain gradient plasticity theories that are often used to explain the ISE. An alternative explanation of the observed ISE given by the authors is dislocation source limitation due to a reduction in the free dislocation length. As GND density

increases, dislocation line segments are restricted and it becomes more difficult to activate new sources, an effect that is more prominent for smaller indents due to the reduced plastic zone size. This theory is expanded upon and explored further in final discussion.

TEM imaging of one of the 8 μm indents showed that a network of dislocations expanded far beyond the region observed using TKD, however being fairly diffuse they were unlikely to contribute towards any hardening effects. Also, when imaging the 8 μm indent using TKD the step size used approached the limit of resolution for this technique so it is possible that finer details were not observable.

This chapter has focused solely on a single crystal, pure material to make observations on the extrinsic size effect. Clearly, the majority of materials used in real life applications are more complex than this and microstructural features such as grain boundaries and alloying elements heavily influence the response to plastic deformation. The following work will focus on the effect of introducing solutes and precipitates to the microstructure by testing the alloy copper-chromium-zirconium using nanoindentation techniques introduced within this chapter.

Chapter 5

Changing the intrinsic length-scale: precipitate size and spacing

As discussed in the Literature Review, there are many ways in which the intrinsic length-scale can be changed by introducing, or altering the size of, microstructural features. It is well known that changing this length-scale can significantly change the mechanical properties of a material, with decades of research contributing towards the identification of fundamental mechanisms behind methods such as grain size strengthening [10, 11] and solid solution hardening [31]. However, the interaction between microstructure and size of the test when it is on the order of microns is less known and requires further understanding to correctly interpret small-scale results.

In this chapter, the effect of adding fine chromium precipitates of various sizes and spacings to a copper matrix will be explored. Copper-chromium-zirconium (CuCrZr) was chosen for these experiments as it has applications in the fusion industry, where a combination of good thermal conductivity and high strength has led to it being chosen for use as a heat-sink layer in divertor components of Iter [143]. CuCrZr is a precipitation-hardened alloy and previous work has identified that following the initial solution annealing at ~1000 °C, maximum strength can be achieved by applying a heat treatment between 450 - 500 °C [144–146]. This heat treatment results in the optimal size, distribution, and order of nano-scale Cr precipitates that oppose dislocation movement and thus increase the mechanical strength of the material. If the alloy is

aged at temperatures above this the precipitates coarsen and the space between them increases resulting in a reduction in strength, a process known as Ostwald ripening.

For this work a sample set of CuCrZr with varying Cr precipitate microstructures was produced by applying heat treatments at temperatures between 400 and 700 °C. The change in mechanical properties due to such heat treatments was initially verified using Vickers indentation. The microstructure of the CuCrZr samples (before and after heat-treatments) was comprehensively characterised using SEM and TEM techniques; this consisted of grain size, precipitate size, and precipitate spacing measurements. Berkovich indentation to various depths and spherical indentation using a range of indenter tip radii then allowed the observation of interaction between intrinsic and extrinsic length-scale effects. A study such as this, where both microstructure and test scale are systematically varied to form a comprehensive experimental matrix, is not commonly found in the literature. It therefore presents a valuable opportunity to better understand size effects in a rigorous manner.

5.1 Vickers indentation

A plate of Cu-1.0 Cr-0.06 Zr (wt%) was divided into 130 x 90 x 35 mm blocks to produce a total of seven samples; six were annealed in a vacuum furnace for two hours at temperatures of 400, 480, 550, 600, 650 and 700 °C, and one remained in the as-received (AR) solution-annealed state. Note that the naming convention used throughout will be 'CuCrZr-*annealing temperature*'. Small sections from each of these were then mechanically polished (as described in Section 3.2) and Vickers indentation performed in order to confirm that a change in hardness had occurred as a result of the heat-treatments. Sixteen indents were made into each sample type in order to average over any location-specific effects. A force of 100 gf was applied with a hold time of 15 s. The mean hardness was calculated as the force applied divided by the area of the residual imprint, as described in Section 3.13.1, and the results of this are given in Figure 5.1.

Typical precipitation-hardening behaviour was observed with the maximum increase in hardness achieved after annealing at 480 °C, as expected from previous studies and discussed in Section 2.2. Following annealing at higher temperatures, the material softened and returned to approximately the same hardness as the AR state. Quantification of the microstructural changes causing this behaviour will be shown in the following sections.

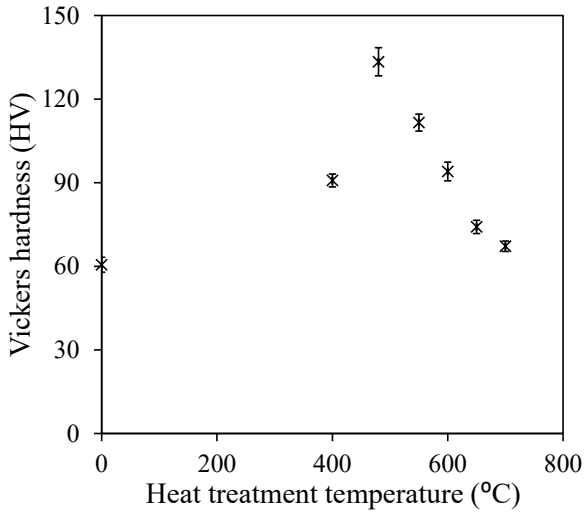

Fig. 5.1 Vickers hardness of as-received and heat-treated CuCrZr sample set.

5.2 Sample characterisation

In order to identify the dominant length-scale responsible for the large change in hardness shown above, the microstructure of all samples was thoroughly characterised. This consisted of the measurement of grain size, precipitate size, and precipitate spacing.

5.2.1 Grain size measurement

To measure grain size for the AR and heat-treated CuCrZr sample set, electron back-scatter diffraction (EBSD) was performed using a scanning electron microscope (SEM); a full description of this technique was given in Section 3.8. The beam voltage used was 20 kV and a beam intensity of 17 (equivalent to a probe current of around 1 nA) was found to produce the clearest Kikuchi patterns for indexing. The acquisition settings for EBSD mapping was as follows: Binning = 4x4, gain = 5, Hough resolution = 70, no. of bands detected = 12, acquisition time $\approx$ 25 ms (automatically set), and 100 frames were collected for the background noise removal.

Three maps were acquired for all samples, each covering different areas across the surface, in order to increase the number of grains counted. A complete set of all EBSD maps acquired for CuCrZr grain size analysis can be found in Appendix A. An example of one inverse pole figure (IPF), showing crystal orientation in the surface normal direction, for the AR condition can be seen in Figure 5.2.

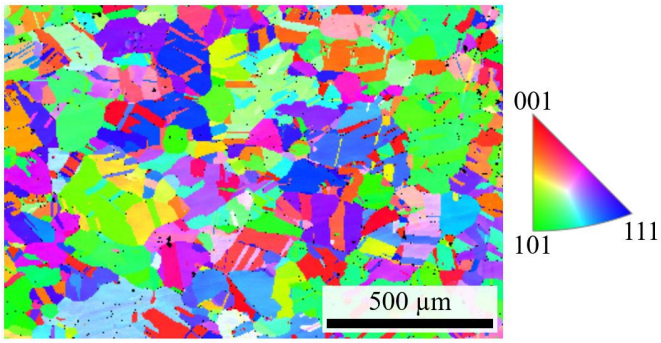

Fig. 5.2 IPF map for CuCrZr-AR and key to orientation with respect to grain colouring.

Grain size analysis was carried out within the Channel5 post-processing software 'Tango' using the IPFs of crystal orientation in the surface normal direction. Firstly, noise reduction was carried out; wild spikes were removed and non-indexed points were interpolated using the six nearest neighbours. If there were not six neighbouring indexed points then the pixel remained non-indexed. The largest percentage of non-indexed points was 7.2 % for the as-received condition. After noise reduction this number was reduced to 1.4 % - well within the ASTM standard (E2627) advised limit to data cleaning, which specifies that no more than 10% of points should be modified [147].

Automatic grain detection was performed using the elliptical fit approach, where identified grains were fit with an ellipse in order to define the x- and y-diameters. The orientation relationship between adjacent grains was also measured. It has been shown that Σ3 twin boundaries - representing a misorientation of 60° between neighbouring grains - contribute little to mechanical strength (outside of the nano-grain regime) [148, 119], therefore these were disregarded in the grain size analysis. Any grains containing fewer than 10 pixels were then removed from the analysis, as advised by the aforementioned ASTM standard. Grains detected on the border of the IPF maps were also disregarded since their size could not be accurately determined.

The final results of grain size measurement for all samples can be seen in Table 5.1.

Table 5.1 Grain size of as-received CuCrZr and following heat treatments, with Σ3 twin boundaries disregarded.

Sample ID	No. grains	Grain diameter (μm)		
		Mean	Min.	Max.
CuCrZr-AR	155	77.9	14.3	527
CuCrZr-400	280	77.3	14.3	311
CuCrZr-480	152	73.6	14.3	409
CuCrZr-550	316	79.6	14.3	396
CuCrZr-600	190	68.7	14.3	359
CuCrZr-650	385	74.1	14.3	365
CuCrZr-700	188	72.8	14.3	331

It was found that there was no significant grain growth across the samples, ruling out the possibility that any change in hardness was due to differences in average grain size. At least 150 grains were counted for all samples, despite removing border grains and those containing <10 pixels, which gives confidence that the final results are statistically reliable. The minimum and maximum grain diameters across all maps are also provided. In this case the smallest grain diameters are the same for all samples since the step size was kept constant and a value of 14.3 μm is therefore the diameter of a grain containing 10 pixels (i.e. lower threshold to be included for analysis). Several sizeable grains were observed for each sample, however the average grain sizes are sufficiently large compared to the extrinsic length-scale of nanoindentation that tests would be considered as being single crystal so indenting into an anomalously huge grain would not affect the results.

5.2.2 Precipitate size characterisation

Following electropolishing (Section 3.2) streaks of larger particles in the material matrix of all samples could be seen in the SEM. Energy dispersive X-ray spectroscopy (EDS) identified that these were Cr-rich particles - an example of one map acquired on as-received CuCrZr is shown in Figure 5.3. Since the as-received material was solution annealed at 970 °C, and at this temperature the solubility limit of Cr in Cu is only ~0.37% [149], the majority of the Cr cannot be accommodated as solutes within the Cu matrix. The observed Cr particles were on the order of several microns in length and would therefore not contribute towards any precipitation hardening effects. Additionally, since the areas containing them were also visible in the optical microscope these regions could be avoided when positioning arrays of indents.

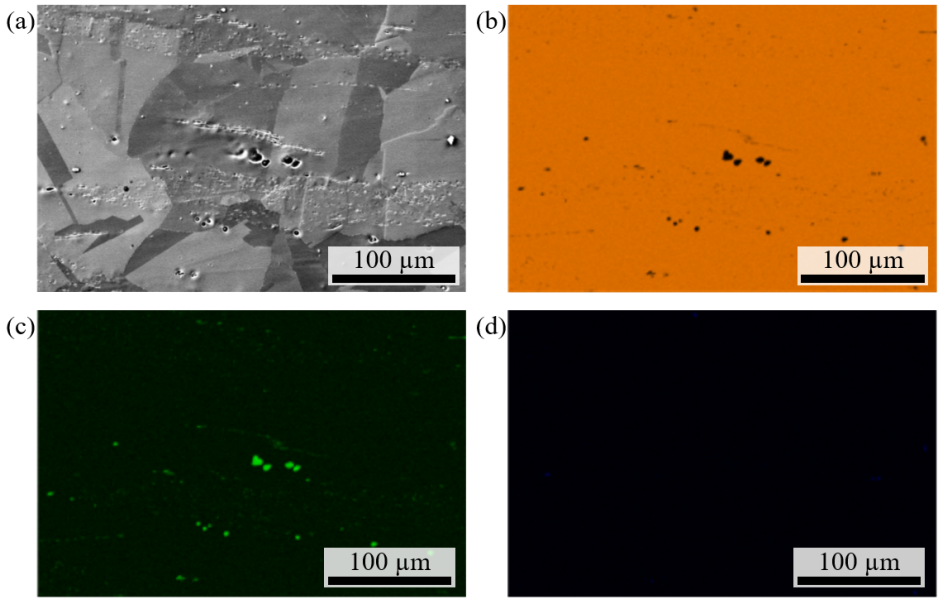

Fig. 5.3 Chemical maps produced in the SEM using EDS: (a) electron image of the scanned area and normalised wt% elemental maps for (b) Cu, (c) Cr, and (d) Zr.

To characterise the smaller, nano-scale Cr precipitates the higher-resolution capabilities of transmission electron microscopy (TEM) was required. This was carried out at the University of Manchester, with Dr J. Lim operating the microscopes and advising on best practice. Samples in the form of 3 mm discs were produced with a twin-jet electropolisher using a electrolyte mix of 1:4 nitric acid to methanol as described in Section 3.3.2. A 200 kV FEI Talos scanning-TEM (STEM) was used with a SuperX-EDS detector from Oxford Instruments. Net Cr chemical maps were used for particle size analysis; maps for all samples are shown in Figure 5.4.

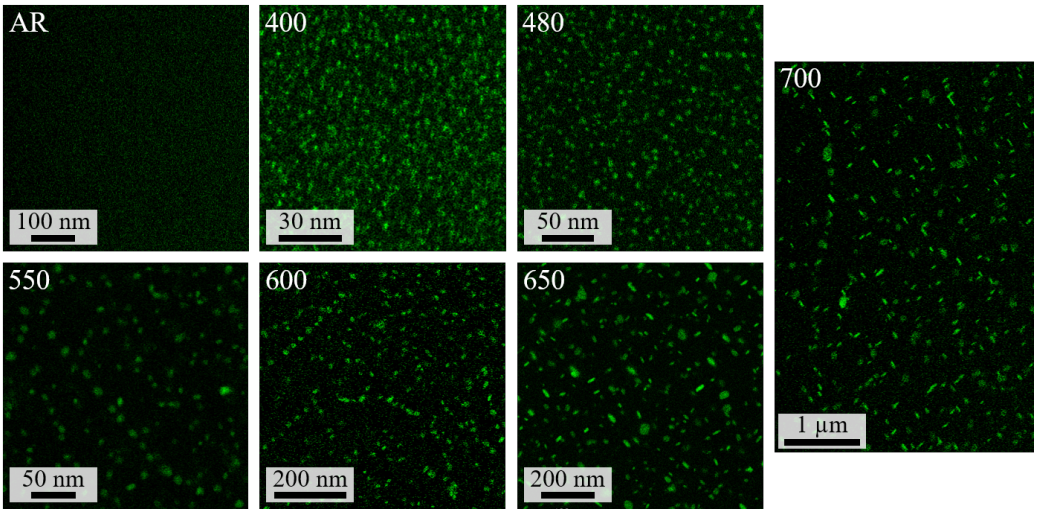

Fig. 5.4 EDS maps showing Cr content (green), labelled by heat-treatment temperature.

As described in Section 3.11.1, these Cr maps were opened within FIJI [114] and the 'Analyse particles' tool was used to detect and measure the precipitates. When carrying out thresholding to remove background noise, the accompanying STEM micrographs were used to make a judgement on the correct level, i.e. the aim was to remove as much stray signal as possible without eliminating visible precipitates. Similarly, the smallest Cr precipitate visible in both the micrographs and the chemical maps was measured and used as the minimum particle diameter for detection. The number and size of particles detected in all samples is given in Table 5.2. Note that the errors shown represent one standard deviation.

Table 5.2 Cr precipitate size as measured using EDS Cr maps.

Sample ID	**No. of precipitates counted**	**Precipitate diameter (nm)**
CuCrZr-AR	Cr in Solution	
CuCrZr-400	426	1.6 ($\pm$ 0.5)
CuCrZr-480	486	3.2 ($\pm$ 1.6)
CuCrZr-550	158	7.0 ($\pm$ 2.0)
CuCrZr-600	256	12.0 ($\pm$ 3.8)
CuCrZr-650	262	16.0 ($\pm$ 7.0)
CuCrZr-700	302	33.2 ($\pm$ 13.5)

In the as-received sample it was not possible to distinguish any defined segregation of Cr (besides the large Cr particles previously discussed). This was as expected since the material was acquired in the solution-annealed and quenched state, where Cr atoms are locked within the Cu matrix (up to the soluble limit). Heterogeneous distributions of Cr could be seen in the CuCrZr-400 material but the first discrete precipitates were observed in the CuCrZr-480 material. As shown in Figure 5.5, in the CuCrZr-550 sample some semi-coherent precipitates were identified by the strain contrast surrounding them, which appeared as two lobes resembling a coffee-bean. This was not seen in the samples annealed at higher temperatures.

It was possible to accurately measure particle dimensions due to the high spatial resolution of EDS in the STEM. However, since the sample thickness could not be measured it was not possible to extract information on the particle density. This was instead done using a different technique described in the following section.

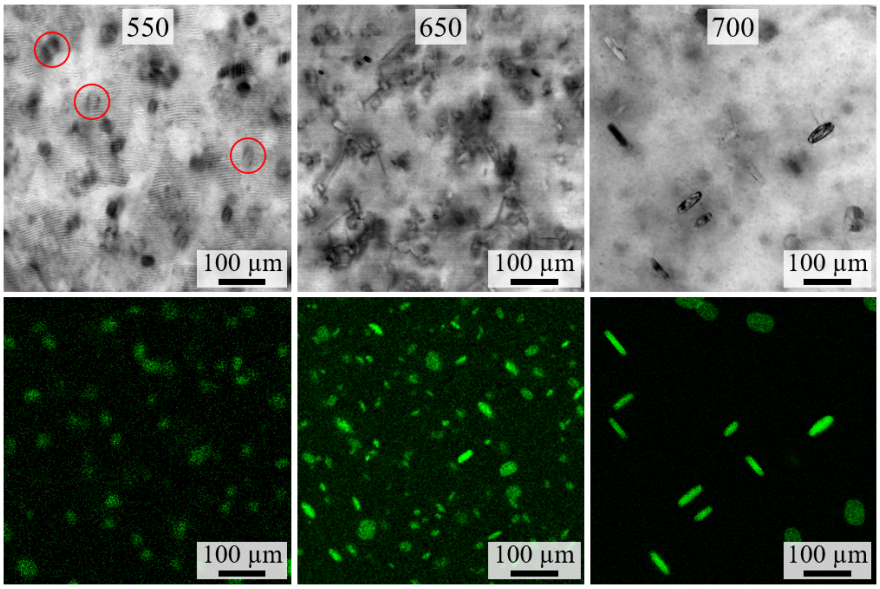

Fig. 5.5 Bright-field micrographs (top row) and net Cr maps (bottom row) for three of the heat-treated CuCrZr samples. Semi-coherent precipitates are outlined in red for the CuCrZr-550 material.

5.2.3 Precipitate spacing characterisation

To measure the average spacing between precipitates, a FEI Titan STEM was used to perform Electron Energy Loss Spectroscopy (EELS). Like EDS, this technique is used to identify chemical composition but in addition to this it can be used to measure the thickness of a sample, which meant that the average distance between precipitates could also be calculated. The materials were prepared using the FIB lift-out technique (Section 3.3.1) in order to produce samples with parallel sides and therefore consistent thickness.

Areas were scanned with the electron beam to produce maps where each point contained the energy spectrum of inelastically scattered electrons collected - the full description of this process is provided in Section 3.11.2. The spectra contained characteristic peaks that were used to identifying the elements present. An example of a spectrum collected from a precipitate can be seen in Figure 5.6.

The raw data was handled within Digital Micrograph, where stray X-rays were removed and spectra were calibrated such that the zero loss peak was aligned with zero energy. The thickness at each map position was then calculated using Eq. 3.1, allowing the total scanned volume to also be calculated for each sample.

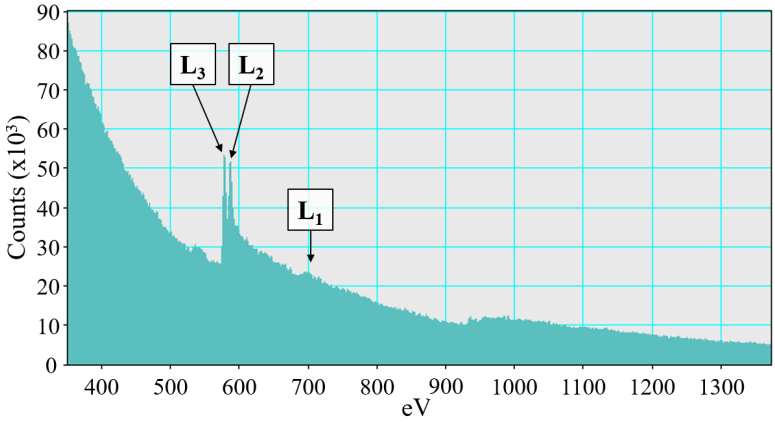

Fig. 5.6 Single EELS spectrum taken from the region of a precipitate. The major (L_2, L_3) and minor (L_1) edge energies for Cr are indicated.

A custom Python routine based on methodology described in [123] was used to produce Cr elemental maps as. Full details of this approach can be found in Section 3.11.2. An example of a high-loss EELS spectrum map (covering an energy range of 670 - 900 eV) can be seen in Figure 5.7(a) alongside the corresponding Cr signal intensity map produced by the Python routine in Figure 5.7(b). Note that in the latter of these the grey-scale represents percentage of Cr, with the highest Cr content being represented in white.

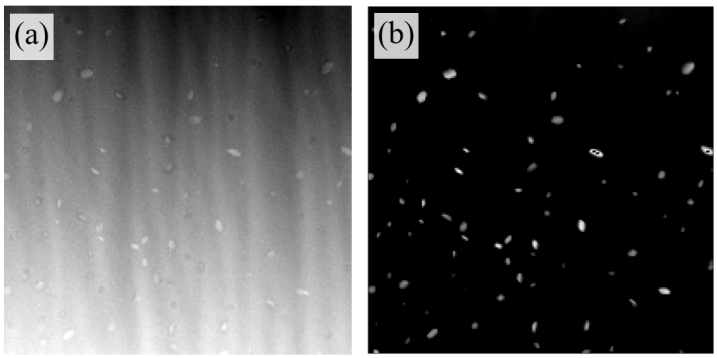

Fig. 5.7 EELS Cr mapping - (a) the original high-loss energy spectrum map for the range 670 - 900 eV and (b) Cr elemental map produced within Python.

The Cr maps produced by Python were used to measured precipitate spacing using a similar approach to that of the characterisation of precipitate size described above. The 'Analyse particles' plugin within FIJI was again used to identify particles based on the Cr elemental maps. An example of the binary map produced after thresholding is shown in Figure 5.8(a) and in Figure 5.8(b) the original EELS high-loss energy map has been overlaid with white outlines of the particles detected. There are several potential precipitates that appear to have not been

detected, as indicated by red circles. This is likely due to a lower Cr signal intensity, either because the precipitate contained less Cr or because it was located further through the thickness of the sample and therefore the edge peak was obscured by background noise.

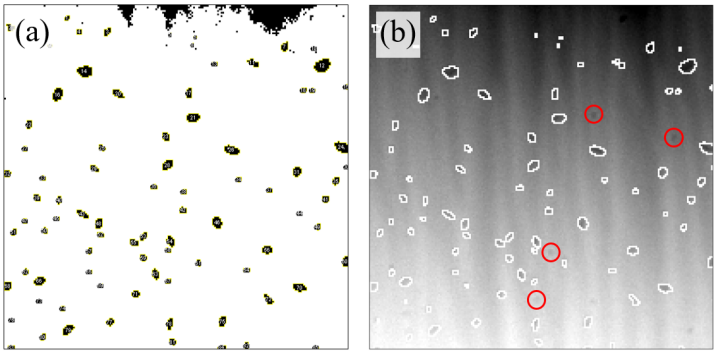

Fig. 5.8 Cr particle detection within FIJI - (a) binary map after thresholding to remove noise and (b) the original EELS high-loss energy map detected particles outlined in white. Red circles indicate potential missed precipitates.

The number and average spacing between particles in each of the samples is given in Table 5.3. Note that here spacing is defined as the average distance between edges of precipitates, not the distance between centre of mass, using the precipitate size measurements made using EDS. A large number of precipitates were counted for each sample, therefore the impact of some not being identified is minimal.

Table 5.3 Cr precipitate spacing as measured using EELS.

Sample ID	**No. of precipitates counted**	**Precipitate spacing (nm)**
CuCrZr-AR	Cr in Solution	
CuCrZr-400	Precipitates not identified	
CuCrZr-480	351	13.3
CuCrZr-550	313	20.7
CuCrZr-600	222	37.9
CuCrZr-650	365	60.0
CuCrZr-700	107	104.4

The quantification of precipitate characteristics shown above supports the reasoning that the observed change in hardness by Vickers indentation was due to a change in the predominant plasticity mechanism, namely from the pinning of dislocations, to shearing/cutting through precipitates, and finally dislocation bowing [150, 24]. Annealing the material at 400 °C allows Cr atoms in the Cu matrix to form small precipitates, resulting in initial hardening due to dislocation pinning by the stress fields around coherent Cr clusters. At 480 °C these precipitates

grow and large stresses are required to shear through them; there is also a sufficiently dense distribution to make it difficult for dislocations to bow around them and progress using the Orowan mechanism [151]. However, as the precipitates continue to grow at higher annealing temperatures the number density decreases. Dislocations no longer need to cut through the precipitates since the large distance between particles is sufficient for dislocation lines to easily bow around them.

5.3 Indentation size effect

5.3.1 Berkovich indentation

Multi-cycle indentation with a Berkovich tip was performed on all CuCrZr samples so that the interaction between precipitate length-scales and indentation size effect (ISE) could be observed. Since the Berkovich tip has self-similar geometry, indentation strain is constant and the ISE scales with indentation depth . Samples were electropolished to create a flat surface free from deformation induced by the previous mechanical polishing stages. The indenter tip shape function and frame compliance were calibrated via indentation into fused silica before indenting into the samples (method given in Section 3.13.2).

A total of 16 indents were made into each sample, all to a maximum depth of 2 μm using ten load partial-unload cycles. As was done for the pure Cu data, indents were reviewed individually to determine the reliability of the data and excluded if the drift measurement exceeded 0.06 nm/s.

The elastic modulus and hardness data for all indents included in the final analysis for the as-received material is shown in Figure 5.9. There was minimal scatter (within $\pm$10%) in the hardness and elastic modulus data across different indents, which gives confidence in the repeatability of the data.

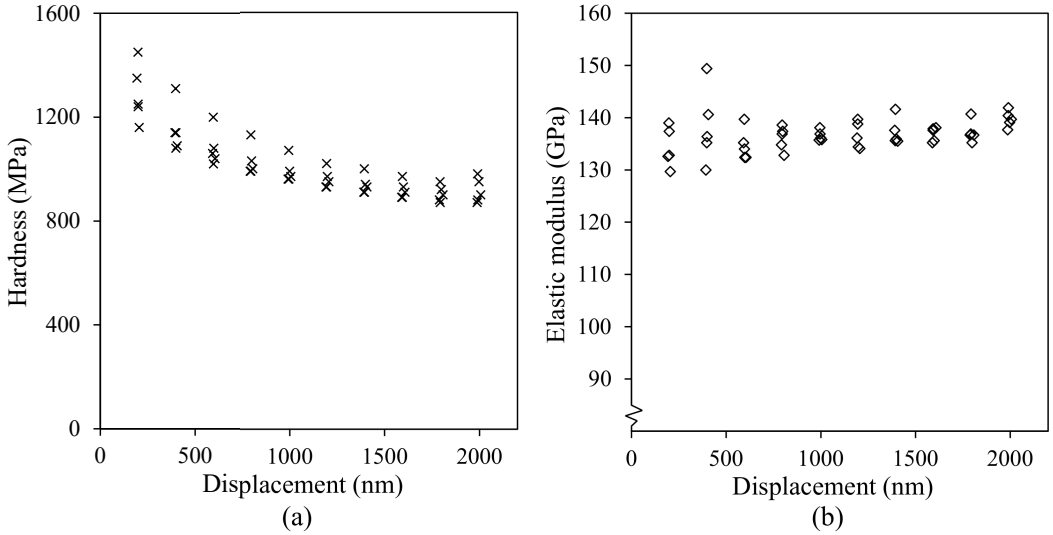

Fig. 5.9 Data for all indents in as-received CuCrZr used for final analysis; (a) hardness and (b) elastic modulus as a function of displacement into surface.

As for the SX Cu sample in Section 4.2, data from individual indents were averaged within a Python routine to produce single sets of hardness and elastic modulus measurements for each of the seven CuCrZr samples. The results of this are shown in Figure 5.10. Note that the y-axis on the plot of elastic modulus displays a reduced range in order to clearly distinguish between individual curves.

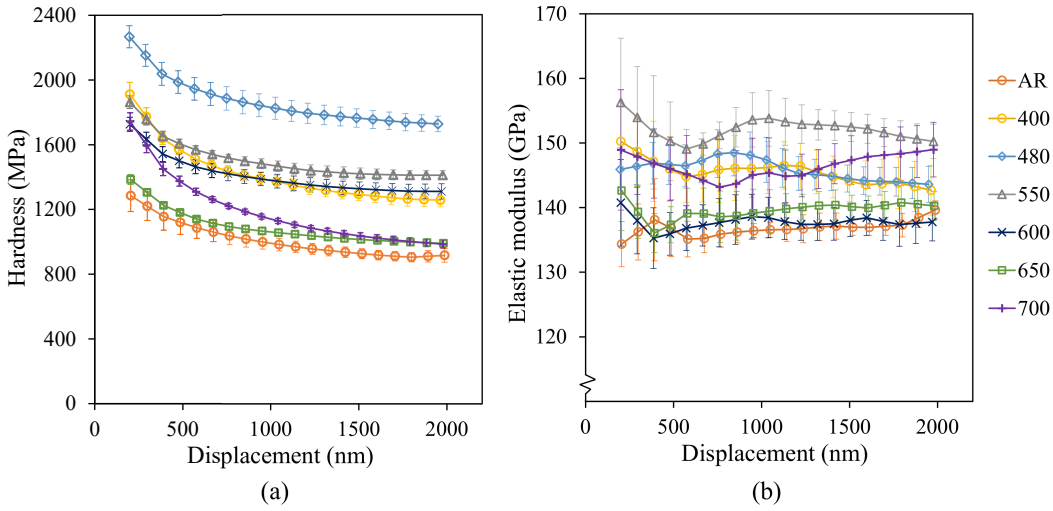

Fig. 5.10 (a) Indentation hardness and (b) elastic modulus for all CuCrZr samples as measured using Berkovich indentation.

The elastic moduli values measured using Berkovich indentation were significantly higher than expected for this material. Upon observation with the SEM it was found that there was a large degree of pile-up visible around the residual indentation pit - an example of this can be seen in Figure 5.11. Since the contact area was underestimated the sample modulus was calculated erroneously high due to an increase in the measured reduced modulus. This leads to the hardness also being over-estimated due to the inverse dependence on contact area.

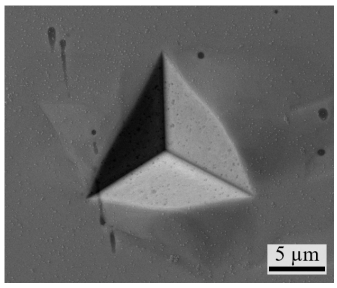

Fig. 5.11 Pile-up around a Berkovich indent in peak aged CuCrZr.

To account for the effects of pile-up, a contact area correction was made by measuring the exact modulus of the CuCrZr used in this work and back-calculating contact area from the measured reduced modulus. Dynamic Young's modulus was measured using the impulse excitation technique (Section 3.15). Four measurements were made in flexture mode on two bars of the AR material having dimensions of 10 x 20 x 80 mm. ASTM standard E1876 - 15 [152] was followed and the instrument was calibrated using the supplied calibration sample prior to testing. The measured fundamental resonant frequencies and calculated modulus for each test are given in Table 5.4.

Table 5.4 Impulse excitation results - fundamental resonant frequencies and dynamic Young's modulus - for AR CuCrZr.

Test ID	**Frequency 1 (kHz)**	**Frequency 2 (kHz)**	**Young's modulus (GPa)**
Bar1 (1)	5.828	14.797	129.99
Bar1 (2)	5.829	5.772	130.05
Bar1 (3)	5.828	-	129.99
Bar1 (4)	5.828	21.611	129.99
Bar2 (1)	5.838	0.403	129.79
Bar2 (2)	5.837	0.391	129.76
Bar2 (3)	5.837	-	129.77
Bar2 (4)	5.837	0.342	129.77

The reduced modulus measured from the indentation tests could subsequently be calculated using the following equation,

$$\frac{1}{E_r} = \frac{1-\upsilon_i^2}{E_i} + \frac{1-\upsilon_s^2}{E_s} \tag{5.1}$$

where the average of the measured sample moduli values was E_s = 130 GPa, sample Poisson's ratio was taken to be υ_s = 0.32 [153], and values for the diamond indenter tip were provided by the manufacturer as $\upsilon_i = 0.07$ and $E_i = 1140$ GPa. The contact area was then calculated for each indentation cycle by rearranging Eq. 3.7,

$$A_c = \frac{\pi}{4}\left(\frac{S}{E_r}\right)^2 \tag{5.2}$$

Finally, the indentation hardness was re-calculated using this corrected value of contact area, also for each indentation cycle. Corrected data for all samples is shown in Figure 5.12.

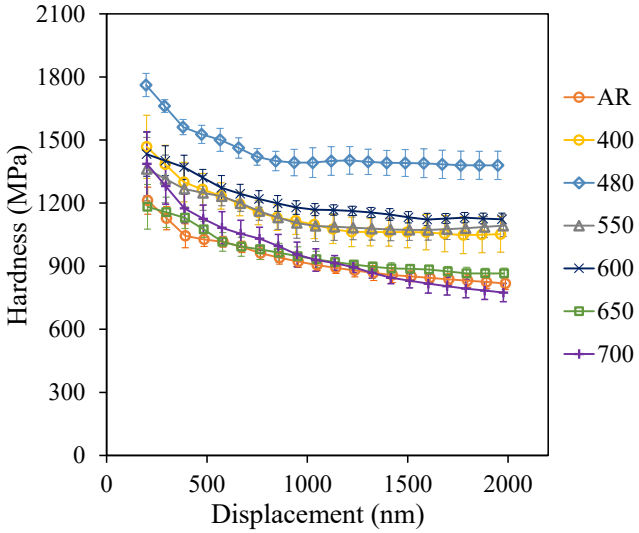

Fig. 5.12 Area-corrected Berkovich hardness data for all CuCrZr samples.

The overall trends in this new data set do not vary significantly from the original data shown in Figure 5.10, however there is a drop in hardness across all samples. The indentation size effect - a decrease in hardness as indentation displacement increases - is evident in all samples, although it quickly diminishes and is less evident at depths greater than 1 μm (on average decreasing by approximately 23% over the first 1 μm compared to 6% in the displacement range 1 to 2 μm). The size effect due to intrinsic length-scale is also observable and corresponds well with initial Vickers hardness results. Data for a subsection of the CuCrZr sample set is shown alongside the single crystal Cu results in Figure 5.13 to highlight the effects of the dominant

strengthening methods: solution annealing, in the CuCrZr-AR material; precipitation hardening, in the peak-aged CuCrZr-480 sample; and over-ageing, in the CuCrZr-650 material.

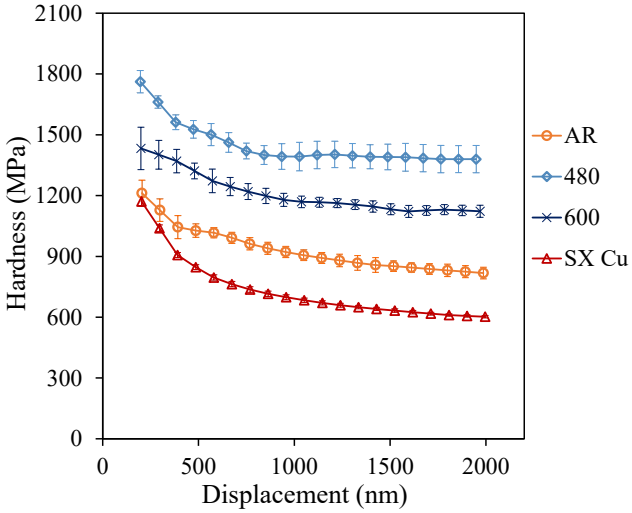

Fig. 5.13 Berkovich hardness data for three CuCrZr samples compared to pure single crystal (SX) Cu.

There are two key points that can be taken from Figure 5.13; firstly, at the initiation of plasticity the response from pure Cu is almost indistinguishable from as-received CuCrZr. The two precipitation-hardened alloys, however, are significantly harder from the first point of contact. This suggests that the response from difference hardening mechanisms has a dependence on the length-scale of the test being used, and that some microstructural differences may only become evident at greater indentation depths. Secondly, the indentation size effect has a much greater influence on the pure copper than the CuCrZr materials. The hardness measured at a displacement of 2 μm is roughly half that measured at the start of the test for copper, whereas the hardness of the CuCrZr samples drops by only one third over the same range. This demonstrates that the extent over which the extrinsic size effect acts depends on the material microstructure.

5.3.2 Spherical indentation

To measure the response from CuCrZr over a range of indentation strain, and to observe the spherical ISE, spherical indentation was carried out using four tips of radii 8, 15, 30 and 90 μm. For this experiment, up to 20 indents were made into electropolished samples using the multi-cycle, load-controlled method with 40 load partial-unload cycles. Results were averaged for multiple indents using the Python code described in Section 3.13.3 to obtain a single curve

representing data produced for one material and one indenter tip. An example of the indentation stress and elastic moduli data for the CuCrZr-AR sample can be seen in Figure 5.14.

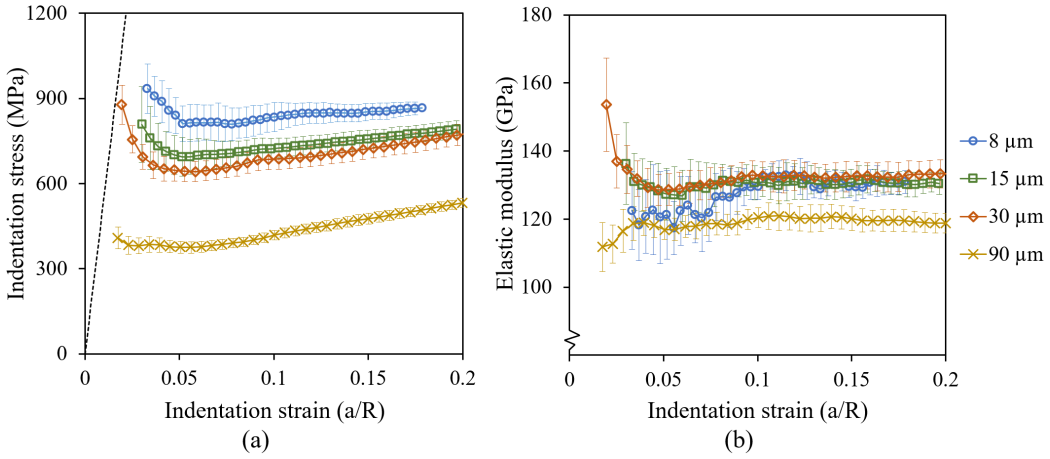

Fig. 5.14 Spherical (a) stress-strain and (b) elastic modulus data for CuCrZr-AR, tested using spherical indenters of four different radii. The dashed line in (a) represents the expected Hertzian elastic response from a material with E = 130 GPa.

The ISE is immediately obvious in Figure 5.14(a), with the smallest tip (8 μm) consistently measuring the highest indentation stress and the largest tip (90 μm) measuring the lowest. Relatively small error bars for all curves indicates that there was little scatter across each indentation array, suggesting that a good surface polish was achieved and that results from individual indents were consistent. The error bars are slightly larger in initial data for the 8 μm tip, which is likely due to a larger variation in measured displacements for shallow indentation depths. For example, at $\varepsilon = 0.1$ the contact depth for the 8 μm tip was just 40 ($\pm$2) nm. The elastic moduli data (Figure 5.14(b)) is consistent for three of the four tips, with the exception of some erroneously high points for initial data produced by the 30 μm tip but given this represents indentation depths on the order of 10's nm this scatter is reasonable. Data for the 90 μm tip, however, is consistently lower than the expected modulus for this material. This could be attributed to several things: poor sample mounting, incorrect mounting of the tip, or an incorrect tip shape function. Since the other data for this material appears reliable, poor sample mounting can be ruled out.

The above process was carried out for all samples and all spherical tip radii. Results for the as-received and heat-treated CuCrZr, grouped by the tip radius used during testing, are shown in the following Figures 5.15 - 5.18. Results grouped by sample can be found in Appendix B.

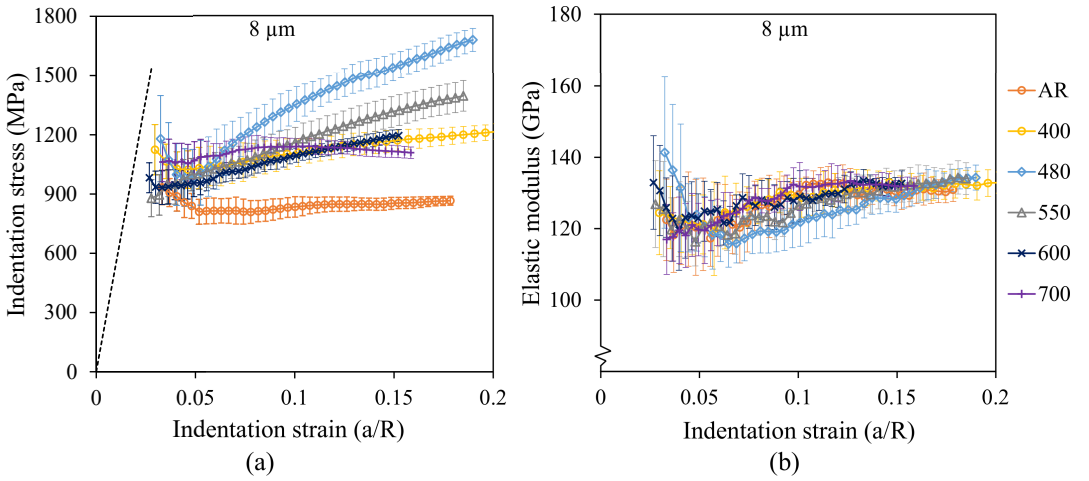

Fig. 5.15 Spherical (a) stress-strain and (b) elastic modulus data for 8 μm spherical tip, all samples.

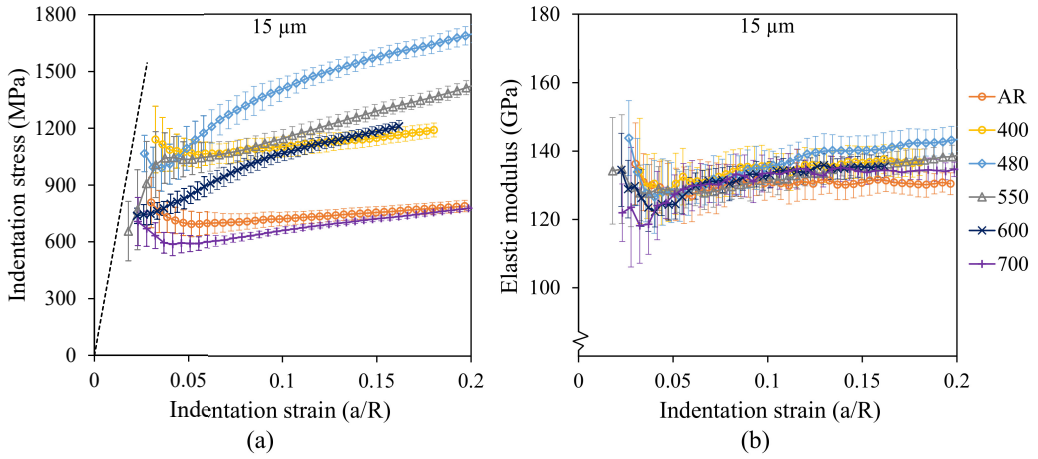

Fig. 5.16 Spherical (a) stress-strain and (b) elastic modulus data for 15 μm spherical tip, all samples.

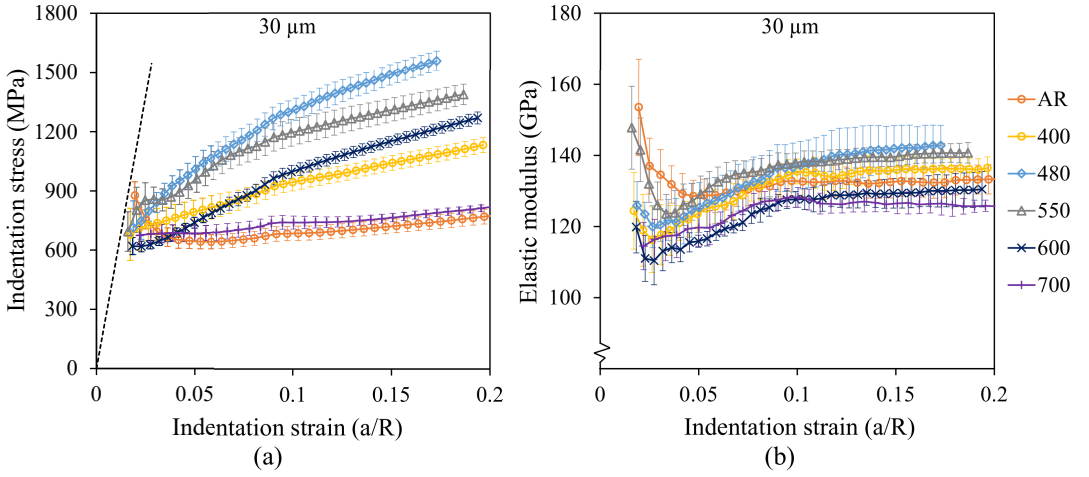

Fig. 5.17 Spherical (a) stress-strain and (b) elastic modulus data for 30 μm spherical tip, all samples.

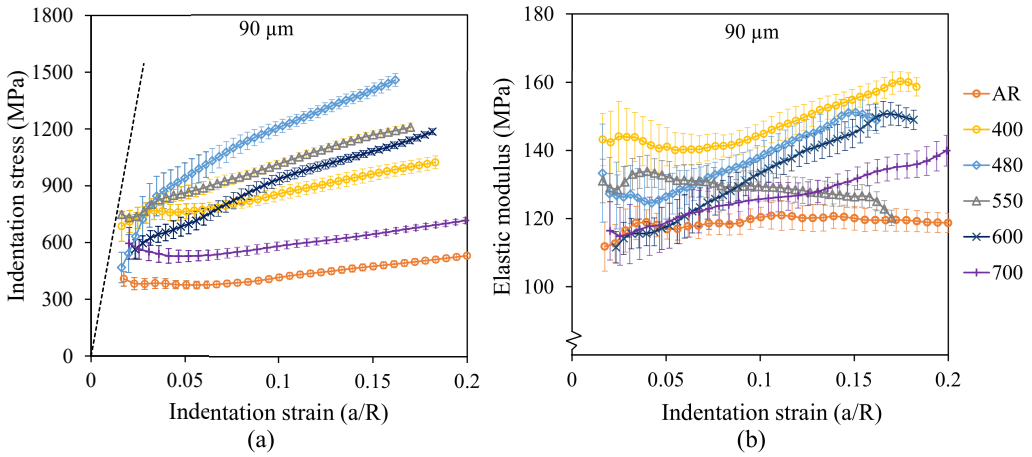

Fig. 5.18 Spherical (a) stress-strain and (b) elastic modulus data for 90 μm spherical tip, all samples.

Data for the CuCrZr-650 sample, which can be seen in Appendix B, was found to be unreliable for all tip radii. The elastic modulus measurements had a significant degree of scatter and the indentation stress values were much lower than any of the other samples in the set. It has therefore not been included in the above plots. Upon observation with an optical microscope this was likely due to poor surface preparation as polishing damage from the mechanical stages were visible but it was unfortunately not possible to repeat the electropolishing process to correct this.

For the other CuCrZr samples the elastic modulus values were generally consistent with the exception of initial data at low strain, however as discussed previously this is reasonable due to the extremely small indentation depths in that range. Greater variation in the measurement of modulus was observed for the 90 μm tip compared to the other tip radii - the range in average modulus across all samples was 29 GPa for the 90 μm tip, compared to 3, 6, and 12 GPa for the 8, 15 and 30 μm tips, respectively. This is likely due to a slight deviation from ideal contact area established during tip calibration; surface and tip roughness will affect the true area in contact during testing and this effect is accentuated for larger tips.

To assess the overall trends in the data for all tips and data, values of average indentation stress were selected at low ($\varepsilon = 0.05$) and high ($\varepsilon = 0.15$) indentation strains and are shown in Figure 5.19. In both cases the ISE is observed as a decrease in indentation stress with an increase in tip radius, as expected. As for the intrinsic size effect, at low strain there is a similar response from all samples as can be seen in Figure 5.19 (a). This suggests that at the initiation of plasticity there is little influence from the precipitate microstructure. As the plasticity progresses,

however, the size effect due to precipitate size and spacing becomes evident - this is evident from Figure 5.19 (b) as a spread in data from different samples.

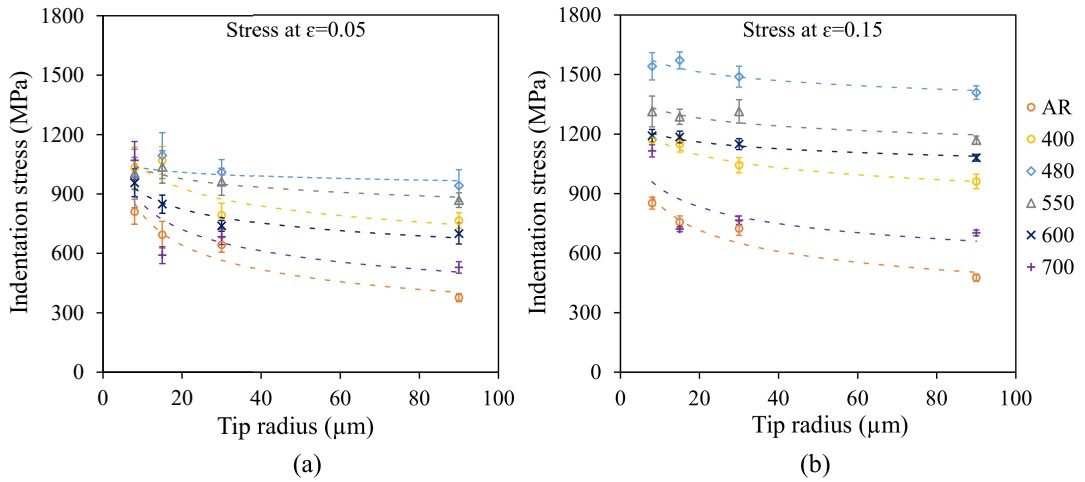

Fig. 5.19 Indentation stress at an indentation strain of (a) $\varepsilon = 0.05$ and (b) $\varepsilon = 0.15$ for all samples and indenter tip radii. Dashed lines are power-law fits to the data to guide the eye.

5.4 Discussion

In this section it has been shown that the precipitation microstructure in CuCrZr can be altered via heat-treating at different temperatures, resulting in a significant variation in hardness as measured by Vickers indentation. Although the grain size did not appreciably change after annealing, the Cr precipitate size and spacing was greatly affected; this was quantified using analytical STEM techniques, which identified that peak hardness was achieved when the precipitates were 3.2 nm in diameter and had an average spacing of 13.3 nm. These values correspond well with similar material characterised in other work [113].

Berkovich indentation was performed and a size effect in hardness as a function of indentation depth was observed for all samples, although the magnitude of this (i.e. amount by which the hardness decreased over the displacement range of 2 μm) varied between samples. There was little difference between the measured hardness of pure Cu and solid solution strengthened CuCrZr at small indentation depths but the precipitation-hardened material was significantly harder throughout the test. The indentation size effect was also observed with spherical indentation, whereby a decrease in tip radius caused an increase in measured indentation stress and this was true even for low strains at the initiation of plasticity. For constant tip radius, there was little

difference in the measured response across all CuCrZr samples. However at increased strains this quickly changed and there was significant hardening seen in the precipitation-hardened material. There was little difference in the overall shape of the stress-strain curves for different samples apart from a small degree of strain-hardening in the peak-aged and over-aged conditions.

As was discussed in Chapter 2, the addition of small precipitates is just one strengthening mechanism used in metals. Grain size strengthening is also commonly used in industry; it is important to understand how the intrinsic length-scale associated to grain boundary density alters the measurement of mechanical strength in combination with the extrinsic size effect. The following chapter therefore consists of an investigation into two of the CuCrZr samples, CuCrZr-AR and CuCrZr-550, that have been modified to have varying grain size.

Chapter 6

Changing the intrinsic length-scale: grain size

Another strengthening mechanism that can be applied to polycrystals is grain refinement, whereby reducing the average grain size results in increased hardness and yield strength. Smaller grains means that there is a higher grain boundary density and it is generally thought that strengthening is therefore as a result of an increase in obstacles to dislocation glide. In addition to this, dislocation curvature will be restricted within small grains and hence dislocation emission via Frank-Read sources becomes more difficult.

Grain refinement can be achieved either as part of the manufacturing process or through techniques applied post-production. For example, physical vapour deposition [154] and electrodeposition [155] techniques can produce a fine-grained microstructure and varying certain parameters can achieve highly controllable and reproducible results. However, this method can only be used to produce coatings or thin layers on the order of micrometers. Post-processing techniques for grain refinement includes severe plastic deformation, whereby large strains are imposed on the material resulting in the creation of small grains. For this work, a severe plastic deformation induced by high pressure torsion (HPT) [117] was used to reduce the grain size of two of the CuCrZr samples. In this technique, two anvils apply pressure to a disc of material whilst one slowly rotates. This induces large stresses within the material that force nano-grains to be created. Details of the technique are given in Section 3.6.

The CuCrZr-AR and CuCrZr-550 samples were used for this study, representing the solid solution and precipitation-hardened alloys respectively. Subsequent annealing in a tube furnace at temperatures of 200 and 600 °C was then performed in order to grow the grains to two different sizes. This generated a total of six new samples - the nano-grained state produced by HPT and two annealed HPT samples for both the CuCrZr-AR and CuCrZr-550 samples. These will hereafter be referred to as 'HPT-*AR/550*' and 'HPT-*AR/550-annealing temperature*', respectively. Indentation testing was carried out using multi-cycle methods with the Berkovich and spherical tips. The results of this were then compared with the original CuCrZr samples.

6.1 Grain size characterisation

Discs of CuCrZr-AR and CuCrZr-550 were subjected to HPT as described in Section 3.6, with a constant pressure of 4 GPa applied for ten turns at a speed of $\frac{1}{15}$ rpm . Slices approximately 2 mm thick were produced from each disc using a slow saw, as indicated in Figure 6.1. These slices were then halved in order to maximise the number of samples available from the limited volume of material. Two samples from each CuCrZr type were annealed at temperatures of 200 and 600 °C for 10 minutes using a tube furnace operated by Dr K. Scott, School of Physics and Astronomy, QMUL. Details of this are given in Section 3.7.

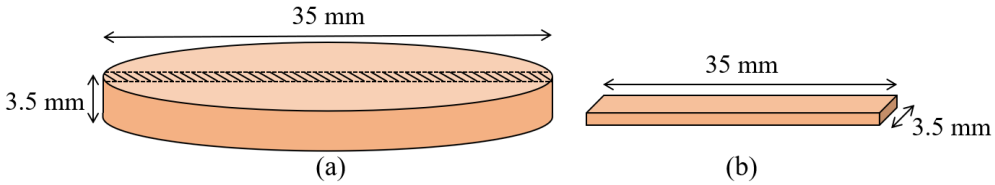

Fig. 6.1 Schematic (not to scale) indicating (a) how slices were produced from discs of HPT material by cutting along the dashed lines and (b) the rectangular samples this generated.

All HPT and HPT annealed samples were prepared by mechanically grinding with SiC paper down to a final grade of P4000, followed by polishing with diamond suspension and chemo-mechanical polishing using colloidal silica. They were then mounted on standard pin stubs using Crystalbond®. An electron back-scatter diffraction (EBSD) map was acquired for each of the samples; previously (for the large-grained CuCrZr samples) three maps were required to observe a statistically reliable number of grains, however this was not necessary for the nano-grained case. Care was taken to avoid thermal drift by mounting the samples in the

SEM then leaving them to stabilise for several hours before carrying out EBSD. Maps were also excluded and repeated if a large amount of drift was evident from the post-acquisition electron image. The inverse pole figures (IPF), showing grain orientation in the surface normal direction, were used for grain size analyses are shown in Figures 6.2 and 6.3.

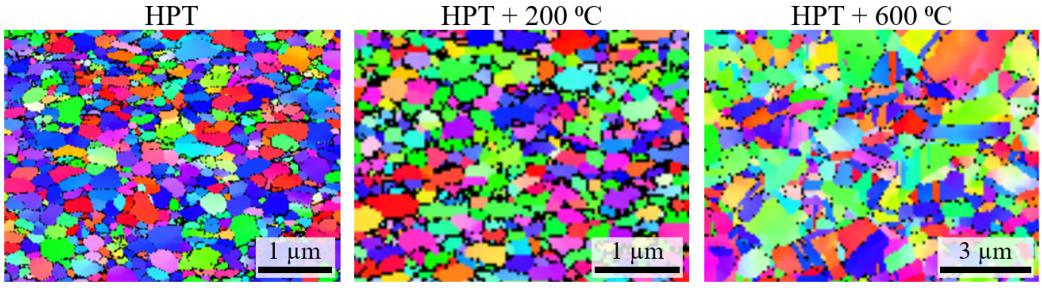

Fig. 6.2 IPFs in the surface normal direction for the HPT-AR material before and after annealing.

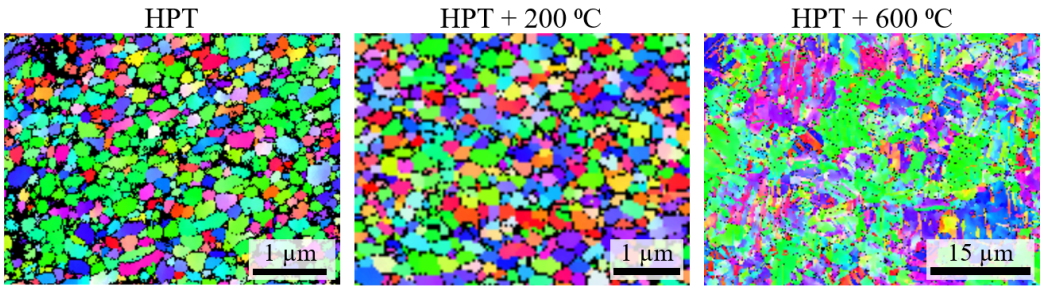

Fig. 6.3 IPFs in the surface normal direction for the HPT-550 material before and after annealing.

As described in the previous Chapter, grains were identified and measured using the elliptical fit method in the Channel5 software 'Tango'. Again, Σ3 coherent twin boundaries were not included, neither were border grains nor those containing fewer than 10 pixels. The number of grains detected and average grain diameter for all samples are given in Table 6.1.

Table 6.1 Grain size of HPT CuCrZr and annealed HPT samples, with Σ3 twin boundaries and border grains disregarded.

Sample ID	No. grains	Step size (nm)	Grain diameter (μm)	
			Mean	S.D.
HPT-AR	443	18	0.179	0.094
HPT-AR-200	229	34	0.211	0.073
HPT-AR-600	142	80	0.692	0.400
HPT-550	496	20	0.170	0.075
HPT-550-200	339	40	0.231	0.071
HPT-550-600	314	200	1.671	1.334

As can be seen in Table 6.1 the grain size of as-received and precipitation-hardened CuCrZr can be substantially reduced by applying severe plastic deformation using HPT, with the average grain diameter being ~80 μm for the original materials but less than 200 nm for both HPT materials. Subsequent annealing in a tube furnace at 200 °C caused a small increase in grain size of ~30 nm for the HPT-AR-200 sample and ~60 nm for the HPT-550-200 sample. When the annealing temperature was increased to 600 °C there was a considerable difference in grain growth between the two CuCrZr samples; an average grain size of <700 nm was retained in the HPT-AR-600 sample, whereas in the HPT-550-600 sample grains grew significantly and an average diameter of 1.67 μm was measured. Given the large number of turns, and thus the substantial induced strain, applied during HPT it could be assumed that the grain refinement had saturated throughout the sample [156, 157].

Is has been shown here that a variation in grain size can be achieved using HPT and subsequent annealing at different temperatures, with the average grain diameter for each sample characterised using EBSD. The interaction between this and test length-scale was then explored using nanoindentation.

6.2 Indentation size effect

6.2.1 Berkovich indentation

Indentation with a Berkovich tip was carried out using the multi-cycle displacement controlled method described in Section 3.13.2. An array of 12 indents was made on all polished samples, each to a final depth of 2 μm using ten load partial-unload cycles. As described previously, averaging across indents was performed within a Python routine and the final hardness and modulus results as a function of indentation depth for all HPT samples is shown in Figure 6.4.

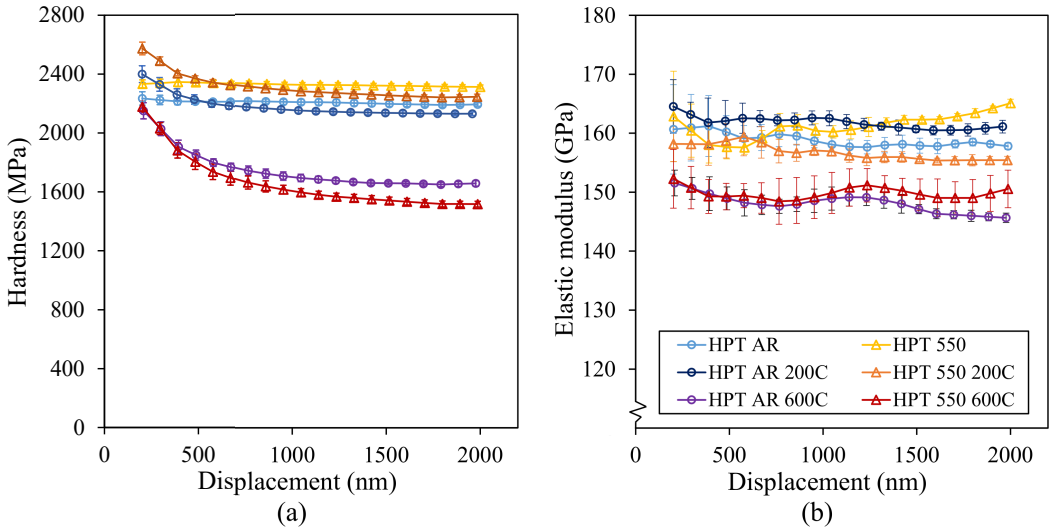

Fig. 6.4 Berkovich (a) hardness and (b) elastic modulus for all HPT material. Error bars represent one standard deviation.

As was seen in the large-grained CuCrZr samples, the elastic modulus values were significantly greater than that measured using an impulse excitation technique (130 GPa for as-received CuCrZr). Upon observation in an optical microscope it was found that this was again due to a large amount of pile-up around the indents, which was particularly evident when a polarised light filter was used to create topographical contrast. Images for the HPT-AR, HPT-AR-200, and HPT-AR-600 samples are shown in Figure 6.5.

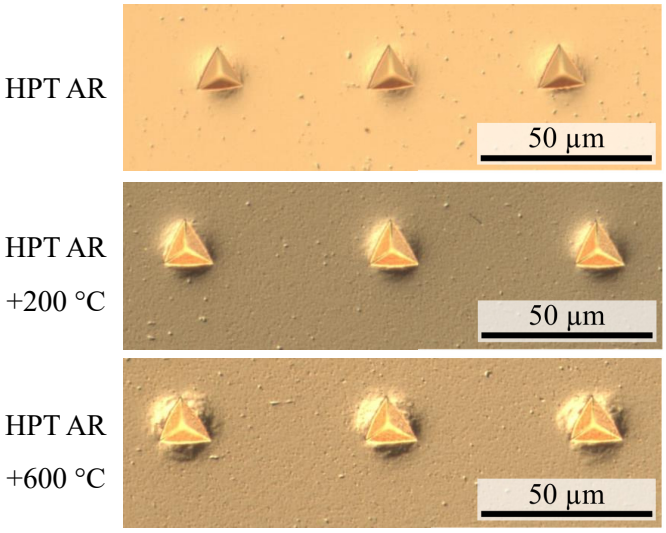

Fig. 6.5 Pile-up around Berkovich indents in the HPT-AR, HPT-AR-200, and HPT-AR-600 samples, as seen in the optical microscope.

As was addressed in the precious chapter, pile-up can cause an erroneously high calculation of both elastic modulus and indentation hardness due to an incorrect value for contact area.

Contact area corrections were made as described previously, by using the known sample elastic modulus to back-calculate contact area on a per-cycle basis and use these new values in the calculation of hardness. The corrected data can be seen in Figure 6.6. In this Figure, data for the original CuCrZr-AR and CuCrZr-550 samples have also been included for comparison.

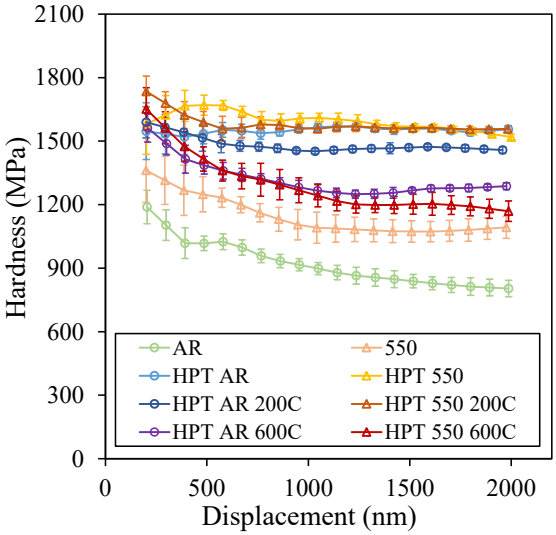

Fig. 6.6 Berkovich hardness for all HPT material, calculated using corrected contact area values.

It is interesting to note that there was very little scatter in any of the HPT data sets, as evident from the error bars being considerably smaller compared to the original CuCrZr Berkovich indentation data. This implies that there was a consistent response from individual indentations, which is likely due to the lack of anisotropy in the microstructure since each indent sampled multiple grains. This is even the case at small indentation depths, which also suggests a good quality surface finish was achieved during polishing.

There are several important observations that can be taken from Figure 6.6. Firstly, there is no indentation size effect (ISE) apparent in the data for both the HPT-AR and HPT-550 samples. This implies that mechanical testing performed on materials having a very small intrinsic length scale may produce results that are insensitive to the scale of the test piece, i.e. there is no extrinsic size effect. There is also little to no difference in response from the solid solution material compared to the precipitation-hardened CuCrZr, suggesting that in the HPT samples the grain boundary density is the dominant intrinsic length-scale. For the HPT-550 sample annealed at 200 °C and, to a lesser degree, the HPT-AR annealed sample, there is some ISE apparent in the first 500 nm of displacement; this is despite containing only slightly larger grains than their pre-annealed counterparts. Hardening due to precipitates also becomes evident, with a small but

consistent increase in indentation hardness for the HPT-550-200 material. After annealing at 600 °C the results for both samples are remarkably similar; it is likely that Cr precipitates have been grown in the HPT-AR-600 sample but the larger grain size in the HPT-550-600 material would counter-act any hardening due to precipitates. However it was not possible to confirm precipitate growth due to a lack of TEM data. A pronounced ISE can be seen in both samples annealed at 600 °C, and particularly in the first 1 μm of data, as was the case for the original CuCrZr samples.

6.2.2 Spherical indentation

Indentation using a spherical indenter was performed on all six HPT samples to observe the indentation size effect as a function of tip radius and strain. Tips of radii 8, 15, 30 and 90 μm were used to make arrays of indentations using a multi-cycle, load-controlled method described in Section 3.13.3. All indents were made to an approximate indentation strain of $\varepsilon = 0.2$ via 40 load partial-unload cycles and results from individual indents were averaged within a Python routine. Final (averaged) indentation stress-strain curves and elastic modulus values for the HPT-AR material tested with all tip radii can be seen in Figure 6.7.

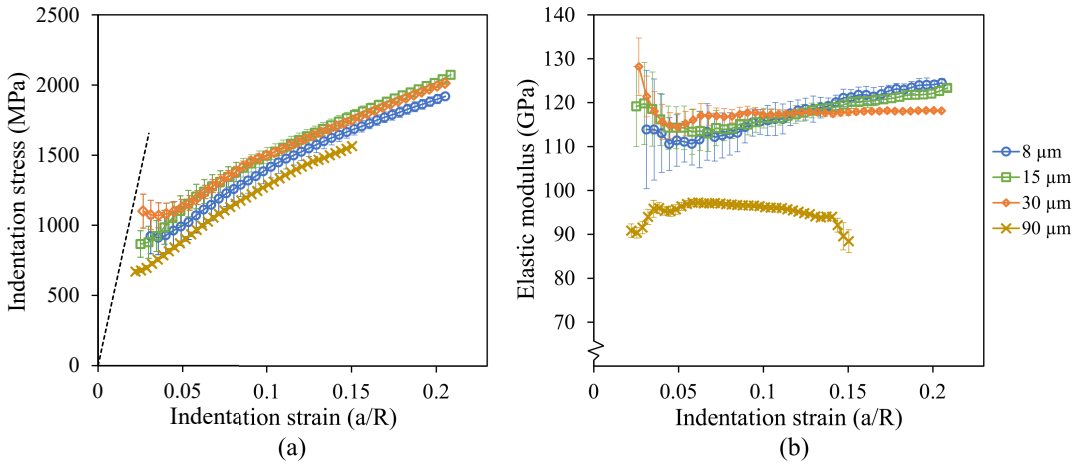

Fig. 6.7 Spherical (a) stress-strain and (b) elastic modulus data for the HPT-AR sample, all tip radii.

The results from the nano-grained HPT-AR material exhibit virtually no ISE, with indentation stress-strain curves for the different tip radii being almost indistinguishable from one another. Elastic moduli values for the 8, 15 and 30 μm tips are consistent and approximately correct for CuCrZr, however data for the 90 μm tip is significantly lower than expected. The

results from this tip for the other HPT and HPT annealed samples were similarly low and also had an unusual shape. To investigate why this may be the case the calibration procedure was repeated on fused silica and results indicated that the 90 μm tip no longer had a smooth profile, suggesting that it had been broken at some point after testing the original CuCrZr sample set. For this reason data produced by this tip unfortunately could not be used to analyse the HPT sample set.

Results for the HPT-AR, HPT-AR-200, and HPT-AR-600 samples, grouped by indenter tip radius, are shown in Figures 6.8 - 6.11 alongside the original CuCrZr-AR data. For completeness, and to demonstrate that the anomalous result discussed above was not sample-specific, data for the 90 μm tip has also been included. Results on the HPT sample set grouped by material can be found in Appendix C.

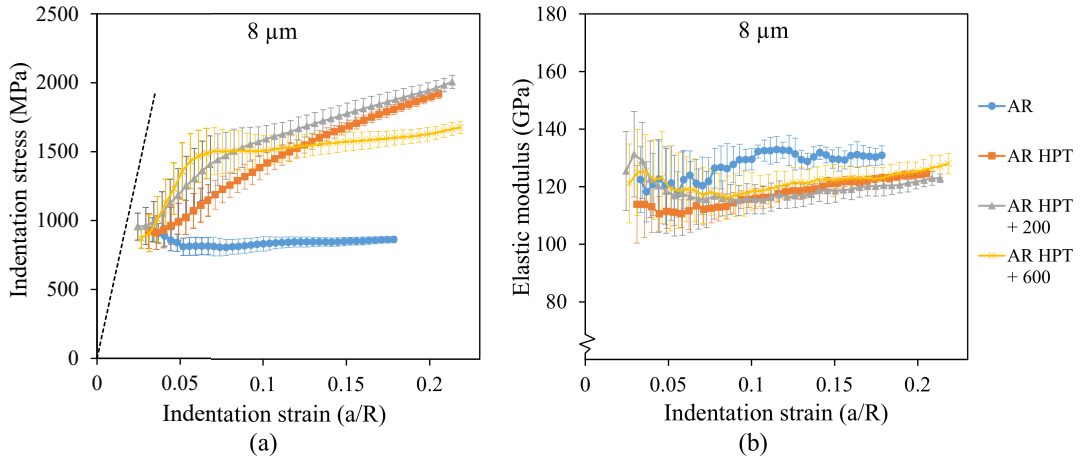

Fig. 6.8 Spherical (a) stress-strain and (b) elastic modulus data for 8 μm spherical tip in CuCrZr-AR and all HPT-AR samples.

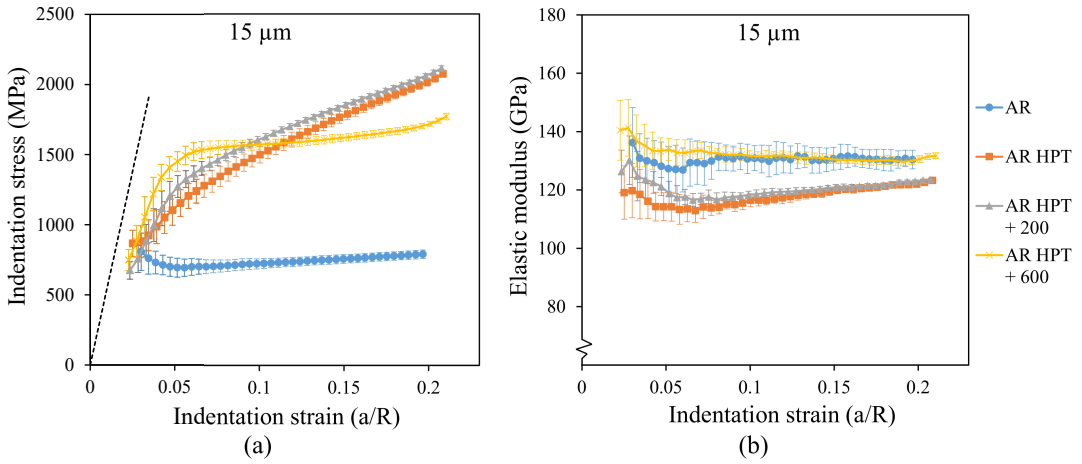

Fig. 6.9 Spherical (a) stress-strain and (b) elastic modulus data for 15 μm spherical tip in CuCrZr-AR and all HPT-AR samples.

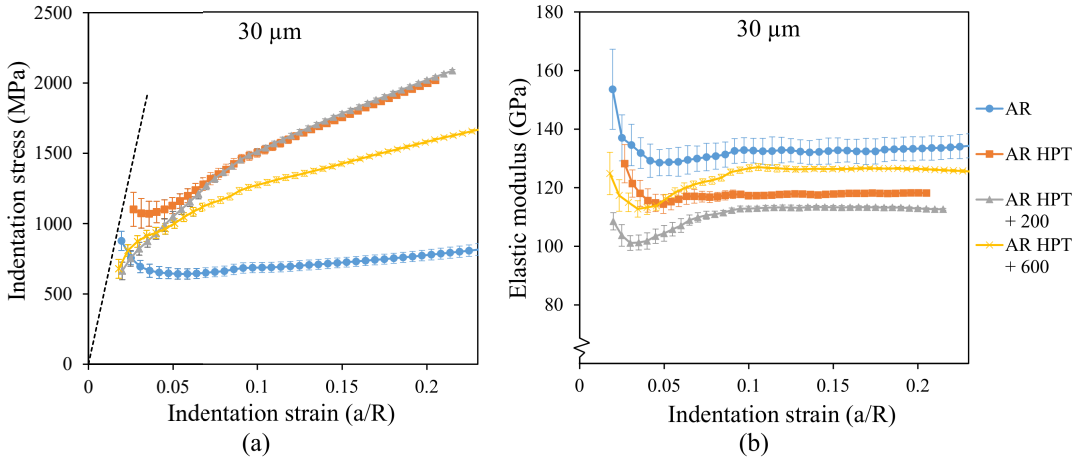

Fig. 6.10 Spherical (a) stress-strain and (b) elastic modulus data for 30 μm spherical tip in CuCrZr-AR and all HPT-AR samples.

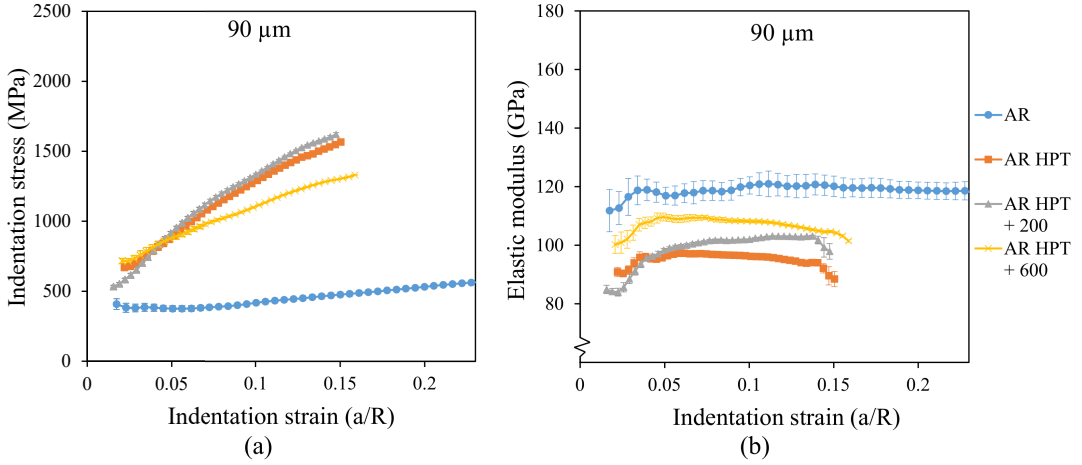

Fig. 6.11 Spherical (a) stress-strain and (b) elastic modulus data for 90 μm spherical tip in CuCrZr-AR and all HPT-AR samples.

Looking at data from all tips, it can be seen that at the start of the tests there is an almost identical response from all HPT-AR samples, i.e. at shallow depths indentation testing is insensitive to microstructural differences. The curves quickly deviate from each other as the tests progress, however, and effects due to differences in grain size becomes apparent. Both the HPT-AR and HPT-AR-200 samples exhibited significant strain hardening, which has commonly been observed in tensile tests for nano-grained materials along with a loss of ductility [158]. In indentation testing this is likely a result of dislocations being unable to flow further into the material, instead becoming trapped in a dense network beneath the indent. This was not seen in the HPT-AR-600 sample, which initially showed a sharp increase in hardness but quickly plateaued and minimal strain hardening was observed. There was little difference between results on the HPT samples from different tip radii and the elastic modulus values were fairly consistent, albeit with a slightly larger scatter in results from the 30 μm tip. This could potentially be due to sample mounting or frame stiffness as very high loads were required to reach strains of ε = 0.2. For example, 240 mN was required to produce a strain of ε = 0.2 for the HPT-AR sample compared to just 65 mN for the original CuCrZr-AR sample. The ISE was only evident for the HPT-AR-600 sample, which is clearest in the results within Appendix C where results from all tip radii are presented on a single plot.

Results for the original CuCrZr-550 and HPT-550 samples, again grouped by indenter tip radius, are shown in Figures 6.12 - 6.15.

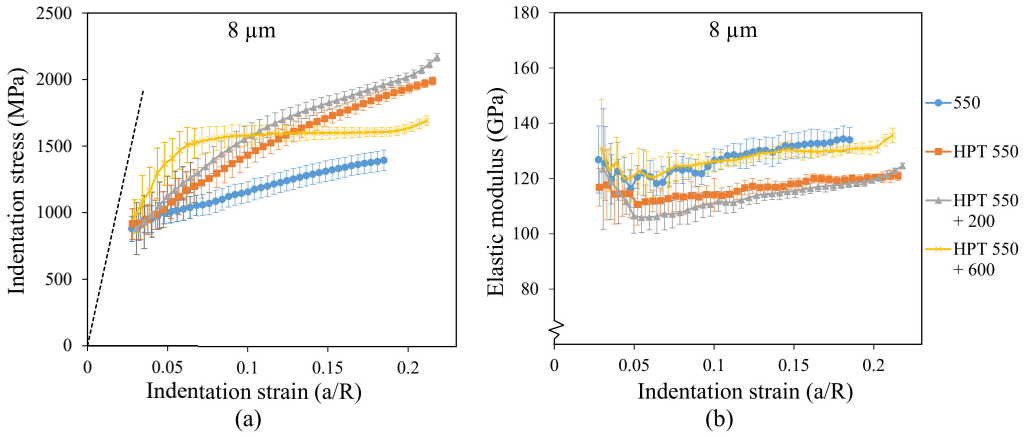

Fig. 6.12 Spherical (a) stress-strain and (b) elastic modulus data for 8 μm spherical tip in CuCrZr-550 and all HPT-550 samples.

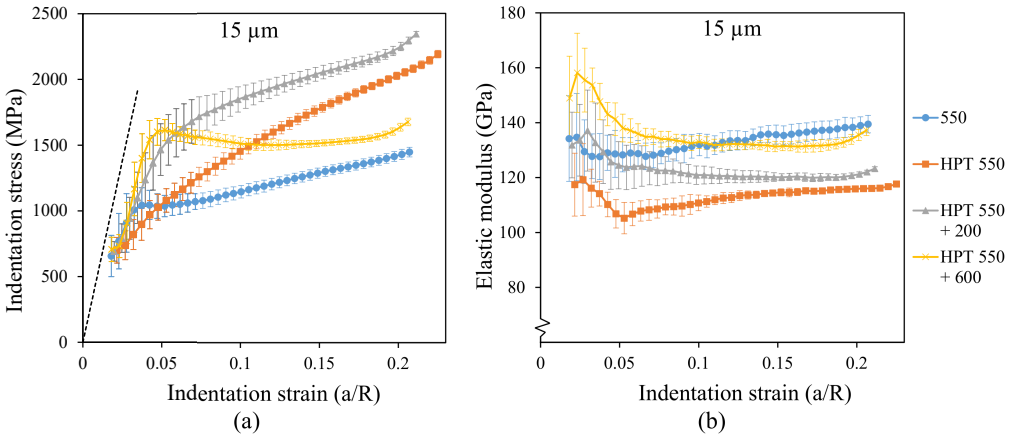

Fig. 6.13 Spherical (a) stress-strain and (b) elastic modulus data for 15 μm spherical tip in CuCrZr-550 and all HPT-550 samples.

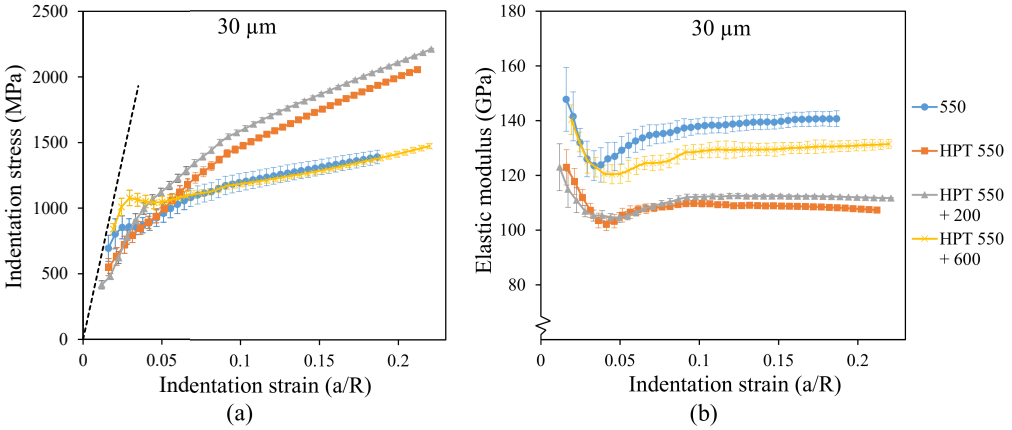

Fig. 6.14 Spherical (a) stress-strain and (b) elastic modulus data for 30 μm spherical tip in CuCrZr-550 and all HPT-550 samples.

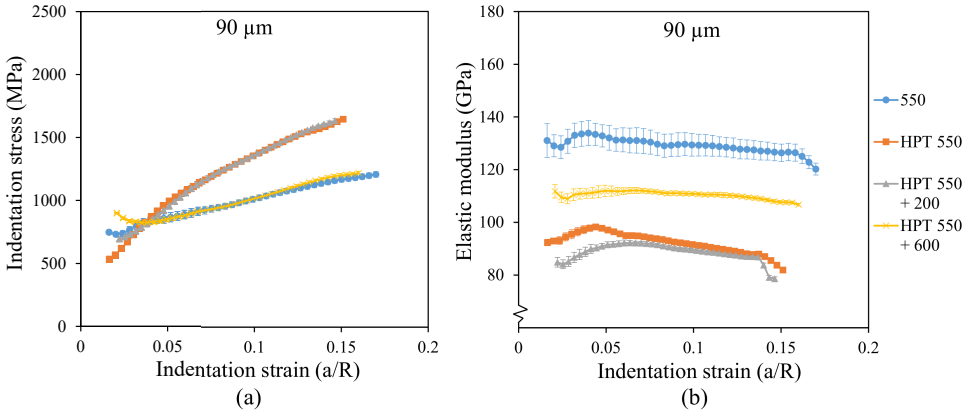

Fig. 6.15 Spherical (a) stress-strain and (b) elastic modulus data for 90 μm spherical tip in CuCrZr-550 and all HPT-550 samples.

As was seen in the HPT-AR data, an almost identical response was recorded from all variants of the HPT-550 sample at the initiation of plasticity. Also similar was the degree of strain hardening in the HPT-550 and HPT-550-200 samples. Interestingly, despite the HPT-550-200 sample having a larger grain size (230 nm) compared to the pre-annealed material (170 nm) it was consistently measured as being harder. This is likely due to the formation of precipitates, offering some degree of hardening in addition to the small grain size. Figure 6.14 demonstrates that after annealing the HPT-550 sample at 600 °C the measured hardness has returned to that of its original, coarse-grained state. This is only the case when indentation was carried out using the larger tip radii, however, and Figures 6.12 and 6.13 demonstrate that when the 8 and 15 μm tips were used there is a considerable difference in the measurements. Elastic modulus measurements on the HPT-550 and HPT-550-200 samples were ~15% lower than expected. This could have been due to sink-in but was difficult to confirm this in the SEM or optical microscope. If sink-in is the reason for this then the indentation stress values measured are slightly lower than the actual values, however they would not change considerably and so do not alter the overall trend between samples.

6.3 Discussion

A significant reduction in the grain size of solid solution (CuCrZr-AR) and precipitation hardened (CuCrZr-550) CuCrZr was achieved using high pressure torsion. Subsequent annealing in a tube furnace at 200 and 600 °C for ten minutes resulted in varying amounts of grain growth, as characterised using EBSD. Average grain diameters for the HPT-AR sample grew from 180 nm to 700 nm following annealing at 600 °C, and for the HPT-550 samples from 170 nm to 1.67 μm.

For the nano-grained materials it was found that there was a lack of sensitivity to extrinsic length-scale when measuring hardness using Berkovich indentation. When the grain size increased after annealing a size effect due to indentation depth returned, with the displacement range over which this occurred being associated with the grain diameter. For example, the HPT-550-200 sample with average grain size 230 nm only showed an increased hardness within the first 500 nm of indentation depth, whereas after annealing at the higher temperature the

indentation size effect was observed throughout the 2 μm displacement range. Little difference due to the addition of precipitates was seen.

Spherical indentation exhibited a similar response, with a change in tip radii having little influence on the measured indentation hardness for the nano-grained samples. Indentation stress-strain curves for all samples were almost coincident at the initiation of plasticity but quickly diverged as the variation in grain size began to impact on dislocation mobility, particularly for the HPT and HPT + 200 °C samples where considerable strain hardening was observed. Unfortunately data from the 90 μm tip could not be included in this analysis as the tip shape was no longer reliable, suspected to have been broken at some point after testing the original CuCrZr sample set.

Here it has been shown how grain sizes on the scale of ~100 nm interacts with the extrinsic length-scale. In the next Chapter an even smaller intrinsic length-scale will be created through the addition of fine irradiation defects.

Chapter 7

Changing the intrinsic length-scale: irradiation defects

The final change in intrinsic length-scale considered for this work was the addition of irradiation defects. CuCrZr will be used as a heat-sink material in divertor components of future fusion reactors, such as Iter, and in this application it will be subjected to bombardment from neutrons produced by reactions within the plasma. Due to this it will become radioactive, therefore in-service monitoring and end of life testing will have to be carried out using miniaturised samples in order to reduce risks associated with handling active material. Alternatively, irradiation using ions or protons can be used as a surrogate for neutron irradiation [159–161] since it is possible to induce similar types of damage without producing a radioactive sample (with some exceptions [108]). However this approach can only produce small volumes of irradiated material, with damage typically only extending several microns into the sample surface therefore experiments on these samples are again limited to micro-mechanical methods. It is for these reasons that it is important to understand how irradiation defects will interact with the extrinsic size effects and alter the material response when testing on the micron-scale.

For this work three of the CuCrZr samples were exposed to proton irradiation: the as-received (CuCrZr-AR), peak-aged (CuCrZr-480) and over-aged (CuCrZr-650) materials. Micro-pillar compression using pillars of three different sizes was then carried out at the University of California, Berkeley, on both irradiated and un-irradiated samples in order to investigate the difference in mechanical response with respect to a change in intrinsic and extrinsic length-scale.

Experiments were performed $in-situ$ whilst viewing with a scanning electron microscope (SEM) so that the deformation during testing could be observed, giving additional insight into the possible mechanisms operating in each case. Berkovich indentation was also performed on the irradiated samples to compare with results on the un-irradiated material.

7.1 Irradiation

Proton irradiation was carried out at the Dalton Cumbrian Facility, using the pelletron ion accelerator 'BABY' [115]. Full details of the set-up can be found in Section 3.4. For each sample an area of 10 x 10 mm was exposed to protons at 1 MeV and 25 μA in order to produce a 5 μm thick layer of approximately uniform damage of 0.4 dpa, as estimated using SRiM [116]. The predicted damage profile as a function of depth from surface can be seen in Figure 7.1.

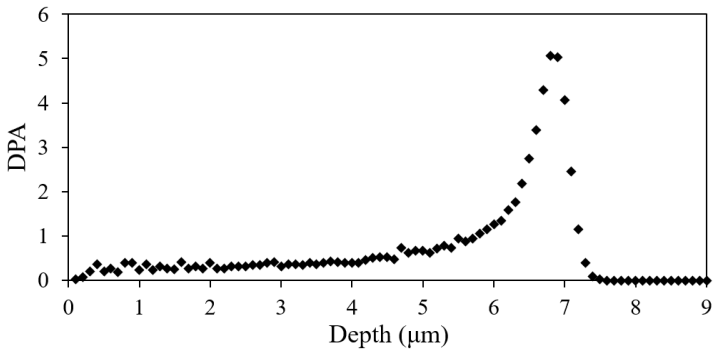

Fig. 7.1 Damage profile of proton irradiation.

Beam current, measured using Faraday cups, was recorded throughout each of the irradiations, along with three temperature measurements from thermocouples attached to the sample edges. These values were monitored so that small adjustments could be made to compensate for small fluctuations in the beam current and keep it roughly constant during each 6 hour run. Current hitting the stage and temperature measured by one thermocouple during irradiation of the CuCrZr-AR sample are shown in Figure 7.2.

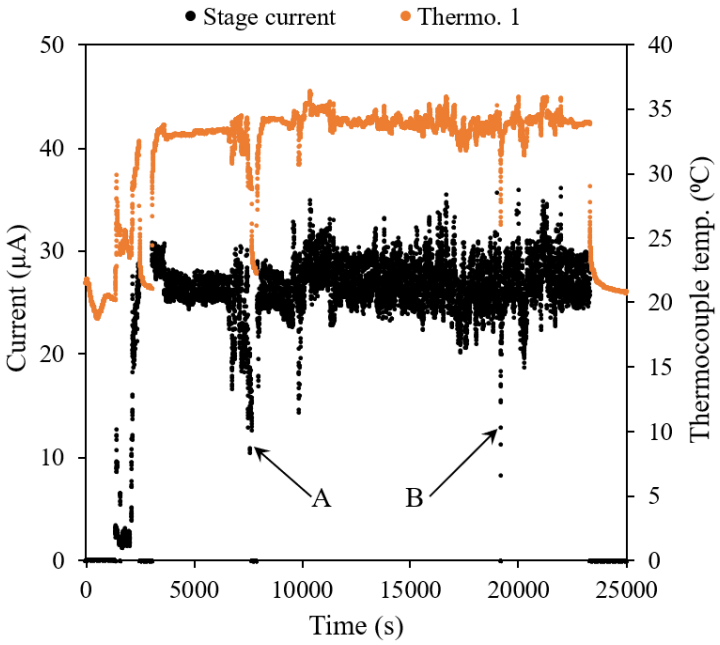

Fig. 7.2 Stage current (black) and thermocouple temperature (orange) data collected during irradiation of CuCrZr-AR. Points A and B indicated large fluctuations in the beam current.

The first ~45 minutes (2700 s) of data was collected whilst beam alignments were being made at a lower current. At some points (e.g. points A and B indicated in Figure 7.2) the current briefly fluctuated by a considerable amount but quickly recovered to around 27 μA, slightly higher than the original target. These large variations in current are reflected in a change in the sample temperature (measured by attached thermocouples) however water-cooling of the holder ensured that the sample did not exceed 40 °C. On two occasions the sample was temporarily shut off from the beam, which can be seen as values recorded at zero current, whilst magnets within the beam-line were adjusted to improve stability.

7.2 Sample characterisation

Following irradiation the samples were cross-sectioned to a thickness of 2 mm, polished on the newly exposed side, then mounted on pin stubs in such a way that the irradiated surface was perpendicular to the pin stub surface. This meant that the first 5 μm along one edge had through-thickness irradiation defects and the rest was the unirradiated bulk material. Once mounted the samples were observed within the SEM and it was found that large voids had formed along the irradiated edge. To better characterise these features a focused ion beam (FIB) was used to progressively remove thin (40 nm) slices from the irradiated CuCrZr-AR sample,

starting at the irradiated face and progressing deeper into the surface. Snapshots from this at 1 μm intervals are shown in Figure 7.3.

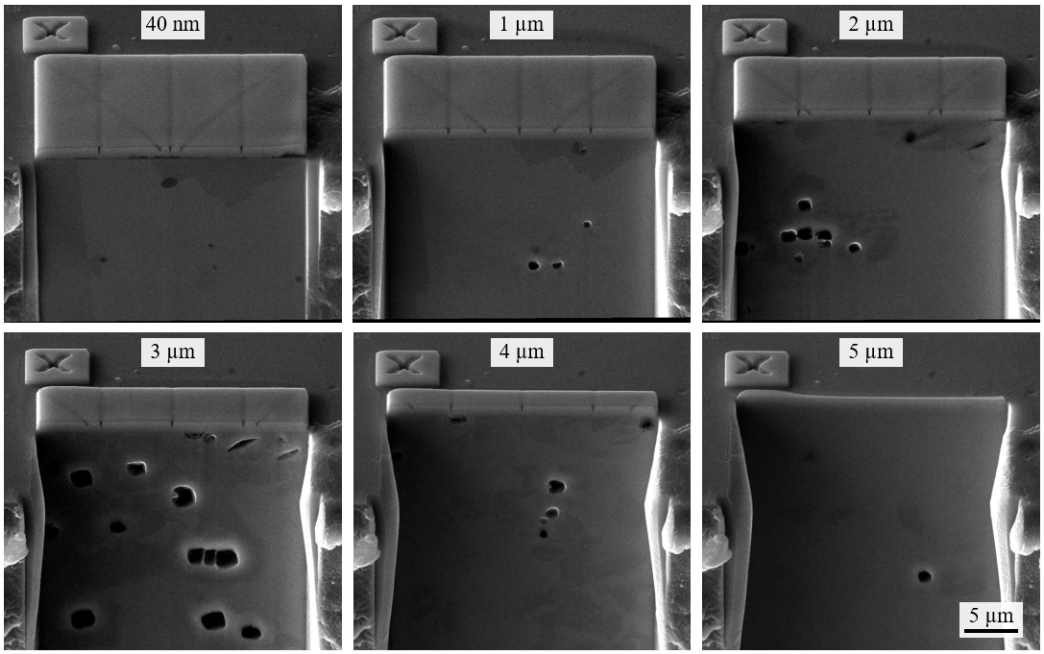

Fig. 7.3 SEM images from slice and view through the irradiated CuCrZr-AR sample. Lengths shown denote the distance between the irradiated surface and exposed face.

It is not clear what has caused such large voids to form in the irradiated samples but they seem to be surrounded by an irregular grain structure, as evident from the non-uniform contrast in the SEM images attributed to crystal orientation. Since protons were used for irradiation it is likely that hydrogen implantation has a role to play in the formation of these holes, however it was not possible to confirm this. Also, a comprehensive analysis of irradiation defects was not the aim of this work; the resultant microstructure and change in dominant intrinsic length-scale were the important aspects of these samples. Since there were areas containing fewer holes where large single grains were visible, these were chosen as sites for manufacturing pillars in order to avoid the effect of voids on the mechanical testing reported here.

Due to limited availability of instrument and operator time it was only possible to analyse the irradiated CuCrZr-650 material in the scanning transmission electron microscope (STEM). A thinned lamella was produced using the FIB lift-out technique and a FEI Titan scanning-TEM was again used to carry out electron energy loss spectroscopy (EELS) and was operated by Dr J. Lim, UKAEA. Cr precipitate size and spacing were characterised using two Cr elemental maps

and the method previously described in Chapter 5. A high-loss energy spectrum map showing one of the areas analysed is given in Figure 7.4.

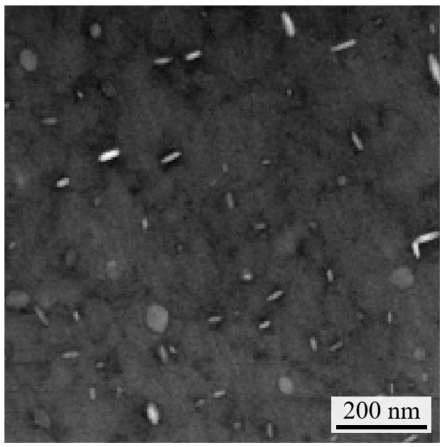

Fig. 7.4 EELS high-loss energy map for the range 670 - 900 eV, irradiated CuCrZr-650.

The spatial resolution of EELS data is lower than can be achieved with energy dispersive X-ray spectroscopy (EDS), however since it was likely that the over-aged alloy would have large precipitates this was not expected to greatly influence the measurements. Results from precipitate characterisation can be seen in Table 7.1. Maps were acquired in two different locations on the sample in order to image a larger area and obtain better statistics on the particle characteristics.

Table 7.1 Precipitate characteristics of irradiated 650 CuCrZr as measured using EELS.

Pixel size (nm)	**No. of precipitates counted**	**Precipitate diameter (nm)**	**Precipitate spacing (nm)**
5	85	24.9 ($\pm$ 11.2)	52.8
2	36	23.9 ($\pm$ 9.3)	51.2

The unirradiated CuCrZr-650 alloy had an average precipitate diameter of 16.0 ($\pm$ 7.0) nm and average spacing of 60.0 nm, therefore the results for the irradiated material show that precipitates had grown by ~50% and the spacing had also increased, although not by such a considerable amount. This precipitate growth could be due to heating at the sample surface, which was not necessarily reflected by the temperature measurements made by the thermocouples that were clamped at the edge of the irradiated region. However, it may also be an artefact due to measuring size using EELS data as opposed to to EDS. If precipitate size is measured using the EELS high-loss energy map for the unirradiated CuCrZr-650 sample

then the average diameter is calculated to be 20.4 nm, suggesting that the numbers given in Table 7.1 could be an over-estimation. Other work has suggested that for this alloy precipitate size does not change following irradiation; in a recent study by Hardie *et al.* [162] peak-aged CuCrZr was ion irradiated with 2 MeV Cu^{2+} ions to 0.2 dpa at temperatures from 125 to 440 °C. Although a change in hardness was observed throughout the temperature gradient (as measured using Berkovich indentation) EELS and atom probe tomography showed no change in average precipitate size.

7.3 Pillar compression testing

Pillars were fabricated using a focused ion beam (FIB); they were made within the first 5 μm of the front edge of the sample so that in the irradiated material they were completely contained within the irradiated region, and in both cases could be clearly viewed during testing. A schematic of the location of pillars with respect to the irradiated sample face is shown in Figure 7.5. Any obvious voids were avoided and pillars were re-made elsewhere if large holes became apparent during fabrication.

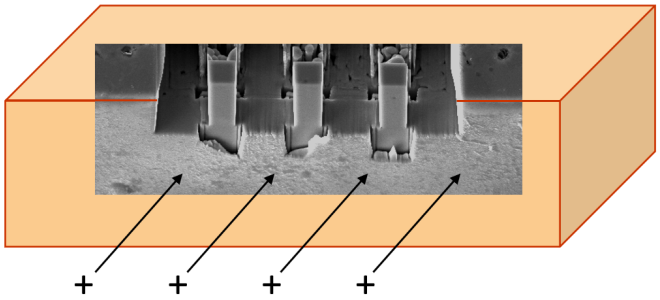

Fig. 7.5 Location of pillars (not to scale) with respect to irradiated edge, with the direction of incident protons indicated schematically as '+'.

Although cylindrical pillars are more commonly used for compression tests, tapering and FIB damage can affect the stress-strain response [163] therefore in this work pillars were made with a square cross-section. Three sizes of pillars were made in all samples: four with a width of 400 nm, four with a width of 1 μm, and three with a width of 4 μm. All had a constant width to height aspect-ratio of 1:2.5. Each group of same-sized pillars were milled within a single grain but it was not possible to fit all pillars of different sizes within the same grain, therefore the crystal orientation varied between pillars. EBSD was used to obtain the pillar

normal orientation for all pillars used in the experiments as well as the Schmid factor, which is needed in the calculation of resolved shear stress (RSS). As was shown in Chapter 2, critical resolved shear stress (CRSS) is the shear stress required to initiate slip on a single slip plane and can be calculated using the following equation,

$$\tau_c = m\frac{F}{A} \tag{7.1}$$

where m is the Schmid factor, a term that describes the relative orientation between crystal orientation and the direction of applied force (see Eq. 2.6). Results from pillars contained within different grains can therefore be compared by normalising by their associated Schmid factors.

Experiments were carried out using a Hysitron PI88 indenter, which was operated by Mr H. Vo within a FEI Quanta 3D FIB/SEM. Samples were first visually aligned, then after mounting the rig in the FIB fine adjustments could be made to the sample's x, y, and z position (not rotation). Before starting the pillar compression tests, a tip calibration was performed by indenting into bulk material; this was done to check the linear response of the piezoelectric load cell with respect to displacement. A flat-punch tip was used with radius 15 μm and care was taken to accurately position the middle of the tip directly over the top of the pillar so that it was not compressed off-centre. All tests were performed at a constant strain rate of 0.025 s^{-1} and compression was stopped after a displacement of 20 % of the pillar height, or sooner if contact was made between a section of slipped pillar and the surrounding material. During testing live imaging was recorded throughout the test, often using a reduced area window and fast acquisition time. The indenter software recorded load (in V and μN), displacement (in V and nm) and time (s). An example of the raw load-displacement results for one pillar can be seen in Figure 7.6 and snapshots taken during the same test are shown in Figure 7.7.

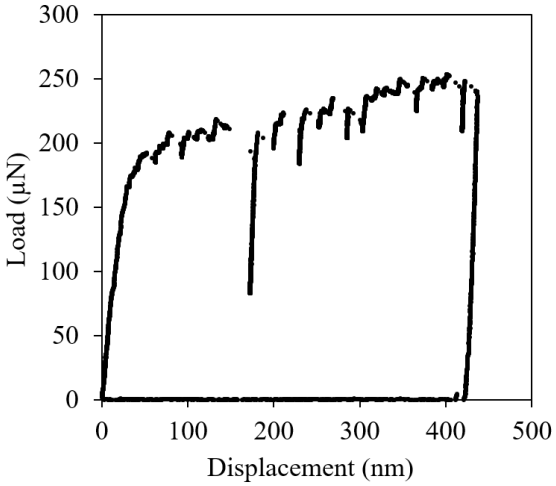

Fig. 7.6 Raw load-displacement results for a 4 μm pillar in un-irradiated CuCrZr-AR.

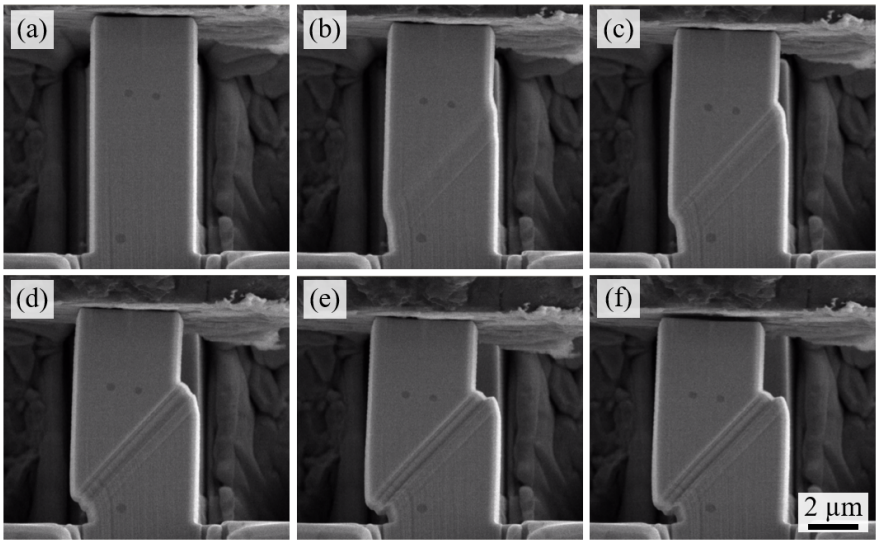

Fig. 7.7 Snapshots of the deformation during compression of a 4 μm pillar in as-received, unirradiated CuCrZr taken at (a) 1s, (b) 3s, (c) 5s, (d) 9s, (e) 12s and (f) 15s.

A modified MatLab code (originally written by Dr C. Hardie [134]) was used to process raw data as described in Section 3.14. It was found that the pillars did not have perfectly square cross-sections and instead tended to be slightly wider on the back face that was shadowed from the Ga-beam during milling of the pillar edges. The cross-sectional area, a, was therefore calculated using the equation for a trapezium,

$$a = \frac{w_1 + w_2}{2} \times d \tag{7.2}$$

where w_1 and w_2 are the widths as measured at the back and front of the pillar, and d is the pillar depth. These dimensions are also shown on Figure 7.8(a). The initial height of the pillar was measured just before compression, as shown in Figure 7.8(b).

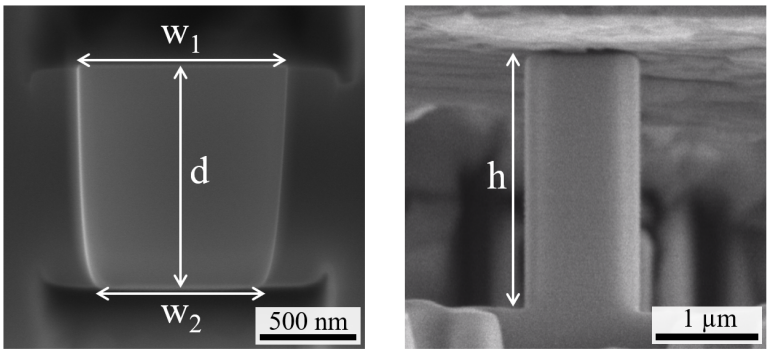

(a) (b)

Fig. 7.8 Measurements of (a) pillar cross-sectional area and (b) pillar height used in the calculation of engineering stress and strain.

Values for engineering stress were then converted into resolved shear stress (RSS) using the Schmid factors acquired by EBSD. Final data for all individual pillar experiments can be found in Appendix D in the form of RSS versus engineering strain. Results from pillars in the same set - i.e. the same size from the same sample - were extremely consistent, suggesting that the technique was highly repeatable. To examine any trends across all samples and pillar sizes, results for a single pillar from each set are shown in Figure 7.9. Note that the same y-axis range has been used for all plots to facilitate cross-comparison between pillars.

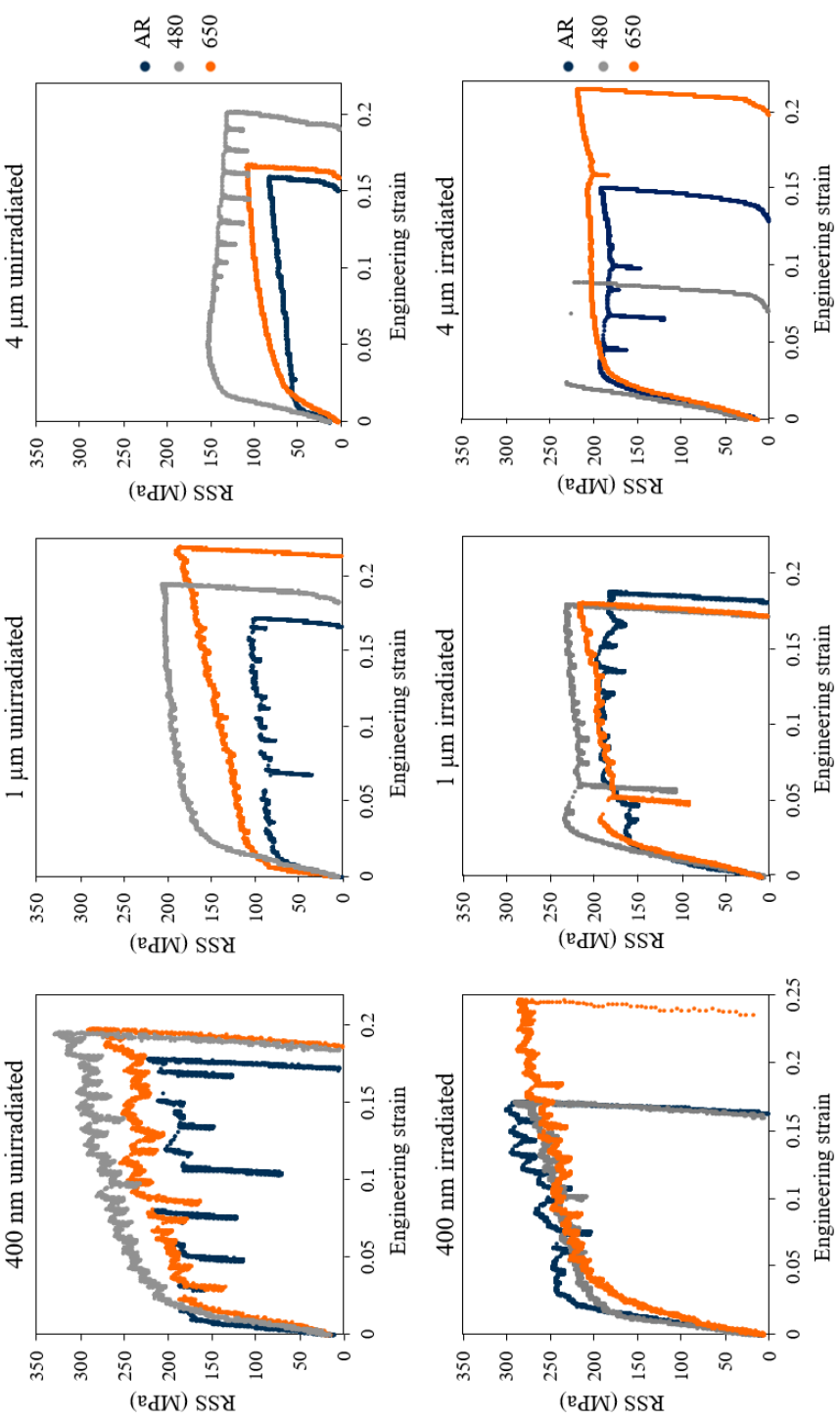

Fig. 7.9 A summary of engineering stress-strain curves for all samples, using one representative example from each pillar set.

Looking firstly at the unirradiated material it is clear that both intrinsic and extrinsic size effects are influencing the measured mechanical response. The highest strengths were recorded for the 400 nm pillars in all materials, with the 4 μm pillars exhibiting the lowest strength. The peak-aged CuCrZr was also the strongest material when tested in all pillar dimensions, as expected.

Results for the irradiated material show diminished size effects, with only the 400 nm pillars measuring as slightly stronger than the 1 and 4 μm pillars that showed a similar response. There was also little observed difference between ageing conditions, particularly for the smallest pillars where results from all three irradiated alloys were indistinguishable. Irradiation hardening was exhibited for all irradiated materials.

There wasn't a considerable difference in the general deformation behaviour between unirradiated and irradiated pillars. Large strain bursts were observed in both conditions, however the magnitude of these was typically larger in the irradiated materials compared to their unirradiated counterparts. This was particularly true of the irradiated CuCrZr-AR and CuCrZr-480 samples, where several pillars exhibited sudden and significant slip in one plane that was sufficient for the indenter tip to lose contact with the pillar. An example of this can be seen in Figure 7.9 for the 4 μm pillar of irradiated CuCrZr-480.

7.4 Indentation of irradiated CuCrZr

Finally, Berkovich indentation was performed on the samples. A continual stiffness measurement (CSM) method was used as described in Section 3.13.2 to produce average hardness and elastic modulus data over a set displacement range. An array of 16 indents were made into each sample to a final depth of 2 μm, using a frequency of 45 Hz and a harmonic displacement of 2 nm. Hardness and elastic modulus measurements were averaged over the same range of 200 - 500 nm for all samples and the results for this can be seen in Figure 7.10.

The elastic modulus values were consistent and within 10 % of the known modulus of CuCrZr. The hardness values exhibited very little scatter, particularly for the unirradiated material, which indicates that there was a consistent response across the indented area.

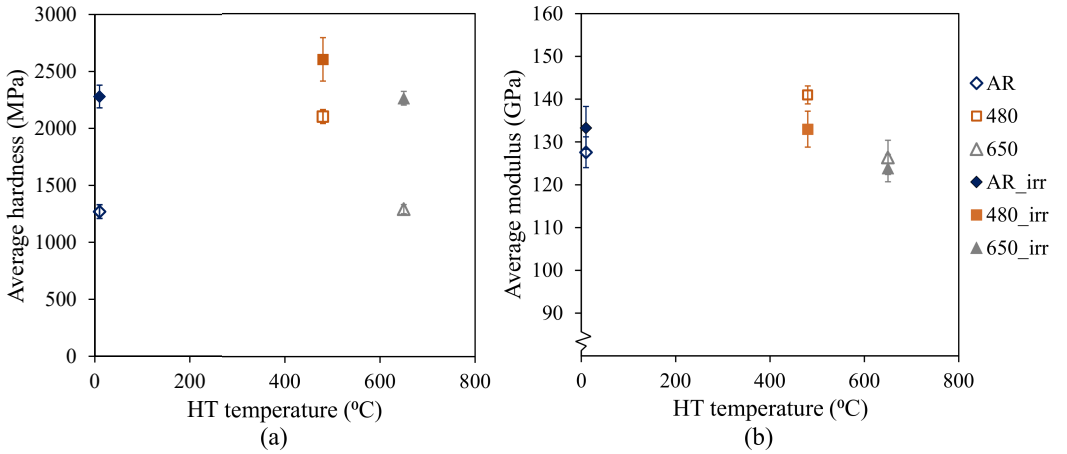

Fig. 7.10 Average (a) hardness and (b) elastic modulus (over the range 200 – 500 nm) for the irradiated and unirradiated AR, peak-aged and over-aged CuCrZr samples.

To observe the deformation around residual indent pits in all samples, indents were imaged in the SEM. One example image from each sample - unirradiated and irradiated - can be seen in Figure 7.11.

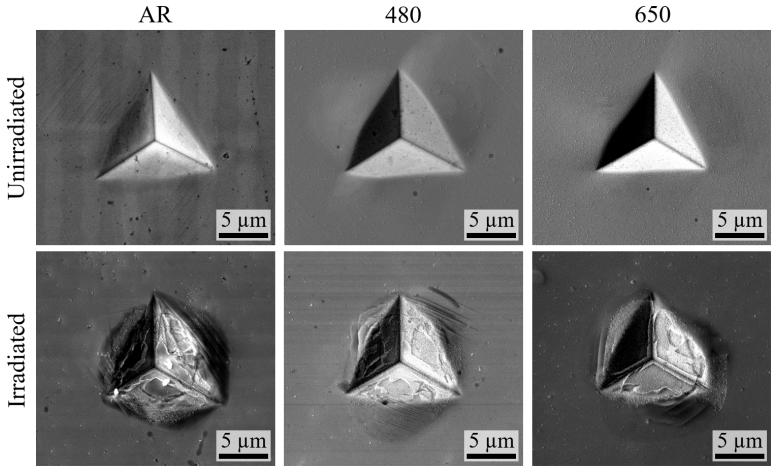

Fig. 7.11 Comparison of residual indentations in unirradiated (top row) and irradiated (bottom row) material.

The deformation topography suggests that there was increased strain localisation in the irradiated samples. One way in which this is evidenced is by slip steps being restricted to a smaller area compared to those seen in the unirradiated samples. For example in the CuCrZr-AR material slip steps can still be seen up to 10 μm from the edge of the indent pit in the unirradiated sample, whereas for the irradiated sample the slip steps extend to only half this distance. Although pile-up is difficult to observe in the SEM, the images in Figure 7.11 additionally suggest that the pile-up lobes are more significant in the unirradiated samples.

The patterning seen in the indent pits for the irradiated samples is likely just as a result of small amounts of surface contamination, which could not be removed without the risk of also removing some of the limited irradiated layer.

7.5 Discussion

In this Chapter three CuCrZr samples were proton-irradiated to investigate the change in mechanical response after fine irradiation defects were added to the microstructure. $In-situ$ micro-pillar compression testing was used to do this, with either three or four pillars made for each testing condition (i.e. size and sample variant). As was expected, pillars fabricated in the unirradiated peak-aged alloy were stronger than both the unirradiated as-received and over-aged alloys. Following irradiation, however, there was little to no variation in RSS across the three heat-treatment conditions, suggesting that the precipitate spacing was no longer the dominant length-scale determining strength.

It was shown that the presence of irradiation defects also inhibits the extrinsic size effect. Three pillar sizes were tested - having widths of 400 nm, 1 μm, and 4 μm - and only the smallest of these exhibited a slight increase in strength for the proton-irradiated samples. This is in contrast to results from the unirradiated samples, which showed an obvious size effect across all pillar dimensions. There was a small degree of scatter in data from pillars in the same sample set (i.e. one size in the same material), however this is to be expected since results are dependent on the microstructure of the individual pillar [93].

It is likely that irradiation defects determine the material response to plasticity, masking any other differences in microstructure and reducing the material volume required to produce length-scale independent results. This finding corresponds well with similar work on irradiated samples, in particular the *in situ* (TEM) compression tests in proton-irradiated Cu carried out by Kiener *et al.* [110]. The authors conclude that size-independent results can be obtained from ~400 nm diameter specimens, when deformation is controlled by dislocation-defect interactions. This effect is also discussed by Hosemann *et al.* [164] who reasons that only the very smallest pillars may show a size effect (approaching the theoretical maximum strength of the material) due to the geometrical restriction of dislocation sources, which scales inversely with the Orowan stress required to activate such sources.

Chapter 8

Discussion

Plasticity size effects are now widely recognised, especially in materials that deform via dislocations, however there is yet to be a unified theory that can describe the mechanisms behind such size effects. It has been shown that at smaller length-scales higher stresses are required to induce deformation and recognisable plasticity; since plastic flow requires the generation of many dislocations (through the operation of dislocation sources) these higher deformation stresses must therefore be related to the stress required to operate dislocation sources in a restricted volume. Based on this theory, Parthasarathy *et al.* [93] proposed the following source size model to examine sample size effects observed in critical resolved shear stress (CRSS) measurements from pillar compression experiments,

$$CRSS = \frac{\alpha Gb}{\overline{\lambda}_{max}} + \tau_0 + 0.5Gb\sqrt{\rho_{tot}} \tag{8.1}$$

The first term in this equation is the Orowan stress; G and b take their usual meanings of shear modulus and Burgers vector, respectively, and α is a dimensionless geometrical constant related to the character of the dislocations, which varies depending on whether they are edge, screw, or a combination of the two (as is more commonly observed). $\overline{\lambda}$ is the source length, which here describes the area available to a dislocation to bow out and multiply via the Frank-Read mechanism. The second term, τ_0, is the intrinsic shear strength of the material and describes the strength of the material in the absence of any length-scale effects. The last term is an expression to characterise forest hardening, i.e. the back-stress on the source caused by existing dislocations with density ρ_{tot}.

The experimental data presented in this thesis can be used to test whether the observed size dependence on material strength can be explained by a dislocation source model, or if other interactions also have to be considered. To do this, source length was compared with the length scale of the test. A source size model similar to that of Parthasarathy (Eq. 8.1) was used to calculate source length,

$$\lambda = \frac{0.2Gb}{0.4P_m - \tau_0 - 0.5Gb\sqrt{\rho}} \tag{8.2}$$

During indentation the stress below the tip has a maximum shear stress value of approximately 0.4 P_m, where P_m is the mean pressure, therefore this has been substituted in place of CRSS. The α term has been replaced with 0.2, representative of an averaged value for edge and screw dislocations.

The length scale of the test included contributions from both microstructure and the test dimension. Considering the stress distribution under an indenter, the shear stress is a maximum over a region beneath the indenter tip that has a dimension of approximately $0.35a$. Therefore in the case of testing single crystals, the length scale of the test was initially assumed to be $0.35a$ since it is within this region that sources will operate, with dislocations then being pushed down the strain gradient until they stop due to either an obstacle or a lack of driving force. For Berkovich indentations the contact radius was calculated from the contact area, A_c using $a = \sqrt{A_c/\pi}$.

The source size theory was initially tested using Berkovich data from single crystal pure Cu and CuCrZr-AR, as these represented the least complicated material systems and test conditions. For the calculation of source length it was assumed that the CuCrZr alloy had a higher intrinsic strength of 100 MPa, compared to 10 MPa for the pure Cu. The results of this can be seen in Figure 8.1.

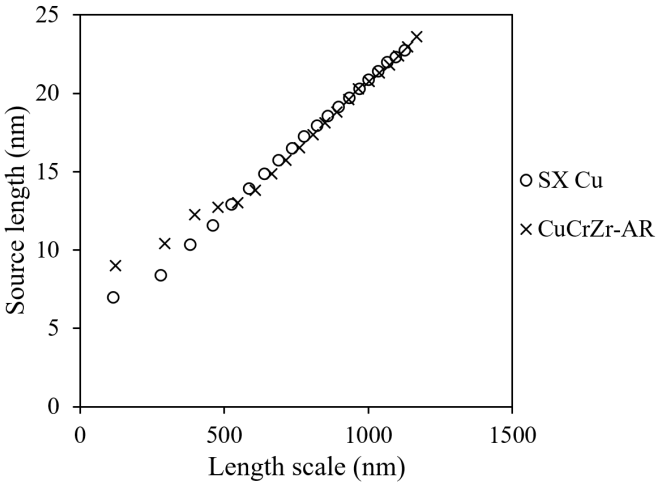

Fig. 8.1 Dislocation source size, as calculated from the Parthasarathy source size model, as a function of length-scale for pure Cu and CuCrZr-AR.

It was found that a linear relationship between source size and length scale could be achieved for both datasets by reducing the length scale from $0.35a$ to $0.2a$. This may reflect the fact that stress is more intense beneath a Berkovich indenter than previously assumed. Since strain is constant for Berkovich indentation (typically considered to be 7% uniaxial equivalent strain) ρ was taken to be constant at $5 \times 10^{14}\ m^{-2}$. The CuCrZr-AR alloy was considered to be single crystal as grains were sufficiently large compared to the size of indentation, therefore for both samples it was only contact size that has a strong influence on the source size and hence the measured hardness.

This approach was then applied to several other material systems to test its applicability when microstructural features were introduced. Berkovich data for two additional conditions from the CuCrZr sample set (CuCrZr-480 and CuCrZr-600), a nano-grained high pressure torsion CuCrZr sample (HPT-AR), and the annealed HPT CuCrZr samples (HPT-AR-200 and HPT-AR-600) were included in this analysis. For these materials, the grain size, precipitate spacing and stressed volume were combined as the sum of the inverse reciprocals (similar to the effective grain size described by Ehrler in [165]) to obtain the length-scale of the test, L:

$$\frac{1}{L} = \frac{1}{0.2a} + \frac{1}{L_P} + \frac{1}{L_D} \tag{8.3}$$

where L_P is precipitate spacing (or some factor of this) and L_D is average grain size. The CuCrZr-480 and CuCrZr-600 samples were considered to be single crystal and as such L only

contained contributions from the contact radius and precipitate spacing. Likewise, the HPT-AR and HPT-AR-200 samples contained no precipitates so the L_P term could be dropped. The HPT-AR-600 contained both precipitates and grain boundaries. The results for these samples are shown in Figure 8.2.

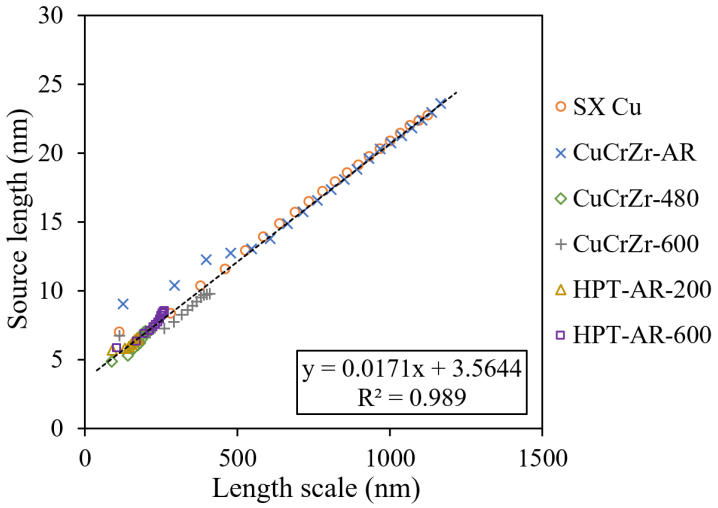

Fig. 8.2 Relation between dislocation source size and length scale for select samples.

Data was found to lie along a single line when the length scale associated to precipitates, L_P, was 20× the precipitate spacing. For the high strength materials - CuCrZr-480 and nano-grained HPT CuCrZr - the data was not as sensitive to changes in the scaling parameters, however grain size and precipitate spacing did have some influence on the source length. Dislocation density was again kept constant, implying that a change in GND density to accommodate the tip does not have a large effect on the hardness. This contradicts the early theories of Nix and Gao that strain gradients are responsible for the size effect.

Using the same set of parameters the model was applied to data from spherical indenters. The problem is more complex in this case due to the different radii of the indenters and the evolving strain history but allows the effects of yield and hardening to be explored. Eq. 8.2 was again used to calculate the source length, however the dislocation density was made to linearly increase with indentation strain, ε, using the function $\rho = (3 \times 10^{15})\varepsilon - 2 \times 10^{14}\ m^{-2}$. The results for the single crystal Cu tested using three tip radii can be seen in Figure 8.3. The trendline found for Berkovich data has been included for comparison.

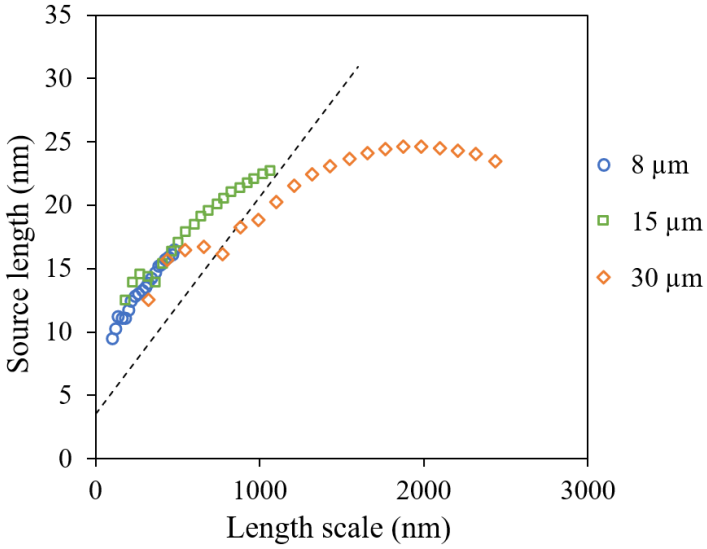

Fig. 8.3 Relation between dislocation source size and length scale for single crystal Cu spherical indentation data. The dashed line represents the trendline for Berkovich data.

A similar trend in source length was seen for all tip radii, with a slight deviation at larger length scales (equivalent to higher indentation strain). The indentation zone size results shown in Chapter 4 demonstrated that the evolution of zone size is not linear, therefore it may be that a more complex hardening relationship is required to more accurately model the spherical data.

Using the same method to combine microstructural parameters into one length scale, the analysis of spherical data was extended to samples that contain precipitates (CuCrZr-480) and grain boundaries (HPT-AR-200). Results for these samples alongside the single crystal Cu data are shown in Figure 8.4.

A higher rate of hardening was assumed for alloys with precipitates, with dislocation density linearly increasing as $\rho = (2 \times 10^{16})\varepsilon - 8 \times 10^{14}\ m^{-2}$. This was to reflect the fact that precipitates will trap dislocations, causing an increase in back-stress. The hardening rate was likewise increased for the nano-crystalline material, since dislocations pile-up at grain boundaries, also increasing back-stress: $\rho = (3 \times 10^{16})\varepsilon - 2 \times 10^{15}\ m^{-2}$. The strain-hardening response during spherical indentation was significantly affected by the addition of precipitates and nano-grains (see e.g. Figures 5.16 and 6.9) however it can be seen here that the source sizes do not vary considerably. This suggests that dislocations may pile-up close to sources and cannot move away, not greatly changing the source size but making them more difficult to operate due to the aforementioned back-stresses.

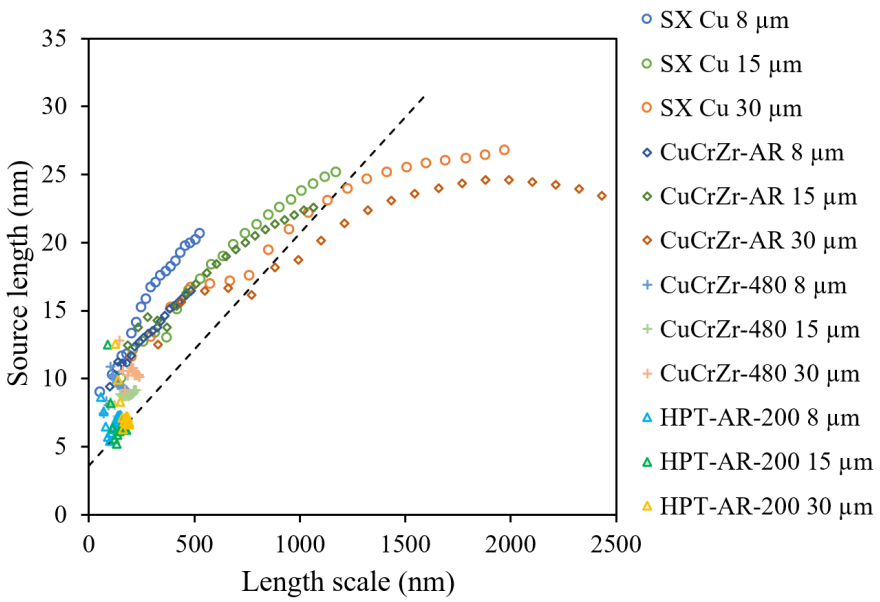

Fig. 8.4 Relation between dislocation source size and length scale for all spherical indentation data. The dashed line represents the trendline for Berkovich data.

It is more difficult to use this analysis approach for the data from pillar compression experiments because results are individual to each pillar, whereas the indentation data is averaged over many experiments. Nevertheless, the overall trend in results shown in Chapter 7 suggest that irradiation introduces defects that appear to dominate the length-scale of the system, raising the yield stress. With the close proximity of free surfaces, once shear bands have formed they are able to propagate freely at constant stress. This type of shear band formation has been observed in other tests on irradiated materials [110].

Overall, this analysis would suggest that the size dependence of measured strength on both microstructural features and sample dimensions can be described by a single length - the dislocation source length. A similar approach to combining length-scales was reported by Hou and Jennett [99], however they do this in the context of a slip distance theory that describes size effects as being as a result of the average slip distance of dislocations, which is reduced by obstacles or indentation size. The analysis presented here is instead in support of earlier thinking (by e.g Erhler *et al.* [165], Dunstan *et al.* [95]) that it is the dimensional constraint on the strained volume - be that by intrinsic microstructural length-scales or extrinsic structure size - that causes the change in measured strength due to a restriction on dislocation curvature. At smaller length scales the space available for dislocation multiplication is reduced and sources become more difficult to operate, leading to a rise in the shear stress required to produce plastic

deformation. In addition to this, the small source lengths suggest homogeneous nucleation of dislocations is the dominant mechanism rather than operation of existing sources. This would also explain the presence of pop-ins observed during loading with spherical indenters.

In the context of developing a strategy for small-scale testing in the nuclear industry, performing micro-pillar compression experiments is not yet a practical solution due to the complicated requirements on sample preparation and the fact that results will be scattered by the microstructure of individual pillars. The results from spherical indentation testing are useful for research applications but remain difficult to interpret in terms of complex hardening rates. Based in the results of this thesis, the simplest model for translating the size-dependent strength from small-scale tests to engineering length-scales is from the Berkovich indentation. By using a multi-cycle indentation protocol and performing characterisation of the material microstructure, the relationship between source size (related to the applied stress) and length-scale allows for translation to other tests or material sizes. This approach shows the most promise for the development of verifiable methods for use in critical industries.

Chapter 9

Summary, Conclusions and Future Work

This thesis is contains four main experimental chapters. In Chapter 4 nanoindentation results were obtained on single crystal copper, with the aim being to understand extrinsic size effects in a material with no obvious intrinsic length scale. Spherical and Berkovich indentation tests quantified the indentation size effect (ISE), which exhibits as an increase in strength at decreasing tip radii or indentation depth, respectively. Additionally, an attempt was made to measure the deformed area induced by spherical indentation in order to estimate the test size as a function of tip radius and indentation strain.

Chapter 5 presented experiments carried out on CuCrZr, a precipitation-hardened alloy. By heat-treating the as-received material at different temperatures a sample set was produced that had a variation in precipitate size and spacing. Berkovich and spherical nanoindentation were performed on theses samples to evaluate the effect of introducing an intrinsic length-scale in the form of solutes and precipitates.

The effect of varying grain size was explored in Chapter 6. By subjecting the solid-solution alloy and one of the precipitation-hardened CuCrZr samples to high pressure torsion, nanograins were created within the microstructure. Subsequent annealing at 200 and 600 °C grew the grains to ultimately produce a set of samples with a range in grain size.

Lastly, Chapter 7 looked at the effect of adding fine irradiation defects to the CuCrZr microstructure. Three CuCrZr samples were proton irradiated and micro-pillar compression

testing, using three different pillar dimensions, was carried out within the thin irradiated layer using . The same tests were also performed on the unirradiated alloys in order to depict differences in deformation behaviour.

The Discussion focused on select data from across the experimental chapters, which were used to provide insight into the possible mechanisms that give rise to observed size effects in indentation. A source size model was used to estimate the length of dislocation sources operating during deformation and the evolution of this was considered as a function of a length-scale that combined both the microstructural and test dimension length-scales. A brief summary of the main conclusions and proposed future work are given below.

9.1 Conclusions

- Observations made of the deformed region beneath nanoindentations and the distribution of calculated geometrically necessary dislocation (GND) density suggested that the extent of the plastic zone size is much smaller than current approximations.

- Berkovich and spherical indentation were used to quantify the indentation size effect (ISE) in materials with a range of intrinsic length-scales associated to microstructural features. It was found that the ISE was evident at yield, which cannot be explained by strain gradient plasticity (SGP) theory since there are no GNDs at the initiation of plasticity.

- Micro-pillar compression experiments were carried out on three proton- irradiated CuCrZr samples. In the un-irradiated material the results exhibited size effects due to both the pillar dimensions as well as differences in precipitate spacing. Following irradiation, however, an increase in strength was only measured for the smallest (400 nm width) pillars with no difference in measurements made on the 1 and 4 μm pillars. The intrinsic size effect was also completely obscured, suggesting that the fine irradiation defects dominate the dislocation behaviour during deformation.

- A source size model similar to that developed by Parthasarathy [93] was used to estimated the dislocation source length using indentation results obtained on several material systems. It was found that microstructural features and the size of the strained volume can be

combined and expressed by a single length scale, which is related to dislocation source length. At smaller length scales it becomes more difficult for dislocation sources to operate and multiply, and it was suggested that this is the origin of both extrinsic and intrinsic size effects.

- The data from Berkovich indentation appeared to be easier to interpret due to the fact that testing is carried out at constant strain, whereas for the spherical data a linear relationship to be introduced to characterise the increase in dislocation density as a function of indentation strain. This suggests that Berkovich data could be used to predict size-independent data.

9.2 Future work

To explore some of the aspects of the current work further it would be beneficial to carry out the following as part of future work:

- In order to test the source size theory at larger scales, instrumented indentation using larger spherical tips (i.e. tip radii greater than 100 μm) should be performed. This would also identify the minimum test size required to produce a size-independent response.

- Using the GND density maps produced by CrossCourt, obtain an estimation of total GND density in the defined plastic zone to compare with findings by Demir et al [141] who reported a "*steep decay of the GND density for smaller indents*".

- It is possible that a slightly different rate of hardening should apply for each indenter radius in the calculation of source length, also that the increasing dislocation density should follow another relation rather than just linear. For example, Meyer's law could instead be used.

- Carry out source size analysis for data produced by the pillar compression experiments. This would entail characterisation of the proton-irradiated samples, requiring high-resolution transmission electron microscope (TEM) imaging to measure defect size and density, so that an accurate intrinsic length term could be established.

References

[1] S.R. Kalidindi and S. Pathak. Determination of the effective zero-point and the extraction of spherical nanoindentation stress-strain curves. *Acta Materialia*, 56(14):3523–3532, 2008.

[2] E. Orowan. Zur kristallplastizität. i. *Zeitschrift für Physik*, 89(9):605–613, Sep 1934.

[3] G.I. Taylor. The mechanism of plastic deformation of crystals. part i.—theoretical. *Proceedings of the Royal Society of London. Series A, Containing Papers of a Mathematical and Physical Character*, 145(855):362–387, 1934.

[4] M. Polanyi. Über eine art gitterstörung, die einen kristall plastisch machen könnte. *Zeitschrift für Physik*, 89(9-10):660–664, 1934.

[5] J. Burgers. Internal strains in solids. *Proc. Acad. Science*, 42:293, 1939.

[6] D. Hull and D.J. Bacon. *Introduction to Dislocations*. Butterworth-Heinemann, 2011.

[7] F.C. Frank and W.T. Read Jr. Multiplication processes for slow moving dislocations. *Physical Review*, 79(4):722, 1950.

[8] O.D. Sherby and J. Wadsworth. Ancient blacksmiths, the iron age, damascus steels, and modern metallurgy. *Journal of Materials Processing Technology*, 117(3):347 – 353, 2001.

[9] D.B. Wagner. *Science and Civilisation in China: Volume 5, Chemistry and Chemical Technology, Part 11, Ferrous Metallurgy*. Cambridge University Press, 2008.

[10] E.O. Hall. The deformation and ageing of mild steel: Iii discussion of results. *Proceedings of the Physical Society. Section B*, 64(9):747, 1951.

[11] N.J. Petch. The cleavage strength of polycrystals. *J. Iron Steel Inst.*, 174:25–28, 1953.

[12] R. Armstrong, I. Codd, R.M. Douthwaite, and N.J. Petch. The plastic deformation of polycrystalline aggregates. *Philosophical Magazine*, 7(73):45–58, 1962.

[13] J.R. Weertman. Hall-Petch strengthening in nanocrystalline metals. *Materials Science and Engineering: A*, 166:161–167, 1993.

[14] T. T. Zhu, A. J. Bushby, and D. J. Dunstan. Materials mechanical size effects: a review. *Materials Technology*, 23(4):193–209, 2008.

[15] J.C.M. Li. Petch relation and grain boundary sources. *Trans. Metall. Soc. AIME*, 227(1):239–247, 1963.

[16] M. Kato. Hall-petch relationship and dislocation model for deformation of ultrafine-grained and nanocrystalline metals. *Materials Transactions*, 55(1):19–24, 2014.

[17] M.F. Ashby. The deformation of plastically non-homogeneous materials. *The Philosophical Magazine: A Journal of Theoretical Experimental and Applied Physics*, 21(170):399–424, 1970.

[18] A.H. Chokshi, A. Rosen, J. Karch, and H. Gleiter. On the validity of the Hall-Petch relationship in nanocrystalline materials. *Scripta Metallurgica*, 23(c):1679–1684, 1989.

[19] C.C. Koch and J. Narayan. The inverse Hall-Petch effect - fact or artifact? In *Materials Research Society Symposium Proceedings*, page B5.1.1, 2001.

[20] J.R. Greer and J.Th.M. De Hosson. Plasticity in small-sized metallic systems: Intrinsic versus extrinsic size effect. *Progress in Materials Science*, 56(6):654–724, 2011.

[21] D.J. Dunstan and A.J. Bushby. Grain size dependence of the strength of metals: The Hall-Petch effect does not scale as the inverse square root of grain size. *International Journal of Plasticity*, 53:56–65, 2014.

[22] E. Arzt. Size Effects in Materials Due To Microstructural and Dimensional Constraints: a Comparative Review. *Acta mater*, 46(16):5611–5626, 1998.

[23] J.M. Fragomeni and B.M. Hillberry. A micromechanical method for predicting the precipitation hardening response of particle strengthened alloys hardened by ordered precipitates. *Acta Mechanica*, 138:185–210, 1999.

[24] Z. Guo and W. Sha. Quantification of precipitation hardening and evolution of precipitates. *Materials Transactions*, 43(6):1273–1282, 2002.

[25] V. Mohles and B. Fruhstorfer. Computer simulations of orowan process controlled dislocation glide in particle arrangements of various randomness. *Acta materialia*, 50(10):2503–2516, 2002.

[26] A.J. Kulkarni, K. Krishnamurthy, S.P. Deshmukh, and R.S. Mishra. Effect of particle size distribution on strength of precipitation-hardened alloys. *Journal of Materials Research*, 19(9):2765–2773, 2004.

[27] R. Santos-Güemes, B. Bellón, G. Esteban-Manzanares, J. Segurado, L. Capolungo, and J. LLorca. Multiscale modelling of precipitation hardening in Al-Cu alloys: dislocation dynamics simulations and experimental validation. *Acta Mater.*, 188:475–485, 2020.

[28] T. Hatano. Dynamics of a dislocation bypassing an impenetrable precipitate: the hirsch mechanism revisited. *Physical Review B*, 74(2):020102, 2006.

[29] S. Gao, M. Fivel, A. Ma, and A. Hartmaier. 3D discrete dislocation dynamics study of creep behavior in Ni-base single crystal superalloys by a combined dislocation climb and vacancy diffusion model. *J. Mech. Phys. Solids*, 102:209–223, 2017.

[30] S-W. Lee and W.D. Nix. Geometrical analysis of 3d dislocation dynamics simulations of fcc micro-pillar plasticity. *Materials Science and Engineering: A*, 527(7-8):1903–1910, 2010.

[31] F.R.N. Nabarro. The mechanical properties of metallic solid solutions. *Proceedings of the Physics Society*, 58:669–676, 1946.

[32] M.Z. Butt and P. Feltham. Solid-solution hardening. *Journal of Materials Science*, 28:2557–2576, 1993.

[33] R.L. Fleischer. Substitutional solution hardening. *Acta Metallurgica*, 11:203–209, 1963.

[34] R. Labusch. Statistical theories of solid solution hardening(concentration of solute atoms, interaction range between solute atoms and distortion, and interaction strength of solid solution hardening). *Acta Met.,(London)*, 20:917–927, 1972.

[35] F.R.N. Nabarro. The theory of solution hardening. *Philosophical magazine*, 35(3):613–622, 1977.

[36] R. Madec, B. Devincre, and L.P. Kubin. From dislocation junctions to forest hardening. *Physical review letters*, 89(25):255508, 2002.

[37] B. Devincre, L. Kubin, and T. Hoc. Physical analyses of crystal plasticity by dd simulations. *Scripta Materialia*, 54(5):741 – 746, 2006. Viewpoint set no. 39: Statistical mechanics and coarse graining of dislocation behavior for continuum plasticity.

[38] P. Landau, R.Z. Shneck, G. Makov, and A. Venkert. In-situ TEM study of dislocation patterning during deformation in single crystal luminum. *Journal of Physics: Conference Series*, 241:012060, jul 2010.

[39] P. Li, S.X. Li, Z.G. Wang, and Z.F. Zhang. Fundamental factors on formation mechanism of dislocation arrangements in cyclically deformed fcc single crystals. *Progress in Materials Science*, 56(3):328 – 377, 2011.

[40] S.S. Brenner. Tensile strength of whiskers. *Journal of Applied Physics*, 1956.

[41] N. A. Fleck and J. W. Hutchinson. A phenomenological theory for strain gradient effects in plasticity. *Journal of the Mechanics and Physics of Solids*, 41:1825–1857, 1993.

[42] M.D. Uchic, D.M. Dimiduk, J.N. Florando, and W.D. Nix. Sample dimensions influence strength and crystal plasticity. *Science*, 305(5686):986–989, 2004.

[43] C. Motz, T. Schöberl, and R. Pippan. Mechanical properties of micro-sized copper bending beams machined by the focused ion beam technique. *Acta Materialia*, 53:4269–4279, 2005.

[44] R.L. Smith and G.E. Sandly. An accurate method of determining the hardness of metals, with particular reference to those of a high degree of hardness. *Proceedings of the Institution of Mechanical Engineers*, 102(1):623–641, 1922.

[45] V. Ashworth, W.A. Grant, and R.P.M. Procter. *Ion implantation into metals: proceedings of the 3rd International Conference on Modification of Surface Properties of Metals by Ion Implantation, held at UMIST, Manchester, UK, 23-26 June 1981*. Elsevier, 1981.

[46] J.B. Pethica, R. Hutchings, and W.C. Oliver. Hardness measurement at penetration depths as small as 20 nm. *Philos. Mag. A Phys. Condens. Matter, Struct. Defects Mech. Prop.*, 48(4):593–606, 1983.

[47] J.L. Loubet, J.M. Georges, O. Marchesini, and G. Meille. Vickers indentation curves of magnesium oxide (mgo). *Journal of tribology*, 106(1):43–48, 1984.

[48] M. F. Doerner and W. D. Nix. A method for interpreting the data from depth-sensing indentation instruments. *J. Mater. Res.*, 1(4):601–609, 1986.

[49] W.C. Oliver and G.M. Pharr. An improved technique for determining hardness and elastic modulus using load and displacement sensing indentation experiments. *Journal of Materials Research*, 7(6):1564–1583, 1992.

[50] S.M. Han, R. Shah, R. Banerjee, G.B. Viswanathan, B.M. Clemens, and W.D. Nix. Combinatorial studies of mechanical properties of ti–al thin films using nanoindentation. *Acta Materialia*, 53(7):2059 – 2067, 2005.

[51] M. Dietiker, R.D. Nyilas, C. Solenthaler, and R. Spolenak. Nanoindentation of single-crystalline gold thin films: Correlating hardness and the onset of plasticity. *Acta Materialia*, 56(15):3887–3899, 2008.

[52] A.E. Ozmetin, O. Sahin, E. Ongun, and M. Kuru. Mechanical characterization of MgB2 thin films using nanoindentation technique. *Journal of Alloys and Compounds*, 619:262–266, 2015.

[53] D.E.J. Armstrong, C.D. Hardie, J.S.K.L. Gibson, A.J. Bushby, P.D. Edmondson, and S.G. Roberts. Small-scale characterisation of irradiated nuclear materials: Part II nanoindentation and micro-cantilever testing of ion irradiated nuclear materials. *Journal of Nuclear Materials*, 462:374–381, 2015.

[54] C.D. Hardie, S.G. Roberts, and A.J. Bushby. Understanding the effects of ion irradiation using nanoindentation techniques. *Journal of Nuclear Materials*, 462:391–401, 2015.

[55] A. Reichardt, A. Lupinacci, D. Frazer, N. Bailey, H. Vo, C. Howard, Z. Jiao, A.M. Minor, P. Chou, and P. Hosemann. Nanoindentation and in situ microcompression in different dose regimes of proton beam irradiated 304 ss. *Journal of Nuclear Materials*, 486:323 – 331, 2017.

[56] W.D. Nix and H.J. Gao. Indentation size effects in crystalline materials: A law for strain gradient plasticity. *Journal of the Mechanics and Physics of Solids*, 46(3):411–425, 1998.

[57] K. W. McElhaney, J. J. Vlassak, and W. D. Nix. Determination of indenter tip geometry and indentation contact area for depth-sensing indentation experiments. *Journal of Materials Research*, 13(5):1300–1306, 1998.

[58] Y.Y. Lim and M.M Chaudhri. The effect of the indenter load on the nanohardness of ductile metals: an experimental study on polycrystalline work-hardened and annealed oxygen-free copper. *Philosophical Magazine A*, 79:2979–3000, 1999.

[59] K. Durst, B. Backes, and M. Göken. Indentation size effect in metallic materials: Correcting for the size of the plastic zone. *Scripta Materialia*, 52(11):1093 – 1097, 2005.

[60] Y. Huang, F. Zhang, K.C. Hwang, W.D. Nix, G.M. Pharr, and G. Feng. A model of size effects in nano-indentation. *Journal of the Mechanics and Physics of Solids*, 54(8):1668 – 1686, 2006.

[61] M. Rester, C. Motz, and R. Pippan. Microstructural investigation of the volume beneath nanoindentations in copper. *Acta Materialia*, 55(19):6427–6435, 2007.

[62] J. Brinell. Sätt att bestämma kroppars hårdhet jämte några tillämpningar of detsamma. *Teknisk Tidskrift*, 5:69–87, 1900.

[63] E. Meyer. Untersuchungen über härteprüfung und härte brinell methoden. *Des Vereines Deutscher Ingenieure*, 52:645–654, 1908.

[64] D. Tabor. *The hardness of metals*. Oxford: Clarendon Press, 1951.

[65] Y.Y. Lim, A.J. Bushby, and M.M. Chaudhri. Nano and macro indentation studies of polycrystalline copper using spherical indenters. *MRS Online Proceedings Library Archive*, 522, 1998.

[66] J.S. Field and M.V. Swain. A simple predictive model for spherical indentation. *Journal of Materials Research*, 8(2):297–306, 1993.

[67] H. Hertz. On the contact of rigid elastic solids. *Journal fur die Reine und Angewandte Mathematik*, 1882(92):156–171, 1882.

[68] I.N. Sneddon. The relation between load and penetration in the axisymmetric boussinesq problem for a punch of arbitrary profile. *International Journal of Engineering Science*, 3(1):47 – 57, 1965.

[69] A.J. Bushby and N.M. Jennett. Determining the area function of spherical indenters for nanoindentation. *MRS Proceedings*, 649:Q7.17, 2000.

[70] D.K. Patel and S.R. Kalidindi. Correlation of spherical nanoindentation stress-strain curves to simple compression stress-strain curves for elastic-plastic isotropic materials using finite element models. *Acta Materialia*, 112:295–302, 2016.

[71] J.E. Campbell, R.P. Thompson, J. Dean, and T.W. Clyne. Acta Materialia Comparison between stress-strain plots obtained from indentation plastometry , based on residual indent pro fi les , and from uniaxial testing. *Acta Mater.*, 168:87–99, 2019.

[72] S. Pathak, S.R. Kalidindi, J.S. Weaver, Y. Wang, R.P. Doerner, and N.A Mara. Probing nanoscale damage gradients in ion-irradiated metals using spherical nanoindentation. *Scientific reports*, 7(1):11918, 2017.

[73] J.S. Weaver, S. Pathak, A. Reichardt, H.T. Vo, S.A. Maloy, P. Hosemann, and N.A. Mara. Spherical nanoindentation of proton irradiated 304 stainless steel: A comparison of small scale mechanical test techniques for measuring irradiation hardening. *Journal of Nuclear Materials*, 493:368–379, 2017.

[74] S. Pathak and S.R. Kalidindi. Spherical nanoindentation stress-strain curves. *Materials Science and Engineering R: Reports*, 91:1–36, 2015.

[75] B.R. Donohue, A. Ambrus, and S.R. Kalidindi. Critical evaluation of the indentation data analyses methods for the extraction of isotropic uniaxial mechanical properties using finite element models. *Acta Materialia*, 60(9):3943–3952, 2012.

[76] A. Clausner and F. Richter. Determination of yield stress from nano-indentation experiments. *European Journal of Mechanics - A/Solids*, 51:11 – 20, 2015.

[77] X. Xiao and L. Yu. Nano-indentation of ion-irradiated nuclear structural materials: A review. *Nuclear Materials and Energy*, 22:100721, 2020.

[78] A. Leitner, V. Maier-Kiener, and D. Kiener. Essential refinements of spherical nanoindentation protocols for the reliable determination of mechanical flow curves. *Materials and Design*, 146:69–80, 2018.

[79] N.I. Tymiak, D.E. Kramer, D.F. Bahr, T.J. Wyrobek, and W.W. Gerberich. Plastic strain and strain gradients at very small indentation depths. *Acta Materialia*, 49(6):1021–1034, 2001.

[80] J. Swadener. The correlation of the indentation size effect measured with indenters of various shapes. *Journal of the Mechanics and Physics of Solids*, 50(2002):681–694, 2002.

[81] G.M. Pharr, E.G. Herbert, and Y. Gao. The Indentation Size Effect: A Critical Examination of Experimental Observations and Mechanistic Interpretations. *Annual Review of Materials Research*, 40:271–292, 2010.

[82] A.J. Bushby and D.J. Dunstan. Plasticity size effects in nanoindentation. *Journal of Materials Research*, 19:137–142, 2004.

[83] I.J. Spary, A.J. Bushby, and N.M. Jennett. On the indentation size effect in spherical indentation. *Philosophical Magazine*, 86(33-35 SPEC. ISSUE):5581–5593, 2006.

[84] T.T. Zhu, X.D. Hou, A.J. Bushby, and D.J. Dunstan. Size effect at the initiation of plasticity for ceramics and metals. *Journal of Applied Physics D: Applied Physics*, 41(7), 2008.

[85] M.D. Uchic, D.M. Dimiduk, J.N. Florando, and W.D. Nix. Exploring specimen size effects in plastic deformation of ni_3(al, ta). *MRS Proceedings*, 753:BB1.4, 2002.

[86] M.D. Uchic and D.M. Dimiduk. A methodology to investigate size scale effects in crystalline plasticity using uniaxial compression testing. *Materials Science and Engineering A*, 400-401:268–278, 2005.

[87] J.R. Greer, W.C. Oliver, and W.D. Nix. Size dependence of mechanical properties of gold at the micron scale in the absence of strain gradients. *Acta Materialia*, 53:1821–1830, 2005.

[88] J.R. Greer and W.D. Nix. Nanoscale gold pillars strengthened through dislocation starvation. *Phys. Rev. B*, 73:245410, Jun 2006.

[89] W.D. Nix, J.R. Greer, G. Feng, and E.T. Lilleodden. Deformation at the nanometer and micrometer length scales: Effects of strain gradients and dislocation starvation. *Thin Solid Films*, 515(6):3152–3157, 2007.

[90] O. Kraft, P.A. Gruber, R. Mönig, and D. Weygand. Plasticity in Confined Dimensions. *Annual Review of Materials Research*, 40:293–317, 2010.

[91] S. Korte and W.J. Clegg. Discussion of the dependence of the effect of size on the yield stress in hard materials studied by microcompression of mgo. *Philosophical Magazine*, 91(7-9):1150–1162, 2011.

[92] P.S. Phani, K.E. Johanns, E.P. George, and G.M. Pharr. A simple stochastic model for yielding in specimens with limited number of dislocations. *Acta materialia*, 61(7):2489–2499, 2013.

[93] T.A. Parthasarathy, S.I. Rao, D.M. Dimiduk, M.D. Uchic, and D.R. Trinkle. Contribution to size effect of yield strength from the stochastics of dislocation source lengths in finite samples. *Scripta Materialia*, 56(4):313–316, 2007.

[94] D. J. Dunstan and A. J. Bushby. The scaling exponent in the size effect of small scale plastic deformation. *International Journal of Plasticity*, 40:152–162, 2013.

[95] DJ Dunstan, B Ehrler, R Bossis, S Joly, KMY P'ng, and AJ Bushby. Elastic limit and strain hardening of thin wires in torsion. *Physical review letters*, 103(15):155501, 2009.

[96] A.J. Bushby and D.J. Dunstan. Size effects in yield and plasticity under uniaxial and non-uniform loading: experiment and theory. *Philosophical Magazine*, 91(923714307):1–13, 2010.

[97] J.A. El-Awady. Unravelling the physics of size-dependent dislocation-mediated plasticity. *Nature Communications*, 6(May 2014):5926, 2015.

[98] X.D. Hou, A.J. Bushby, and N.M. Jennett. Study of the interaction between the indentation size effect and hall–petch effect with spherical indenters on annealed polycrystalline copper. *Journal of Physics D: Applied Physics*, 41(7):074006, mar 2008.

[99] X. Hou and N.M. Jennett. Application of a modified slip-distance theory to the indentation of single-crystal and polycrystalline copper to model the interactions between indentation size and structure size effects. *Acta Materialia*, 60(10):4128–4135, 2012.

[100] D.J. Dunstan. The size effect in the mechanical strength of semiconductors and metals: Strain relaxation by dislocation-mediated plastic deformation. *Journal of Materials Research*, 32(21):4041–4053, 2017.

[101] K. Fujii and K. Fukuya. Characterization of defect clusters in ion-irradiated a533b steel. *Journal of Nuclear Materials*, 336(2):323 – 330, 2005.

[102] D. Zhao, S. Li, X. Wang, Y. Wang, F. Liu, and X. Cao. Proton irradiation induced defects in t92 steels: An investigation by tem and positron annihilation spectroscopy. *Nuclear Instruments and Methods in Physics Research Section B: Beam Interactions with Materials and Atoms*, 442:59 – 66, 2019.

[103] M. Kiritani. Observation and analysis of defect structure evolution from radiation damage by d-t fusion neutrons. *Journal of Nuclear Materials*, 137(3):261 – 278, 1986.

[104] L.K. Mansur. Effects of point defect trapping and solute segregation on irradiation-induced swelling and creep. *Journal of Nuclear Materials*, 83(1):109 – 127, 1979.

[105] D. J. Mazey. Fundamental aspects of high-energy ion-beam simulation techniques and their relevance to fusion materials studies. *Journal of Nuclear Materials*, 174(2-3):196–209, 1990.

[106] G.S. Was. *Fundamentals of radiation materials science: metals and alloys*. Springer, 2016.

[107] C.D. Hardie and S.G. Roberts. Nanoindentation of model Fe-Cr alloys with self-ion irradiation. *Journal of Nuclear Materials*, 433(1-3):174–179, 2013.

[108] C. D. Hardie, G. R. Odette, Y. Wu, S. Akhmadaliev, and S. G. Roberts. Mechanical properties and plasticity size effect of Fe-6%Cr irradiated by Fe ions and by neutrons. *Journal of Nuclear Materials*, 482:236–247, 2016.

[109] E. M. Grieveson, D. E J Armstrong, S. Xu, and S. G. Roberts. Compression of self-ion implanted iron micropillars. *Journal of Nuclear Materials*, 2012.

[110] D. Kiener, P. Hosemann, S. A. Maloy, and A. M. Minor. In situ nanocompression testing of irradiated copper. *Nature Materials*, 10(8):608–613, 2011.

[111] D. L. Krumwiede, T. Yamamoto, T. A. Saleh, S. A. Maloy, G. R. Odette, and P. Hosemann. Direct comparison of nanoindentation and tensile test results on reactor-irradiated materials. *Journal of Nuclear Materials*, 504:135–143, 2018.

[112] A. Chbihi, X. Sauvage, and D. Blavette. Atomic scale investigation of Cr precipitation in copper. *Acta Materialia*, 60(11):4575–4585, 2012.

[113] D. J. Edwards, B. N. Singh, and S. Tähtinen. Effect of heat treatments on precipitate microstructure and mechanical properties of a CuCrZr alloy. *Journal of Nuclear Materials*, 367-370 B:904–909, 2007.

[114] J. Schindelin, I. Arganda-Carreras, E. Frise, V. Kaynig, M. Longair, T. Pietzsch, S. Preibisch, C. Rueden, S. Saalfeld, B. Schmid, J-Y Tinevez, D.J. White, V. Hartenstein, K. Eliceiri, P. Tomancak, and A. Cardona. Fiji: an open-source platform for biological-image analysis. *Nat Meth*, 9(7):676–682, jul 2012.

[115] P.T. Wady, A. Draude, S.M. Shubeita, A. Smith, N. Mason, S. . Pimblott, and E. Jimenez-Melero. Accelerated radiation damage test facility using a 5 MV tandem ion accelerator. *Nuclear Instruments and Methods in Physics Research, Section A: Accelerators, Spectrometers, Detectors and Associated Equipment*, 806:109–116, 2015.

[116] J.F. Ziegler, M.D. Ziegler, and J.P. Biersack. SRIM – The stopping and range of ions in matter (2010). *Nucl. Inst. Methods Phys. Res. B*, 268(11-12):1818–1823, 2010.

[117] A.P. Zhilyaev and T.G. Langdon. Progress in Materials Science Using high-pressure torsion for metal processing : Fundamentals and applications. *Progress in Materials Science*, 53(March):893–979, 2008.

[118] D.V. Shangina, N.R. Bochvar, A.I. Morozova, A.N. Belyakov, R.O. Kaibyshev, and S.V. Dobatkin. Effect of chromium and zirconium content on structure , strength and electrical conductivity of Cu-Cr-Zr alloys after high pressure torsion. *Materials Letters*, 199:46–49, 2017.

[119] N.V. Malyar, J.-S. Micha, G. Dehm, and C. Kirchlechner. Dislocation-twin boundary interaction in small scale cu bi-crystals loaded in different crystallographic directions. *Acta Materialia*, 129:91 – 97, 2017.

[120] R. van Bremen, D.R. Gomes, L.T.H. de Jeer, V. Ocelík, and J.Th.M. De Hosson. On the optimum resolution of transmission-electron backscattered diffraction (t-ebsd). *Ultramicroscopy*, 160:256–264, 2016.

[121] A. J. Wilkinson, T. B. Britton, J. Jiang, and P. S. Karamched. A review of advances and challenges in EBSD strain mapping. *IOP Conference Series: Materials Science and Engineering*, 55:012020, 2014.

[122] Gatan Corporation. EELS.info, n.d.

[123] F. de la Peña, M. Berger, J. Hochepied, F. Dynys, O. Stephan, and M. Walls. Mapping titanium and tin oxide phases using EELS : An application of independent component analysis. *Ultramicroscopy*, 111:169–176, 2011.

[124] Z. Shen, D. Tweddle, M. Thomas, B. Jenkins, D. Du, L. Zhang, M.P. Moody, and S. Lozano-perez. Scripta Materialia Observation of internal oxidation in a 20 % cold-worked Fe-17Cr-12Ni stainless steel through high-resolution characterization. *Scr. Mater.*, 173:8–12, 2019.

[125] G. Binnig, Ch. Gerber, E. Stoll, T.R. Albrecht, and C.F. Quate. Atomic resolution with atomic force microscope. *Surface Science*, 189-190:1 – 6, 1987.

[126] V.A. Bykov, Yu.A. Novikov, A.V. Rakov, and S.M. Shikin. Defining the parameters of a cantilever tip afm by reference structure. *Ultramicroscopy*, 96(2):175 – 180, 2003.

[127] D. Nečas and P. Klapetek. Gwyddion: an open-source software for SPM data analysis. *Central European Journal of Physics*, 10:181–188, 2012.

[128] M.R. VanLandingham, T.F. Juliano, and M.J. Hagon. Measuring tip shape for instrumented indentation using atomic force microscopy. *Measurement Science and Technology*, 16(11):2173–2185, sep 2005.

[129] T.T. Zhu, A.J. Bushby, and D.J. Dunstan. Size effect in the initiation of plasticity for ceramics in nanoindentation. *Journal of the Mechanics and Physics of Solids*, 56:1170–1185, 2008.

[130] J.S. Field and M.V. Swain. Determining the mechanical properties of small volumes of material from submicrometer spherical indentations. *Journal of Materials Research*, 10:101–112, 1995.

[131] K.L. Johnson. *Contact Mechanics*. Cambridge University Press, 1985.

[132] A.J. Bushby. Nano-Indentation Using Spherical Indenters. *Nondestructive Testing and Evaluation*, 17:213–234, 2001.

[133] A.H.W. Ngan and B. Tang. Viscoelastic effects during unloading in depth-sensing indentation. *Journal of Materials Research*, 17(10):2604–2610, 2002.

[134] C.D. Hardie. *Micro-mechanics of irradiated Fe-Cr alloys for fusion reactors*. PhD thesis, Oxford University, UK, 2013.

[135] J.W. Hutchinson. Plasticity at the micron scale. *International Journal of Solids and Structures*, 37:225–238, 2000.

[136] J. Bauer, C. Crook, A.G. Izard, Z.C. Eckel, N. Ruvalcaba, T.A. Schaedler, and L. Valdevit. Additive manufacturing of ductile, ultrastrong polymer-derived nanoceramics. *Matter*, 1(6):1547 – 1556, 2019.

[137] A.T. Jennings, M.J. Burek, and J.R. Greer. Microstructure versus size: mechanical properties of electroplated single crystalline cu nanopillars. *Physical review letters*, 104(13):135503, 2010.

[138] Y. Liu, S. Varghese, J. Ma, M. Yoshino, H. Lu, and R. Komanduri. Orientation effects in nanoindentation of single crystal copper. *International Journal of Plasticity*, 24(11):1990 – 2015, 2008.

[139] Y. Liu and A.H.W. Ngan. Depth dependence of hardness in copper single crystals measured by nanoindentation. *Scripta Materialia*, 44(2):237–241, 2001.

[140] S. Das, F. Hofmann, and E. Tarleton. Consistent determination of geometrically necessary dislocation density from simulations and experiments. *Int. J. Plast.*, 2018.

[141] E. Demir, D. Raabe, N. Zaafarani, and S. Zaefferer. Investigation of the indentation size effect through the measurement of the geometrically necessary dislocations beneath small indents of different depths using EBSD tomography. *Acta Mater.*, 57(2):559–569, 2009.

[142] S. Qu, Y. Huang, G.M. Pharr, and K.C. Hwang. The indentation size effect in the spherical indentation of iridium: A study via the conventional theory of mechanism-based strain gradient plasticity. *Int. J. Plast.*, 2006.

[143] T. Hirai, V. Barabash, F. Escourbiac, A. Fedosov, L. Ferrand, S. Gicquel, T. Jokinen, V. Komarov, A. Martin, and M. Merola. Design and integration of iter divertor components. In *Advances in Science and Technology*, volume 73, pages 1–10. Trans Tech Publ, 2010.

[144] M. Li and S.J. Zinkle. 4.20 - physical and mechanical properties of copper and copper alloys. In Rudy J.M. Konings, editor, *Comprehensive Nuclear Materials*, pages 667 – 690. Elsevier, Oxford, 2012.

[145] T. Hirai, V. Barabash, F. Escourbiac, A. Durocher, L. Ferrand, V. Komarov, and M. Merola. ITER divertor materials and manufacturing challenges. *Fusion Engineering and Design*, 125:250–255, 2017.

[146] A.J. Cackett, J.J.H. Lim, P. Klupś, A.J. Bushby, and C.D. Hardie. Using spherical indentation to measure the strength of copper-chromium-zirconium. *Journal of Nuclear Materials*, pages 5–11, 2018.

[147] Standard Practice for Determining Average Grain Size Using Electron Backscatter Diffraction (EBSD) in Fully Recrystallized Polycrystalline Materials, 2013.

[148] P.J. Imrich, C. Kirchlechner, C. Motz, and G. Dehm. Differences in deformation behavior of bicrystalline cu micropillars containing a twin boundary or a large-angle grain boundary. *Acta Materialia*, 73:240 – 250, 2014.

[149] I. S. Batra, G. K. Dey, U. D. Kulkarni, and S. Banerjee. Microstructure and properties of a Cu-Cr-Zr alloy. *Journal of Nuclear Materials*, 299:91–100, 2001.

[150] J. B. Correia, H. A. Davies, and C. M. Sellars. Strengthening in rapidly solidified age hardened Cu-Cr and Cu-Cr-Zr alloys. *Acta Materialia*, 45(1):177–190, 1997.

[151] E. Orowan. Symposium on internal stresses in metals and alloys. *Institute of Metals, London*, 451, 1948.

[152] ASTM E 1876:09. Standard Test Method for Dynamic Young's Modulus, Shear Modulus, and Poisson's Ratio by Impulse Excitation of Vibration, 2009.

[153] S.D. Preston, I. Bretherton, and C.B.A. Forty. The thermophysical and mechanical properties of the copper heat sink material intended for use in ITER. *Fusion Eng. Des.*, 68:441–446, 2003.

[154] S. Ranganathan, R. Divakar, and V.S Raghunathan. Interface structures in nanocrystalline materials. *Scripta Materialia*, 44(8):1169 – 1174, 2001.

[155] I. Matsui, T. Yamamoto, N. Omura, and Y. Takigawa. Effect of low-temperature annealing on tensile behavior of electrodeposited bulk nanocrystalline ni–w alloys. *Materials Science and Engineering: A*, 709:241 – 246, 2018.

[156] M. Das, G. Das, M. Ghosh, M. Wegner, V. Rajnikant, S. GhoshChowdhury, and T.K. Pal. Microstructures and mechanical properties of HPT processed 6063 Al alloy. *Mater. Sci. Eng. A*, 558:525–532, 2012.

[157] P. Král, J. Staněk, L. Kunčická, F. Seitl, L. Petrich, V. Schmidt, V. Beneš, and V. Sklenička. Microstructure changes in HPT-processed copper occurring at room temperature. *Mater. Charact.*, 151(February):602–611, 2019.

[158] C.C Koch. Optimization of strength and ductility in nanocrystalline and ultrafine grained metals. *Scripta Materialia*, 49(7):657 – 662, 2003. Viewpoint Set No. 31. Mechanical Properties of Fully Dense Nanocrystalline Metals.

[159] Standard Practice for Investigating the Effects of Neutron Radiation Damage Using Charged-Particle Irradiation, 2016.

[160] C. Heintze, F. Bergner, S. Akhmadaliev, and E. Altstadt. Ion irradiation combined with nanoindentation as a screening test procedure for irradiation hardening. *Journal of Nuclear Materials*, 472:196 – 205, 2016.

[161] N. Galy, N. Toulhoat, N. Moncoffre, Y. Pipon, N. Bérerd, M.R. Ammar, P. Simon, D. Deldicque, and P. Sainsot. Ion irradiation used as surrogate of neutron irradiation in graphite: Consequences on 14c and 36cl behavior and structural evolution. *Journal of Nuclear Materials*, 502:20 – 29, 2018.

[162] C.D. Hardie, A.J. London, J.J.H. Lim, R. Bamber, T. Tadić, M. Vukšić, and S. Fazinić. Exploitation of thermal gradients for investigation of irradiation temperature effects with charged particles. *Sci. Rep.*, 9(1):13541, dec 2019.

[163] J. Hütsch and E.T. Lilleodden. The influence of focused-ion beam preparation technique on microcompression investigations: Lathe vs. annular milling. *Scripta Materialia*, 77:49 – 51, 2014.

[164] P. Hosemann, C. Shin, and D. Kiener. Small scale mechanical testing of irradiated materials. *Journal of Materials Research*, 30(9):1231–1245, 2015.

[165] B. Ehrler, X.D. Hou, T.T. Zhu, K.M.Y. P'ng, C.J. Walker, A.J. Bushby, and D.J. Dunstan. Grain size and sample size interact to determine strength in a soft metal. *Philosophical Magazine*, 88(25):3043–3050, 2008.

Appendix A

CuCrZr grain size measurement

In order to measure the average grain size of the as-received and heat-treated CuCrZr samples, three EBSD maps were acquired in different areas over the surface of each sample. All maps covered a 1 x 1.5 mm area and with a step size (i.e. pixel size) of 4 μm. Figures A.1 - A.7 below are the inverse pole figure (IPF) maps for each of the samples, which are coloured relative to orientation in the surface normal direction. Note that the 500 μm scale provided applies to all maps in the set.

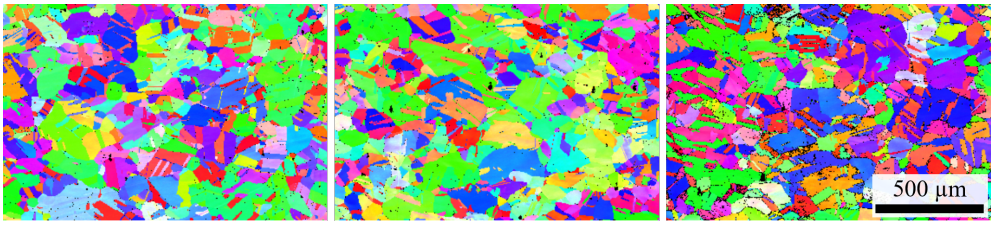

Fig. A.1 EBSD maps used for grain size analysis of CuCrZr-AR.

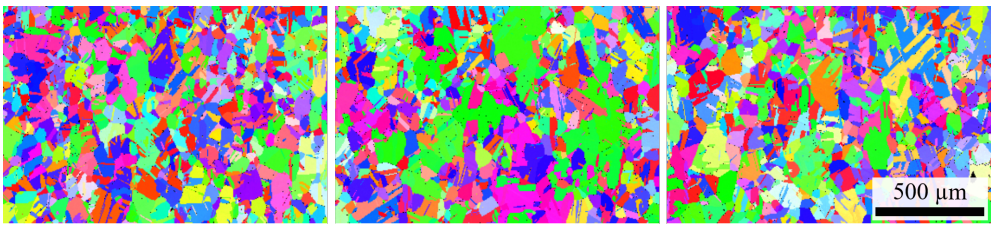

Fig. A.2 EBSD maps used for grain size analysis of CuCrZr-400.

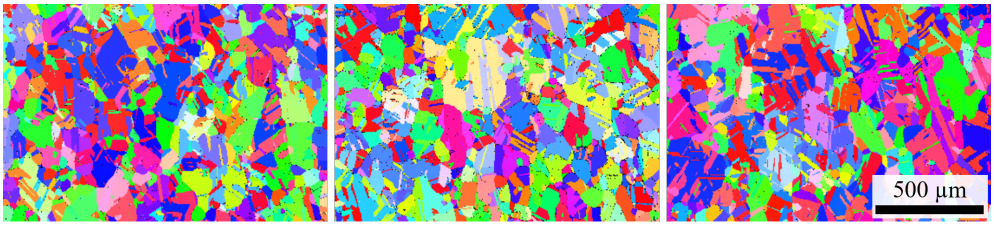

Fig. A.3 EBSD maps used for grain size analysis of CuCrZr-480.

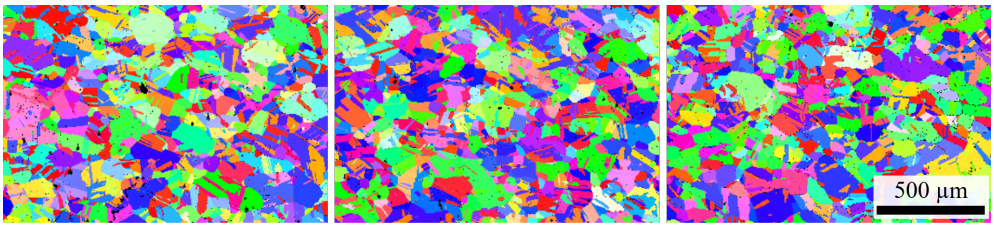

Fig. A.4 EBSD maps used for grain size analysis of CuCrZr-550.

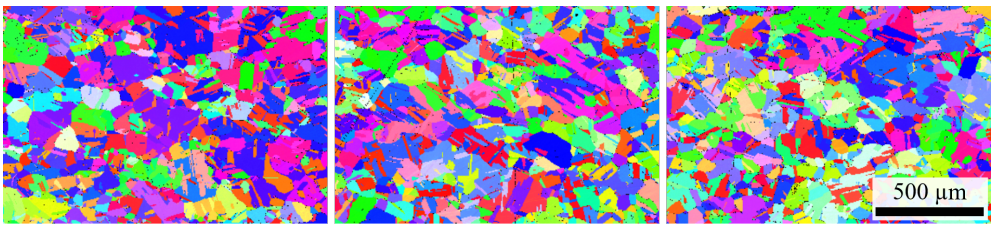

Fig. A.5 EBSD maps used for grain size analysis of CuCrZr-600.

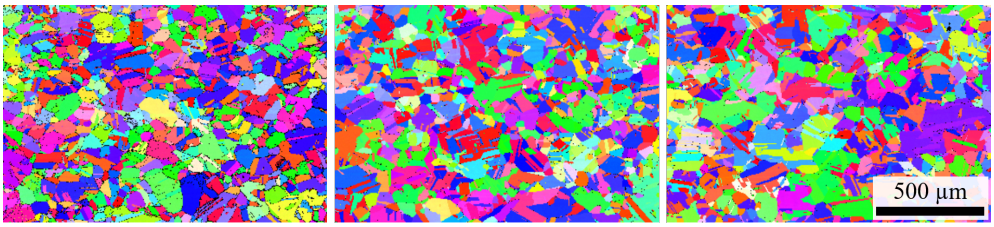

Fig. A.6 EBSD maps used for grain size analysis of CuCrZr-650.

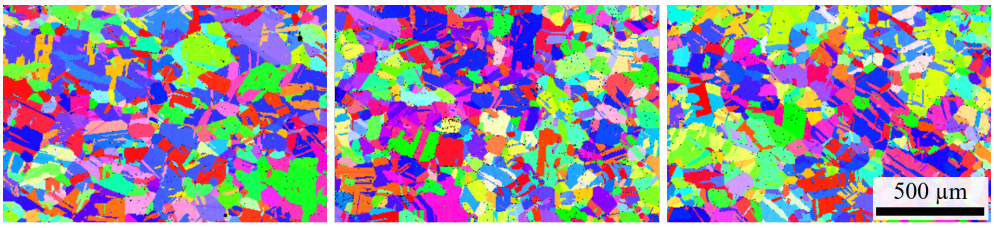

Fig. A.7 EBSD maps used for grain size analysis of CuCrZr-700.

The colours in these IPF maps are indicative of crystallographic orientation in the surface normal direction, the key for which can be seen in Figure A.8.

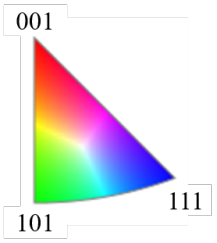

Fig. A.8 Orientation of EBSD maps with respect to the IPF colouring.

Appendix B

Spherical indentation data for CuCrZr

Spherical indentation data (indentation stress-strain curves and elastic modulus measurements) for all tip radii, grouped by material type.

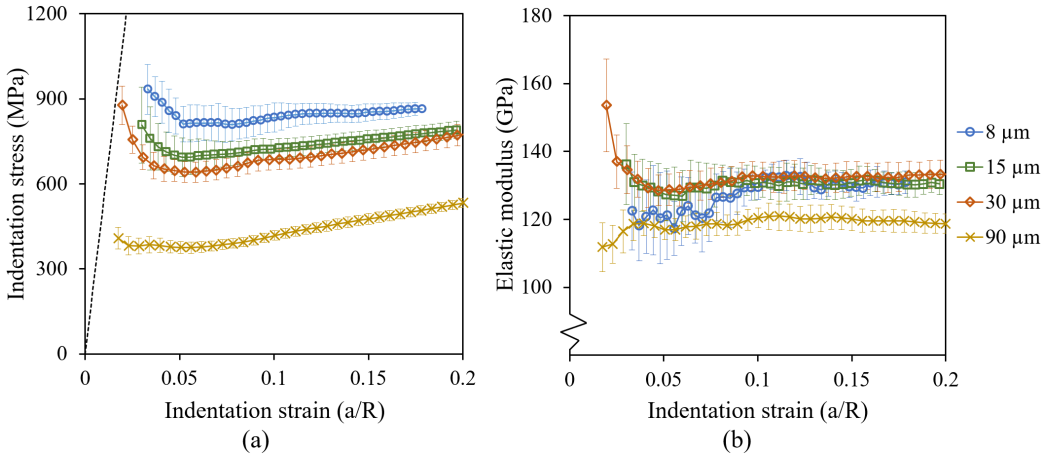

Fig. B.1 Spherical indentation (a) stress-strain and (b) elastic modulus data for CuCrZr-AR.

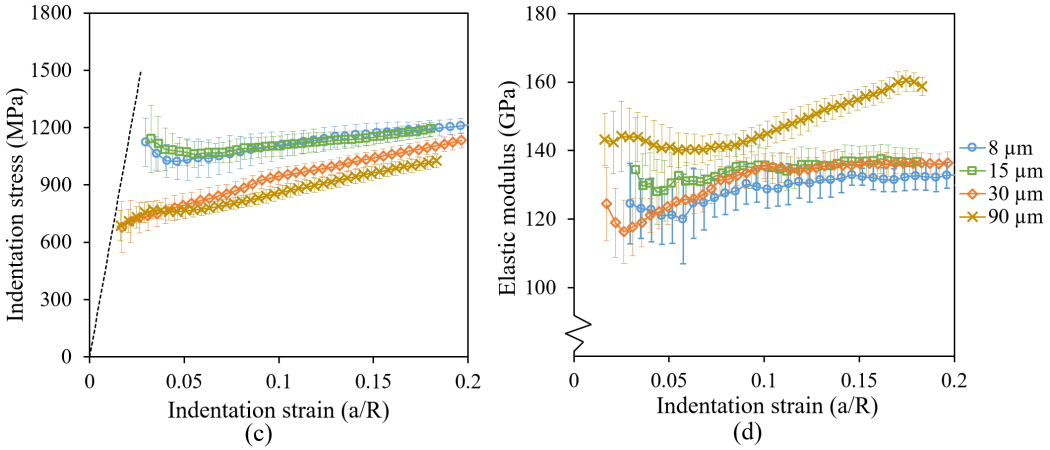

Fig. B.2 Spherical indentation (c) stress-strain and (d) elastic modulus data for CuCrZr-400.

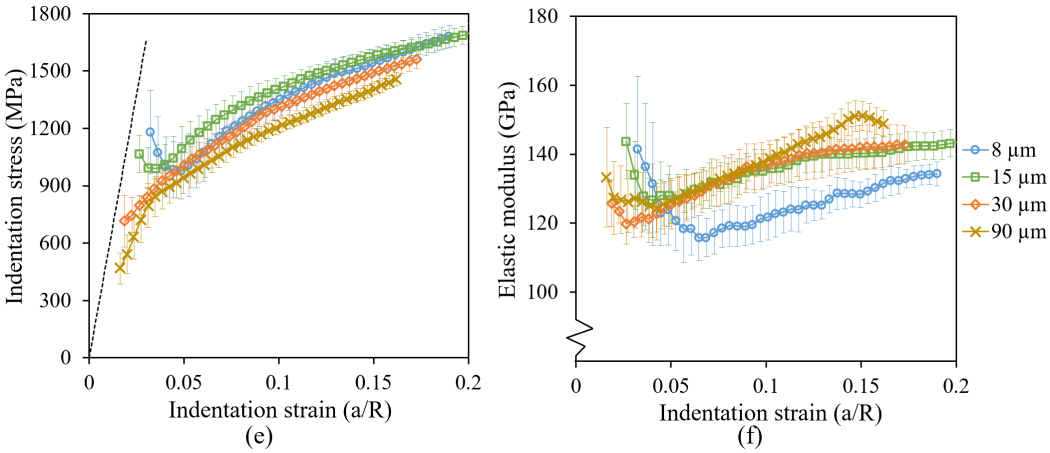

Fig. B.3 Spherical indentation (e) stress-strain and (f) elastic modulus data for CuCrZr-480.

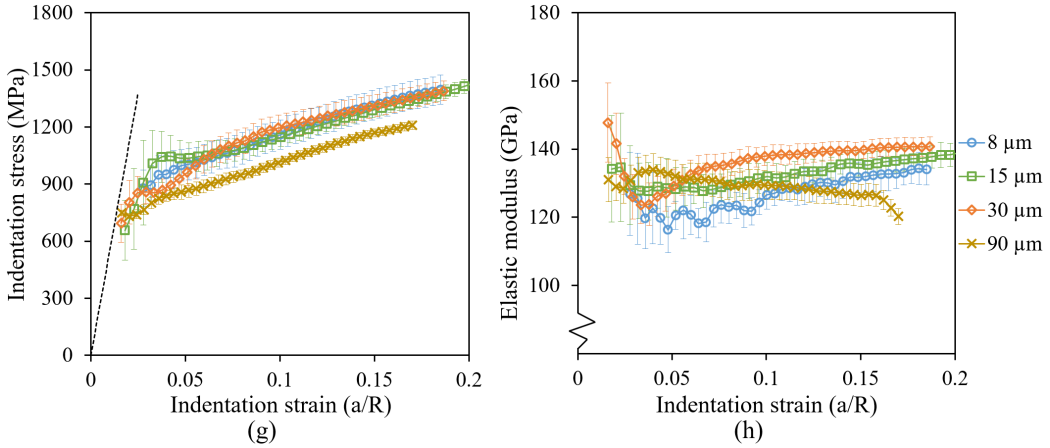

Fig. B.4 Spherical indentation (g) stress-strain and (h) elastic modulus data for CuCrZr-550.

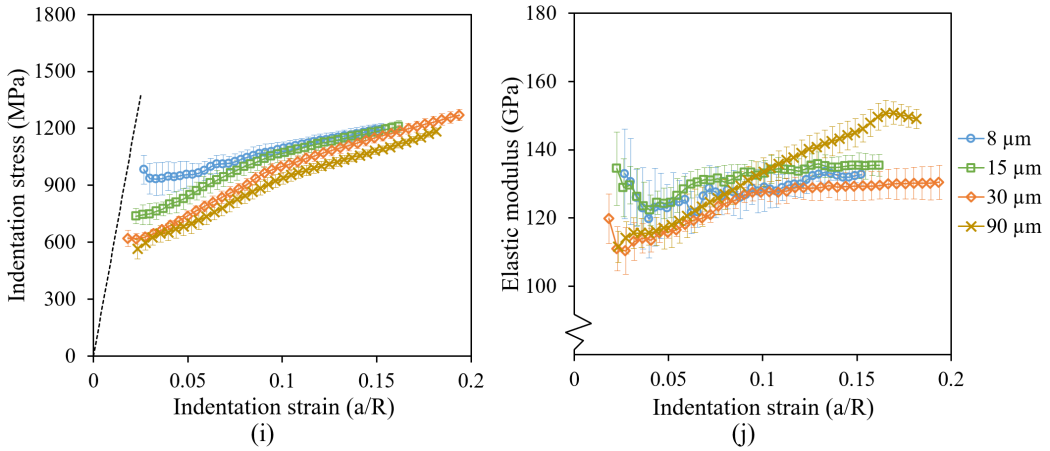

Fig. B.5 Spherical indentation (i) stress-strain and (j) elastic modulus data for CuCrZr-600.

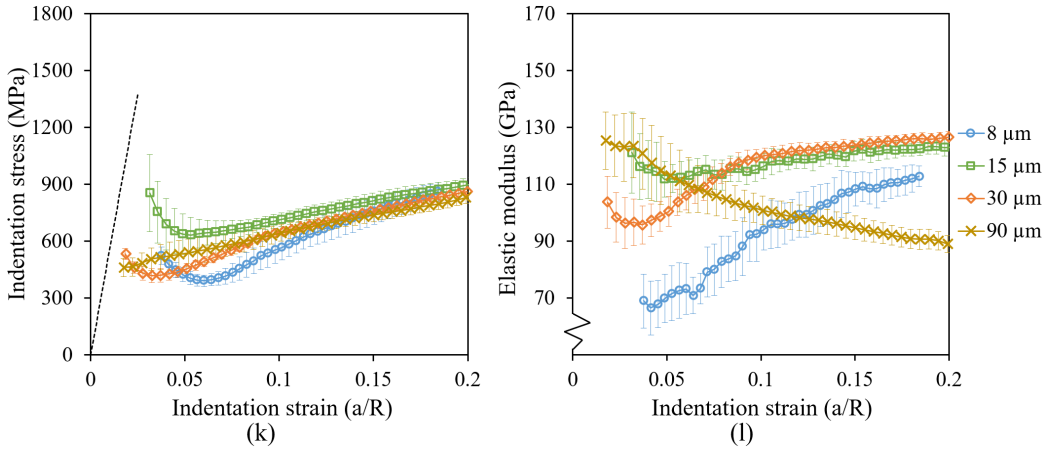

Fig. B.6 Spherical indentation (k) stress-strain and (l) elastic modulus data for CuCrZr-650.

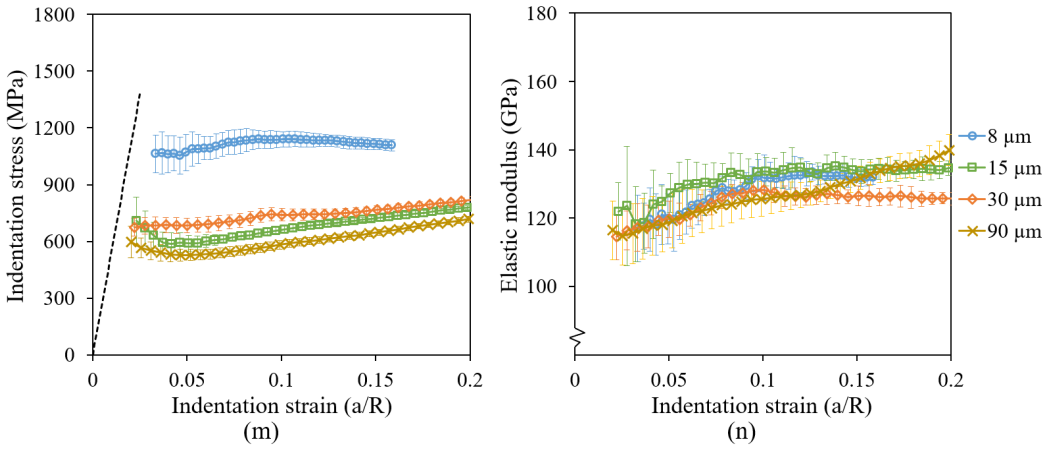

Fig. B.7 Spherical indentation (m) stress-strain and (n) elastic modulus data for CuCrZr-700.

Appendix C

Spherical indentation data for HPT CuCrZr

Spherical indentation data (indentation stress-strain curves and elastic modulus measurements) for all tip radii, grouped by material type.

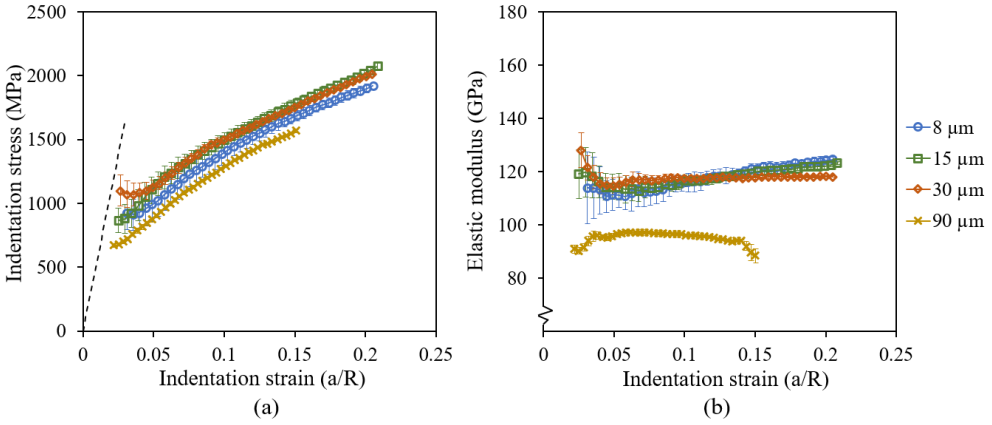

Fig. C.1 Spherical indentation (a) stress-strain and (b) elastic modulus data for HPT-AR CuCrZr.

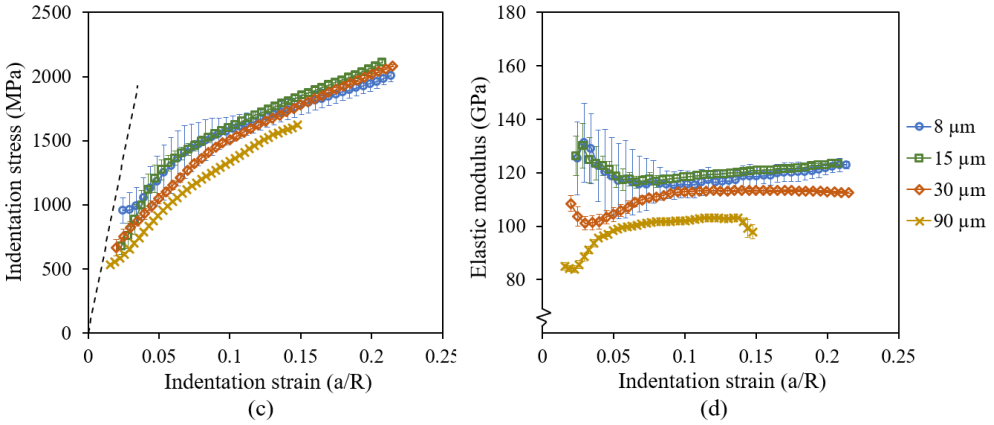

Fig. C.2 Spherical indentation (c) stress-strain and (d) elastic modulus data for HPT-AR-200 CuCrZr.

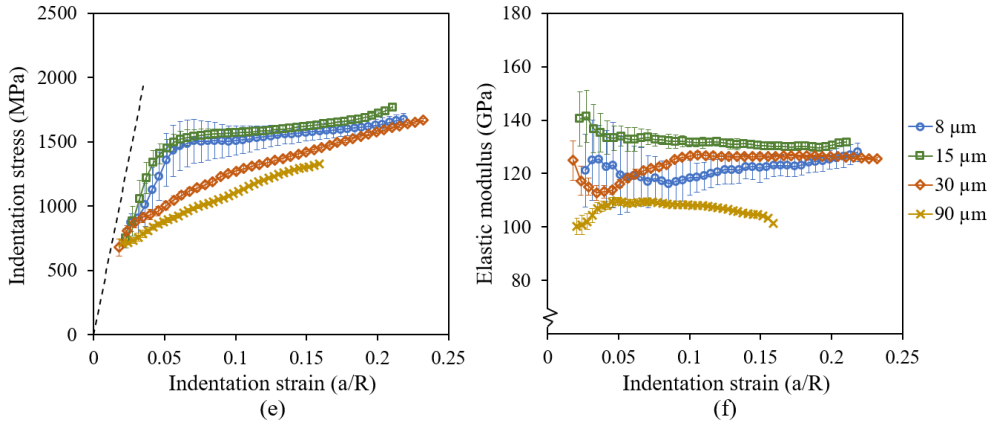

Fig. C.3 Spherical indentation (e) stress-strain and (f) elastic modulus data for HPT-AR-600 CuCrZr.

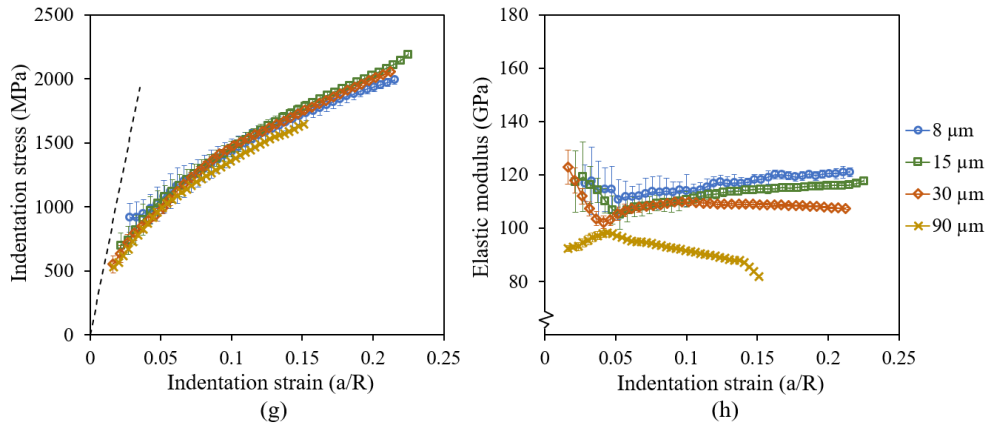

Fig. C.4 Spherical indentation (g) stress-strain and (h) elastic modulus data for HPT-550 CuCrZr.

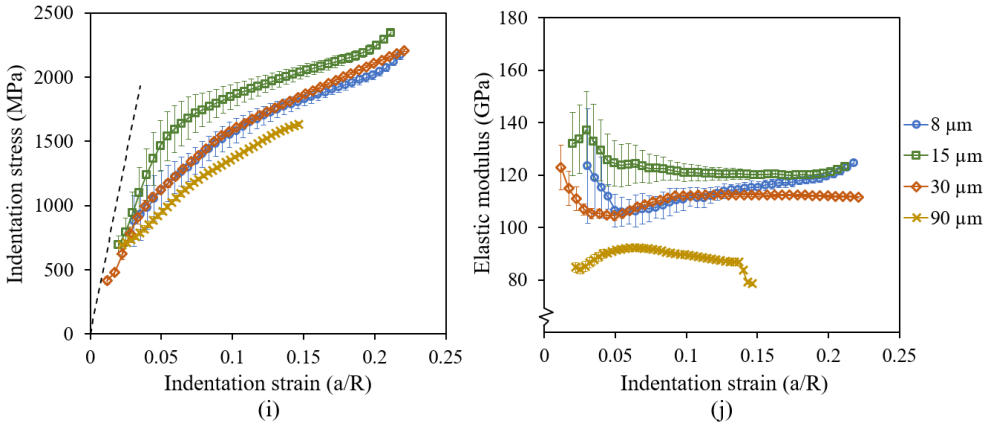

Fig. C.5 Spherical indentation (i) stress-strain and (j) elastic modulus data for HPT-550-200 CuCrZr.

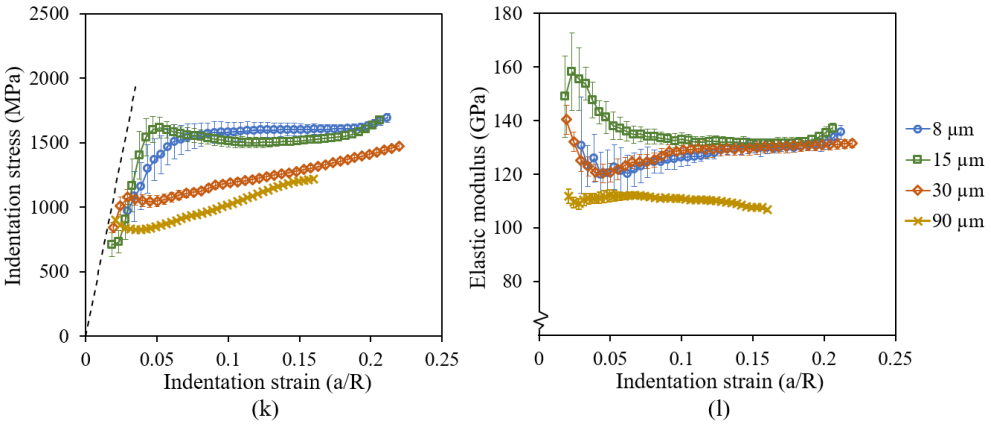

Fig. C.6 Spherical indentation (k) stress-strain and (l) elastic modulus data for HPT-550-600 CuCrZr.

Appendix D

Pillar compression experiments

Results for all micro-pillar compression experiments in as-received, peak-aged (480 °C) and over-aged (650 °C) CuCrZr as well as proton irradiated samples of each of these.

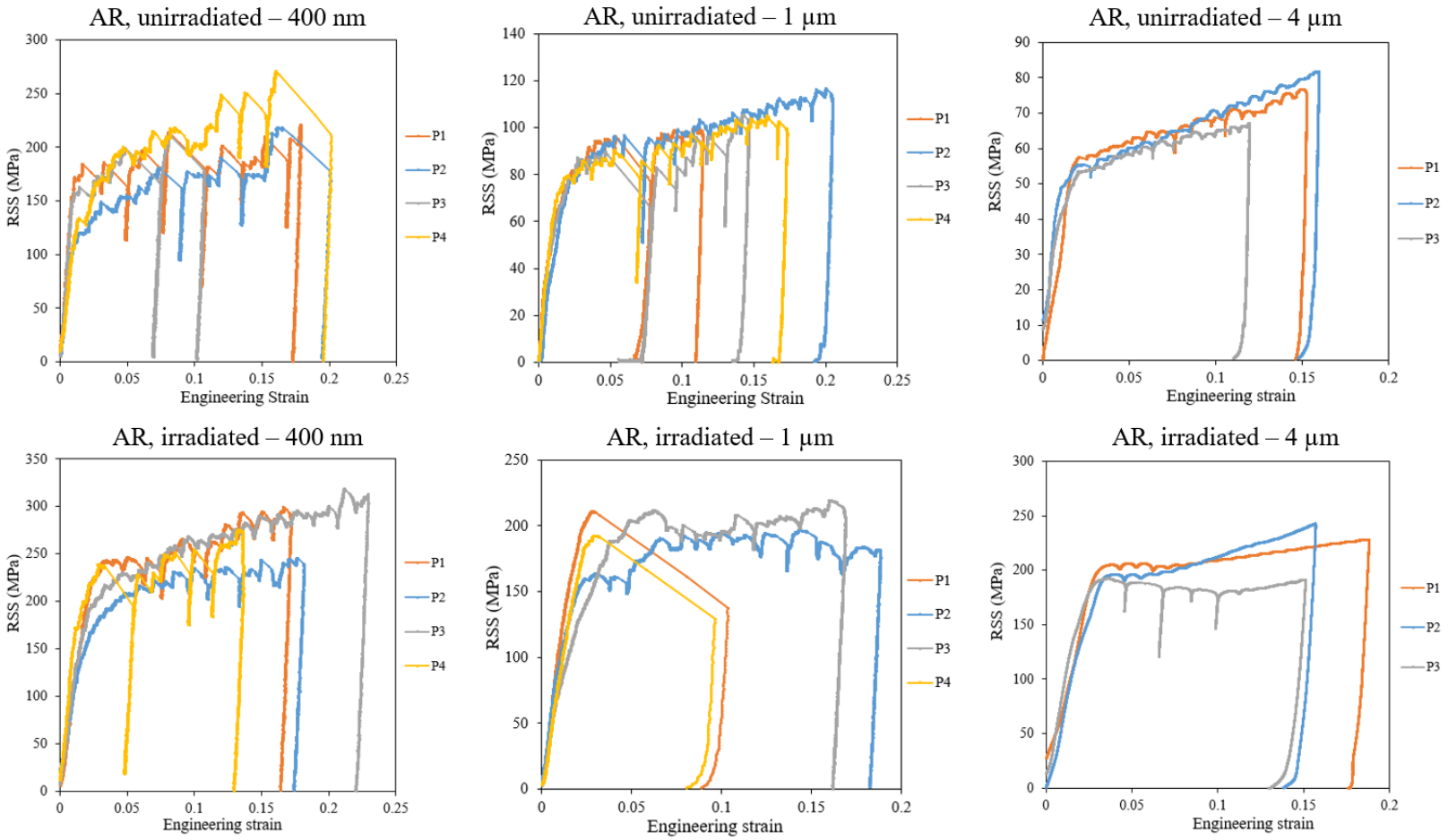

Fig. D.1 All results from pillar compression experiments in CuCrZr-AR.

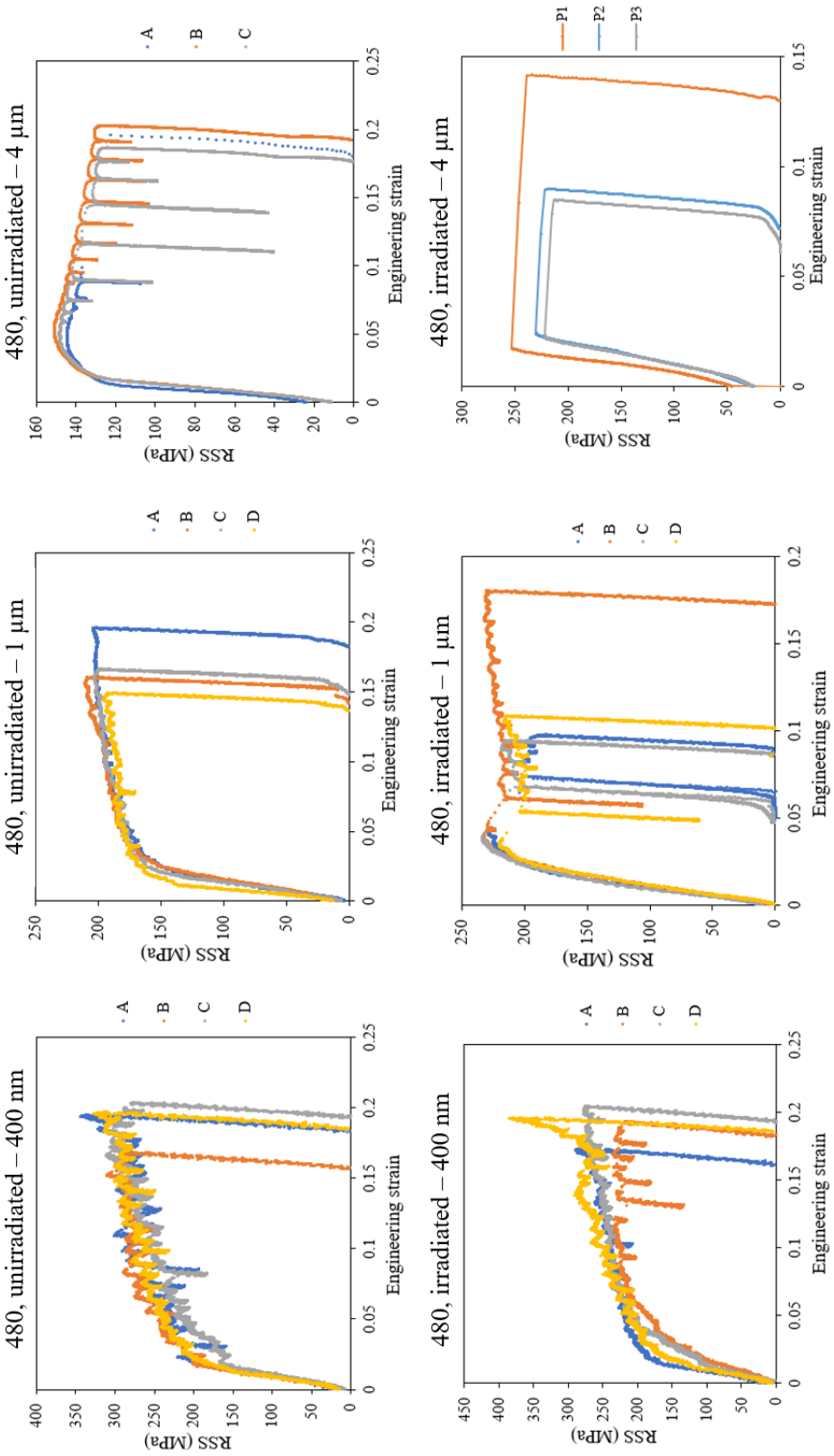

Fig. D.2 All results from pillar compression experiments in peak-aged CuCrZr-480.

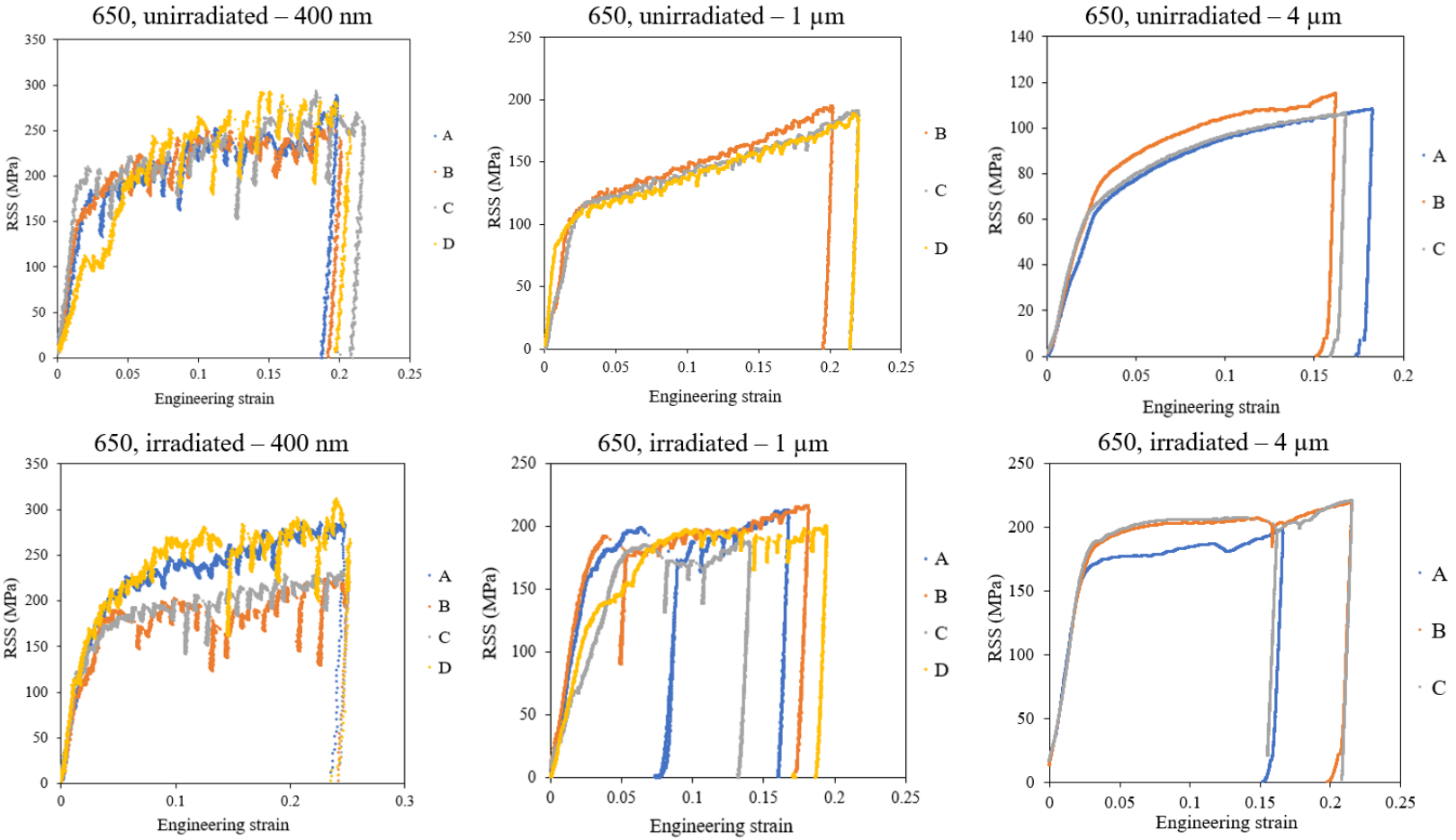

Fig. D.3 All results from pillar compression experiments in CuCrZr-650.